Extragalactic molecular clouds and chemistry of diffuse interstellar clouds

Yuri Beletsky

SIGILL. UNIVERSITAT. LUDOVIC. MAXIM.

München, 2009

Extragalactic molecular clouds and chemistry of diffuse interstellar clouds

Yuri Beletsky

Dissertation
an der Fakultät für Physik
der Ludwig–Maximilians–Universität
München

vorgelegt von
Yuri Beletsky
aus Minsk, Belarus

München, den 2009

Erstgutachter: Prof. Dr. Ralf Bender
Zweitgutachter: Prof. Dr. Andreas Burkert
Tag der mündlichen Prüfung: 2009

To my friends.

Abstract / Zusammenfassung

Since the discovery of a cold molecular component of the interstellar medium in the 1970s, it has been realized that most of the dark clouds are actually molecular clouds, consisting mainly of molecular hydrogen and some amount of dust and other molecules. Nowadays, molecular clouds are recognized as places of star-formation in the Milky Way and other galaxies. Therefore, studies of the structure, physical conditions, and chemical compositions of these objects are of paramount importance, since they allow us to understand the process of star formation.

This thesis presents the study of giant molecular clouds in the giant elliptical radio galaxy NGC5128 (Centaurus A) and an analysis of the chemical composition of diffuse interstellar clouds. Using dust as tracer of molecular hydrogen, and detecting the clouds by a multi-scale wavelet based method we derive basic parameters of the molecular clouds in NGC5128. We show that the slope of the mass spectrum of molecular clouds is significantly steeper than that of Galactic clouds.

Our near-infrared study of the nucleus region of the giant elliptical galaxy NGC1316 (Fornax A) reveals a ”peanut-shape” structure in the nucleus, which was hidden behind dense dust lanes. We estimate the sizes of the structure and, applying optical and near-infrared kinematical data, propose several possible explanations of the complex nuclear morphology. The chemical analysis of diffuse interstellar clouds leads us to a discovery of a new class of objects – Ca-Fe interstellar clouds. They turn out to be rare (just a few examples among ~ 300 lines of sight) objects with the Ca I 4227 Åas well as Fe I 3720 Åand 3860 Ålines stronger than those of K I (near 7699 Å) and Na I (near 3302 Å), occupying volumes different from the well-known interstellar H I clouds where the K I and ultraviolet Na I lines are dominant features. We establish that the CaFe clouds can be found only along sightlines toward hot, luminous (and thus distant) objects with high rates of mass loss.

We also suggest a new consistent system of the oscillator strength of several unsaturated methylidyne bands. Based on optical spectra of a sample of stars we estimate methylidyne column densities.

Finally, we study spatial correlations of some diffuse interstellar bands (DIB) and simple molecules. We find that radial velocities of CH, CH$^+$ features, and two narrow DIBs at 6196 and 4964 Åsuggest that the 6196 DIB carrier is spatially correlated with CH$^+$, while the 4964 DIB carrier prefers environments where the CH molecule is abundant. Using a statistically meaningful sample of reddened OB stars and analyzing correlations between CH and CH$^+$ column densities and DIB strengths we clearly confirm this suggestion.

Seit der Entdeckung einer kalten, molekularen Komponente im Interstellaren Medium in den 1970er Jahren kam man zu der Erkenntnis, dass die meisten interstellaren Dunkelwolken tatsächlich Molekülwolken sind, die zur Hauptsache aus molekularem Wasserstoff und einem gewissen Anteil anderer Moleküle sowie Staub bestehen. Heutzutage sind Molekülwolken allgemein anerkannt als Stätten der Sternentstehung in unserer Milchstraße und anderen Galaxien. Deshalb sind Studien ihrer Struktur, physikalischen Bedingungen und chemichen Zusammensetzung von herausragender Bedeutung, erlauben sie uns doch das Verständnis des Prozesses der Sternentstehung.

Die vorliegende Dissertation präsentiert eine Studie der Riesenmolekülwolken in der elliptischen Radiogalaxie NGC5128 (Centaurus A), sowie eine Analyse der chemischen Zusammensetzung von diffusen interstellaren Wolken. Unter der Verwendung von Staub als Indikator des molekularen Wasserstoffs und einer Detektionsmethode mithilfe einer zweidimensionalen Elementarwellenanalyse auf unterschiedlichen Größenskalen werden grundlegende Parameter der Riesenmolekülwolken in NGC5128 abgeleitet. Es läßt sich dadurch zeigen, dass die Steigung des Massenspektrums der Molekülwolken in NGC5128 deutlich größer ist als jene von galaktischen Wolken.

Die Untersuchung der Kernregion der elliptischen Riesengalaxie NGC1316 (Fornax A) im nahen Infrarot enthüllt eine erdnussförmige Struktur des Kerns, welche bislang hinter dichten Staubfilamenten verborgen war. Wir schätzen die Größe der Struktur ab und geben unter Einbezug von optischen und nah-infrarot Beobachtungsdaten der Kernkinematik mehrere Erklärungsmöglichkeiten der komplexen Kernmorphologie ab.

Die chemische Analyse diffuser interstellarer Wolken brachte die Entdeckung einer neuen Klasse von Objekten mit sich: interstellare Kalzium-Eisen (Ca-Fe) Wolken. Es stellt sich heraus, dass diese Klasse von Wolken sehr selten ist, mit nur ein paar wenigen Vertretern entlang von ca. 300 Sichtlinien. Im Falle einer Ca-Fe Wolke sind die interstellaren Absorptionslinien Ca I 4227 Åsowie Fe I 3720 Åund 3860 Åstärker als jene von K I (bei 7699 Å) und Na I (bei 3302 Å). Darüberhinaus nehmen sie einen anderen Raum als die bekannten interstellaren H I Wolken ein, in denen die K I und ultravioletten Na I Linien dominieren. Wir zeigen zudem, dass Ca-Fe Wolken nur entlang von Sichtlinien zu heißen, leuchtkräftigen (und daher weit entfernten) Sternen mit hohen Massenverlustraten zu finden sind.

Die Arbeit legt des Weiteren einen neuen, konsisenten Satz von Oszillatorstärken mehrerer nicht saturierter Banden des CH Moleküls vor. Basierend auf optischen Spektren einer Auswahl von Sternen schätzen wir CH Säulendichten ab.

Abschließend untersuchen wir die räumliche Korrelation zwischen einigen diffusen interstallaren Banden (DIB) und einfachen Molekülen. Dabei zeigt sich, dass die Radialgeschwindigkeit von CH und CH$^+$ Merkmalen einerseits und zweier DIBs bei 4964 und 6196 Åandererseits eine räumliche Korrelation zwischen CH$^+$ und dem 6196 ÅDIB nahelegen, wohingegen das 4964 ÅDIB Umgebungen mit hoher CH-Konzentration bevorzugt. Diese Hypothese wird von einer Untersuchung der Korrelation zwischen CH und CH$^+$ Säulendichten und DIB Stärken in einer statistisch aussagekräftigen Auswahl von geröteten Sternen des Spektraltyps O und B eindeutig unterstützt.

Contents

List of Figures

List of Tables

1

Introduction

Our understanding of how stars and planets form is still incomplete and remains one of the longest-standing problems in astronomy today. Being a part of the interstellar medium (ISM) in galaxies molecular clouds are the key components of star formation process. It is today well accepted that most if not all stars are born from the gravitational collapse of the densest regions of a molecular cloud.

On the other hand, study of the chemical composition of the interstellar medium is important and can provide unique opportunities to investigate fundamental processes in galaxies, from metal enrichment to star and planet formation, and assert on cosmological questions. Molecular clouds contain large number of molecules and stretch across a large range of densities, pressures, and temperatures. At the same time a fraction of those molecules can found here on Earth. Comparing molecular processes in molecular clouds with those on Earth can provide insights into how our planet's chemistry evolved given its unique environment.

Despite some progress in our understanding of the origin and evolution of molecular clouds there are still many question which remain open. Namely, how are molecular clouds formed? What physical properties of molecular gas explain the variety of star formation rates observed? What are the lifetimes of molecular clouds? What are the carriers of complex molecules which are found in diffuse interstellar clouds?

The remainder of this chapter presents introductory background material regarding molecular clouds and the chemistry of diffuse interstellar clouds (mostly focusing on enigmatic diffuse interstellar bands) and explains what are the goals and structure of this thesis.

1.1 Giant molecular clouds

Molecular clouds are cold (10-40K) and dense ($n(H_2) = 10^2 cm^{-3}$) regions of the interstellar medium containing $\sim 90\%$ of H_2, $\sim 10\%$ of He, and many other molecules. Dust particles, such of carbon or silicate material, comprise about 1 per cent of a clouds mass, and they are the cause of extinction within the cloud.

Masses of molecular clouds typically range from 100 to $10^6 M_\odot$, while the sizes are of few to hundreds parsec. Molecular clouds of masses $10^3 ... 10^6 M_\odot$ are self-gravitating and called giant molecular clouds (GMCs). Clouds which have lower masses do not seem to be self-gravitating and therefore external pressures of the ISM is required in order to maintain the equilibrium of this population (Heyer et al. 2001). The internal structure of molecular clouds is quite complex (see Figure 1.1) and consists of clumps and filaments of dense gas surrounded by interclump gas of much lower density (Williams et al. 1994). Individual clumps typically have supersonic internal motions reaching a velocity of several kilometers per second. The outflows produced by young stars during the first 10^5years of their existence may be a major source of these chaotic motions. It has been shown by numerous studies that there is a strong correlation between location of young stars and molecular clouds (see a review by Blitz & Williams 1999). Magnetic fields which thread molecular clouds play an important role in the longevity of turbulent motions and may support clouds against gravitational collapse.

Lifetime of molecular clouds are from 3 to 30 Myr, thus these objects seem to be transient entities. Given this fact, molecular clouds must be formed and destroyed constantly in the disks of most galaxies. While the clouds formation mechanism is not known yet, clouds are destroyed by the dissociating radiation coming from the young stars that form within them. There might be other ways of clouds destruction, like supernova shocks from the newly formed stars, protostellar winds, the ram pressure of turbulent flows, etc.

One of the most important questions to be addressed in molecular cloud research is the determination on how exactly clouds are produced by the interstellar medium? This is especially interesting for giant molecular clouds, which are believed to be the cradle of star formation in the Universe. The second obvious question is then how GMCs produce in turn stars, star clusters, and eventually planets.

GMC formation

It is commonly accepted that there are more than a single mechanism for cloud formation (Elmegreen 1993, and references therein). Earlier proposed models of collisional agglomeration of smaller cloudlets (Kwan 1979; Cowie 1980) do not reproduce the observational data (Blitz & Shu 1980). The model predict the time, required for building up a GMC, is about 100 Myr which is too long and makes difficult to support a GMC against collapse or avoid their disruption by SN explosions and the internal HII regions. Moreover Blitz & Williams (1999) emphasize that in order to allow the formation of GMCs via agglomeration there is simply not enough molecular material in the “chaff ”. As a result, since the clouds are not a collection of isolated entities

The "Black Cloud" B68
(VLT ANTU + FORS1)

ESO PR Photo 20a/99 (30 April 1999)

© European Southern Observatory

FIGURE 1.1: Molecular Cloud Barnard 68. Credit: Joao Alves

of gas, but a complex interconnected network, the whole hypothesis of the "cloudlets" might be inadequate (Scalo 1990).

Involving the idea of a turbulent ISM, clouds may form by the convergence of the turbulent flows at large scales. These might be as results produced by different kinds of instabilities, like Parker, thermal, gravitational, or magnetorational (Sellwood & Balbus 1999), the passage of spiral density waves, swept up shells from SN remnants or simply the general action of global turbulence, where no single apparent mechanism is invoked, but the result of streams at different velocities that collide (Elmegreen 1993; Blitz & Williams 1999). This latter type of mechanism involving coherent instabilities is favored both on theoretical and empirical grounds.

Being a long-range force, gravity is a natural candidate to drive dynamical instabilities and collect the ISM over a large spatial scale. It may act in two different ways – either locally changing the net force on gas by varying its buoyancy in the background vertical gravitational field of the galaxy (Parker instability), and/or changing the local gravitational field on the gas via the self-gravitation of positive density perturbations (Jeans instability). There are other important effects, which include:

- Turbulence, which produces large–amplitude perturbations in the gas properties at a range of scales
- Stellar spiral arms in galaxies, which induce large local variations in the background ISM velocity, density, and magnetic field
- Coriolis forces, which produce epicyclic motion
- Differential rotation in the galactic potential, which produces background shear
- Magnetic fields, which produce pressure and tension forces

After a cloud is formed, how long does it live? This is a fundamental question but the problem of reliable lifetimes estimates still remains. The estimates of the lifetime of a GMC vary from 10^6 to 10^8 years. Clouds with shorter lifetimes can barely be self-gravitating. However, there some theoretical studies suggesting that clouds do have short lifetimes and they are not self-gravitating (e.g. Elmegreen et al. 2000).

The lifetime of molecular clouds must be much larger than the dynamical time: $t_{dyn} \sim 2.5{M_5}^{1/4}$ using the mass-radius relationship, obtained by Solomon et al. (1987). M_5 is the mass of the cloud expressed in units of $10^5 M_{\odot}$. Based on dissipation the molecular material by photoionization Blitz & Shu (1980) calculated an upper limit on the lifetimes of molecular clouds of $\tau_{cloud} \lesssim 30$ Myr. CO observations of young cluster and molecular clouds in our Galaxy (Leisawitz et al., 1989) and in the Large Magellanic Cloud (Yamaguchi et al., 2001a) suggest the lower limit on cloud lifetimes as $\tau_{cloud} \sim$ 10 Myr. According to Williams & McKee (1997) molecular cloud lifetimes are most probably located within the range of $20 - 30$ Myr with some scaling due to the mass of the cloud. In fact this is longer than a dynamical time by the factor of 5 – 10. Based on the observational evidence, it seems that molecular clouds are self-gravitating objects.

The mass spectrum of giant molecular clouds

The mass distribution (or the mass spectrum) of molecular clouds is one of the basic characteristics of this population. Using various independent approaches, such as principal component analysis (Heyer & Schloerb 1997), delta variance techniques (Stutzki et al. 1998), spectral correlation functions (Rosolowsky et al. 1999), multi-fractal analysis (Chappell & Scalo 2001), etc., it has been shown that interstellar gas seems to be scale-free. However, applying intensity contouring drawing (Williams et al. 1994) or gaussian fit to absorption spectral lines (Spitzer & Jenkins 1975), the interstellar medium looks like a collection of discrete clouds. These two interpretations have led to different models for star formation and the origin of gas structure. Scale-free models typically involve turbulence and self-gravity (see Elmegreen 2002, and references therein). Therefore the mass spectrum of molecular clouds is the key contact point between those two views, providing the clouds can be isolated and well defined. Such the spectrum is also important for bound star clusters, which are better defined (Elmegreen et al. 2000), and for individual stars, whose masses are probably proportional to the primordial clump masses (Motte et al. 1998; Testi & Sargent 1998).

Another interesting application of the GMC mass function is its relation to the initial mass function (IMF) of stars. The latter one was determined by Salpeter (1955). With some rare exceptions, it's not possible to measure IMF directly in other galaxies. Since the evolution of disk masses depends on the shape of the IMF (at low mass end), it it becoming important to know how IMF is changing from galaxy to a galaxy. This will allows us to understand more about the galaxy evolution. One of possible approaches is to have a look at the GMCs – the "cradles" of star formation. If the clouds have similar properties within (and between) the galaxies, than it would mean that the stars, that are formed in those clouds might have similar properties and distributions.

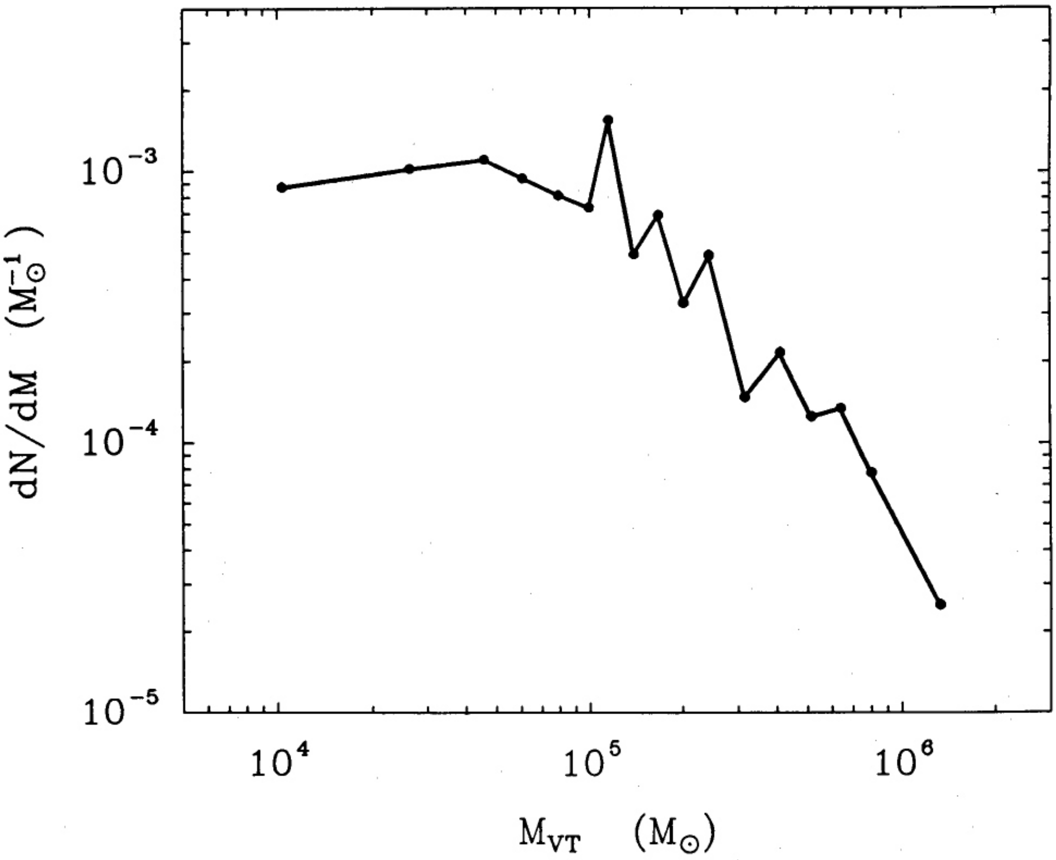

FIGURE 1.2: The molecular clouds mass spectrum dN/dM. A fit to the data above 7×10^4 $M_\odot$ gives $dN/dM \propto M^{-3/2}$ (Solomon et al. 1987).

Determination of the mass function of GMCs requires a large homogeneous and unbiased survey. Good angular resolution is essential in order to separate and resolve individual clouds. Unfortunately molecular hydrogen itself is hardly detectable due to following reasons – firstly, hydrogen is a homonuclear molecule which is lacking a permanent dipole moment and as a result its rotational transitions are very weak. Secondly, due to very low mass of the molecule its lowest energy rotational transitions located in mid-infrared wavelengths, which are not observable from the ground. Thirdly, even if there is a possibility to observe at the mid-infrared region in space, those rotational transitions require too much energy to be excited by collisions at the typical temperature of 10-30K in molecular clouds. Therefore another tracer of the dense ISM is needed. Usually the molecule most used to trace H_2 is the next most common cloud molecule – carbon monoxide (CO). The ratio between CO luminosity and H_2 mass is almost constant, with a H_2/CO ratio of $\sim 10^5$. The 2.6 and 1.33 mm CO lines are typically used, since hydrogen does not normally emit at these frequencies. The energy differences of these transitions are such that wavelengths are located in the sub-millimeter and millimeter range, i.e. the gigahertz region of the radio spectrum, where ground based observations are possible due to quite good transparency of the Earths atmosphere at these wavelengths.

The first attempt to estimate the GMCs mass spectrum in the Milky Way using CO-observations was done by Solomon et al. (1987). In the inner disk of the Milky Way, the mass distribution follows a power law $dN/dM \propto M^{-3/2}$ (see Figure 1.2). More recent surveys of molecular clouds throughout the Local Group find that the mass spectrum also follows a power law, but the indices are steeper than in inner Milky Way (Engargiola et al. 2003). The mass spectrum may be the only feature of the molecular cloud population that varies between systems, since other cloud properties (e.g., cloud radius and line width) obey the relationships established in the Milky Way (Wilson & Scoville 1990; Rosolowsky et al. 2003). Careful attention to accurate determination of the parameters of the mass spectrum is critical in using the mass spectrum to quantify differences between cloud populations. In addition, the empirically derived mass distribution is an important parameter for theoretical and modeling work. Several studies aim to reproduce the mass distribution of molecular clouds (see Figure 1.3, Elmegreen & Falgarone 1996; Vazquez-Semadeni et al. 1997; Wada et al. 2000) or use the mass spectrum as inputs to models (Krumholz & McKee 2005). Most of these studies focus on the canonical value of adopted from the inner Milky Way, neglecting any variation in the distribution. Judging from the scope of these other studies, measuring the mass distribution of molecular clouds is essential for understanding both cloud formation and the importance of star-forming clouds in regulating large-scale star formation.

Extragalactic Molecular Clouds

Why study extragalactic molecular clouds? Since many factors that operate on kiloparsec scales may be involved in molecular cloud formation and the regulation of large-scale star formation, observational efforts to study these phenomena must also span large physical scales. Our location within the Milky Way allows for detailed observations of individual molecular clouds and the star formation within them. However,

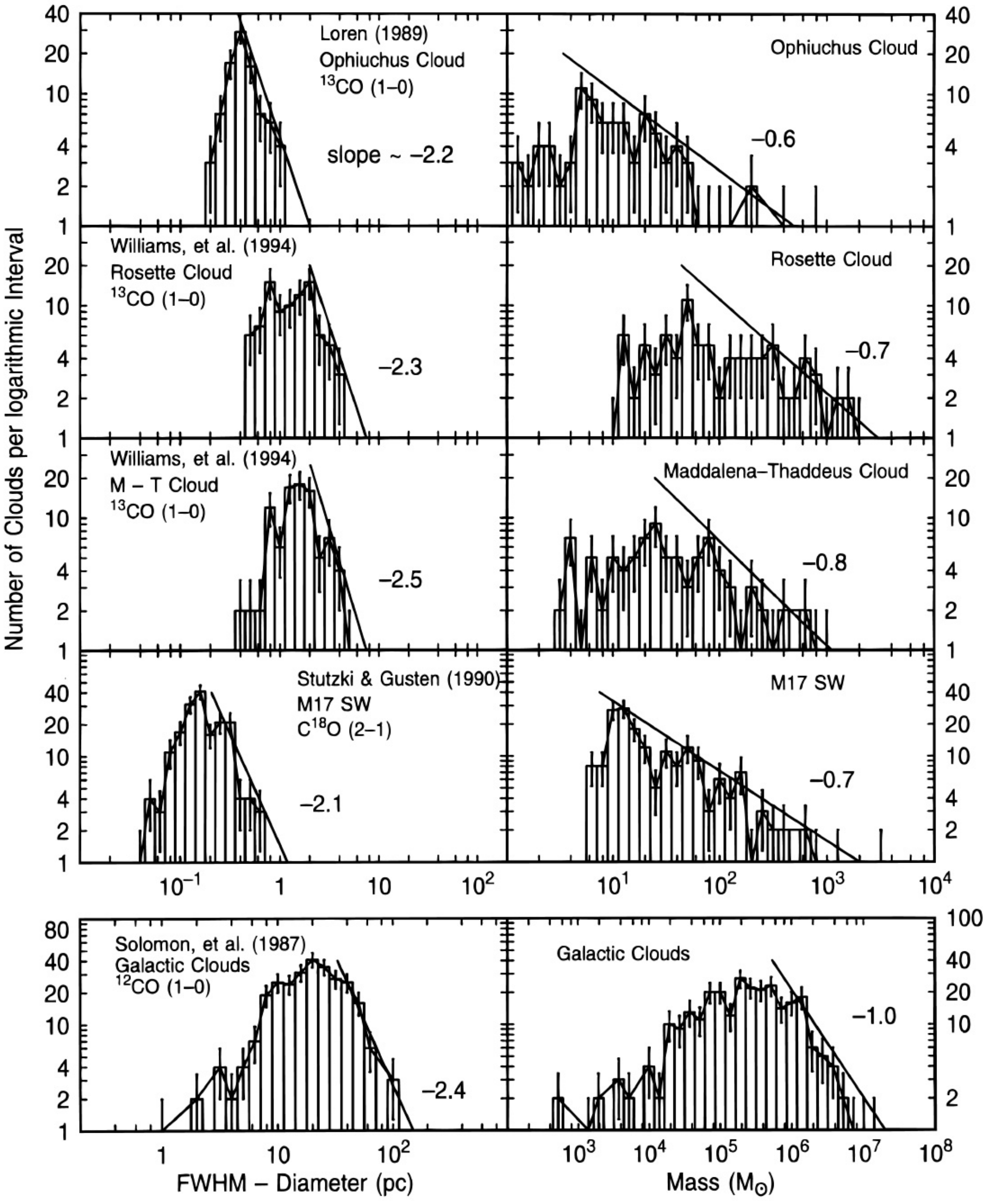

FIGURE 1.3: Size L and mass M distributions in logarithmic intervals from published surveys with large numbers of clouds (Elmegreen & Falgarone 1996)

studies of large numbers of molecular clouds and their relation to other components of the galaxy are complicated by our position in the Galaxy. Line-of-sight blending makes relating molecular clouds to other components of the ISM and to stellar populations particularly difficult. Observations of extragalactic molecular clouds can provide a complementary picture to studies of clouds within the Galactic disk. Owing to an external perspective, exploring the relationships between molecular clouds and other important components of the star-forming disk (the H I gas, OB associations, H II regions, supernova remnants, and the magnetic field) is much easier.

For the time being, there have only been a few studies of extragalactic molecular clouds with relatively high resolution. M33 has been studied by Engargiola et al. (2003), M64 by Rosolowsky & Blitz (2005), and M31 by Rosolowsky (2007). The study of the Magellanic Cloud has been done by Mizuno et al. (2001b,a).

Using observations of extragalactic molecular clouds and comparing them to the Milky Way one, will allow us to answer some fundamental questions, namely: what is the mechanism of cloud formation across the galaxies ? Are clouds in other galaxies different from the Milky Way ones ? What is the mass distribution of those clouds ?

1.2 Diffuse Interstellar Bands (DIBs)

Interstellar medium is not homogenous and has rather complex clumpy structure. Those clumps, or so called interstellar clouds, are the accumulations of gas, plasma and dust. They are found both all over our own galaxy and in other galaxies, and continually evolving as new stars form, and are enriched by material ejected from dying stars that was formed during stellar nucleosynthesis. While precise definition of the term "cloud" is a complicated question, usually it's assumed that a typical interstellar cloud is a structure/area which is denser than average region of the interstellar medium. The ISM consists mainly of three types of clouds: dark clouds (Av $>$ 5 mag), translucent clouds (1 mag $<$ Av $<$5 mag), and diffuse clouds (visual extinction, Av $\sim$ 1 mag). Interstellar clouds are neither uniform nor dynamically quiescent on long time-scales.

Hydrogen is the most abundant element in the ISM. At the same time, over the past 40 years a large number of gas-phase molecules, ranging in size up to more than 10 atoms have been discovered in the clouds. Depending on the temperature, density, and size of a given cloud, the hydrogen in it can be neutral (H I regions), ionized (H II regions) , or molecular (molecular clouds). Neutral and ionized clouds are referred to diffuse clouds, while molecular clouds are typically associated with dense clouds.

One of the most interesting and puzzling components of the interstellar clouds are the diffuse interstellar bands (DIBs). The first discovery of diffuse interstellar bands (DIBs) has been reported by Heger (1922). She used just panchromatic photographic emulsions to record the spectra, however the new interstellar lines could be vividly observed in the yellow and red spectral regions.

The two new quite strong spectral features she discovered were significantly broader than the neighboring interstellar sodium lines and were centered close to 5780 and 5797 Å. Later on Merrill (1934, 1936), Beals & Blanchet (1937), York (1971), and Herbig (1975) and several other independent authors has confirmed that the lines have interstellar nature. Herbig (1975) designated 39 spectral lines as certain DIBs and a few others as "possible". It should be noted that the number of published DIBs strongly depended on the signal-to-noise ratio (S/N) of the spectra. Figure 1.4 shows the diffuse interstellar bands plotted as spikes atop the extinction curve for HD 183143.

At the time of photographic observations DIBs were measured mostly in the spectra of heavily reddened stars where the optical depth of the interstellar medium is large enough to make such extremely shallow features visible. In such cases, usually there are many individual clouds located along the line of sight and each cloud has its own set of physical parameters. These separate clouds were discovered as distinct Doppler components, in high-resolution profiles of strong interstellar absorption lines, such as Na i D1 and D2 or Ca ii H and K. As early as the 1930s, the question was raised whether individual interstellar clouds have identical spectra and, thus, identical physical parameters.

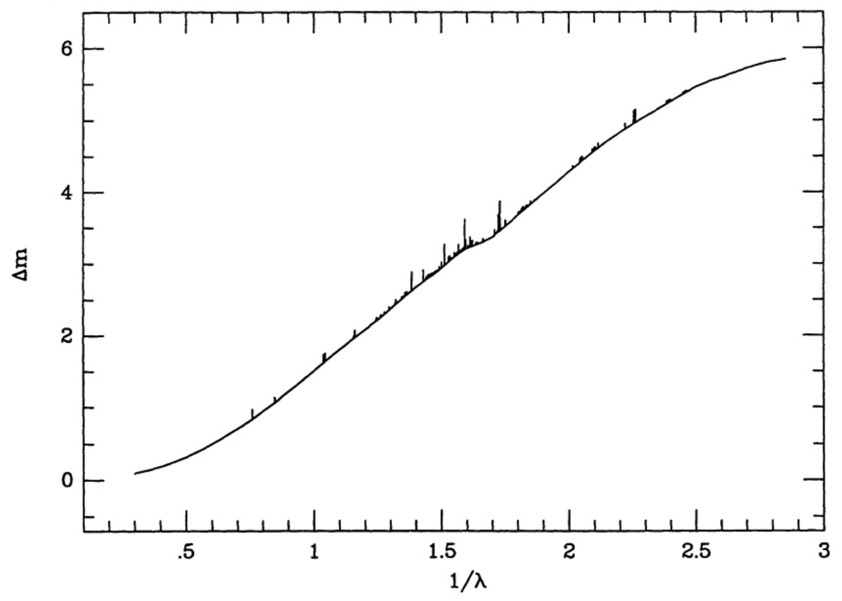

Figure 1.4: The interstellar extinction curve for HD 183143 with the diffuse bands represented as spikes extending above it. The extinction curve is from van Breda & Whittet (1981), scaled to the color excess of HD 183143 of $E(B-V) = 1.28$. Several of the broader DIBS are shown of width equal to FWHM (Herbig 1975).

DIBs and reddening

Studying interstellar lines in the yellow and red regions of the optical spectra Merrill & Wilson (1938) proposed the idea of the dependence of DIBs on color excess (see Figure 1.5). They also pointed out that the DIBs might be produced by "small solid particles". Numerous follow up measurements showed good correlation between DIBs and the optical thickness of the interstellar extinction derived from color excess (strengths of DIBs have a factor of two dispersion about a mean relationship). Based on broad band infrared photometric measurements of 105 stars (which have diffuse interstellar bands in their spectra) Sneden et al. (1978) demonstrated that DIBs strengths show as large a scatter with the infrared color excesses as they do with $E(B-V)$. On the other hand, there are cases when DIBs strengths in some directions depart from the mean dependence upon color excess.

Fast development of digital detectors in the 1980s has opened a new window to spectroscopical studies of DIBs. High signal-to-noise linear CCD and Reticon detectors allowed to overcome and understand many systematic errors introduced by photographic measurements (Schmidt-Kaler et al. 1980). However, having such shallow spectral lines DIBs are still very sensitive to errors such as is the continuum level, etc. Surprisingly, the major increase in the accuracy of DIBs measurements did not greatly reduce the scatter around a mean regression line relation DIB strength to color index excess.

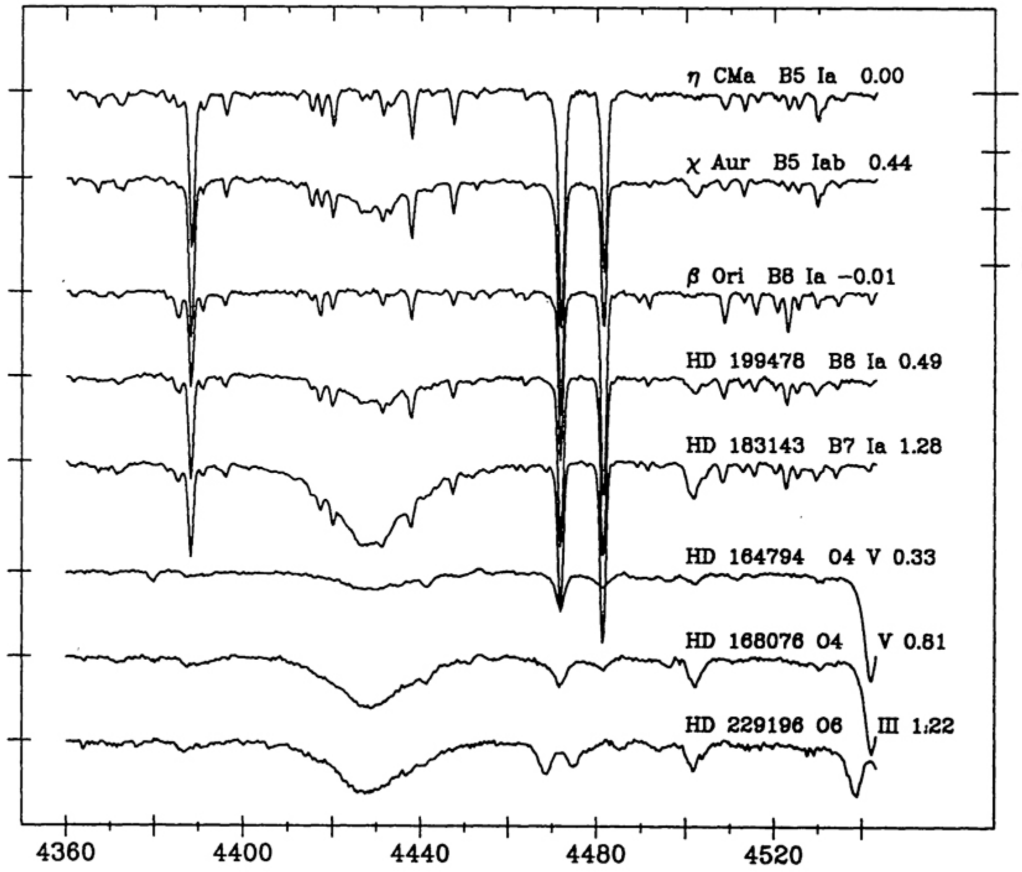

FIGURE 1.5: The region of the diffuse band λ 4428Åin stars reddened and unreddened. Spectral types and $E(B-V)s$ appear on the right. All the spectra have been shifted in wavelength to that their stellar lines coincide (Herbig 1975).

Herbig & Soderblom (1982) demonstrated that the profiles of DIBs can be modified by Doppler splitting. The same results has been obtained later by Westerlund & Krelowski (1988b), but they published the Doppler broadening of some DIB profiles only. These observations showed how difficult is to determine intrinsic profiles of the DIBs free of any Doppler splitting (Westerlund & Krelowski 1988a) in order to make a comparison with laboratory spectra. Such kind of profiles can be observed only in single/isolated clouds located at the light of sight, where reddening is low to moderate.

Spectrographs, equipped with CCD detectors also made possible to probe DIBs in individual clouds. From analysis of high resolution and very high signal–to–noise–ratio (S/N) combined spectra of a sample of stars (σSco, ζOph, ζPer, and HD 40111) Krelowski & Walker (1987) demonstrated that the the relative strengths of the prominent DIBs 5780 and 5797 Åwere quite different. Similar results were published soon after by Krelowski & Westerlund (1988) and Josafatsson & Snow (1987). This is an interesting result, meaning that the DIBs do not have a common origin and individual clouds may differ both in DIB intensity ratios and in the shapes of the extinction curves produced by interstellar dust.

It is usually easier to look for new DIBs in the spectra of heavily reddened stars since the strengths of the features generally increase with reddening. However, while searching for new features in such spectra, we cannot determine their wavelengths accurately since the sight lines are probably intersected by many different clouds with different line-of-sight velocities (Herbig & Soderblom 1982). Therefore it is important to establish DIB rest wavelengths in very high S/N spectra of moderately reddened stars as free as possible from Doppler splitting of the interstellar atomic lines.

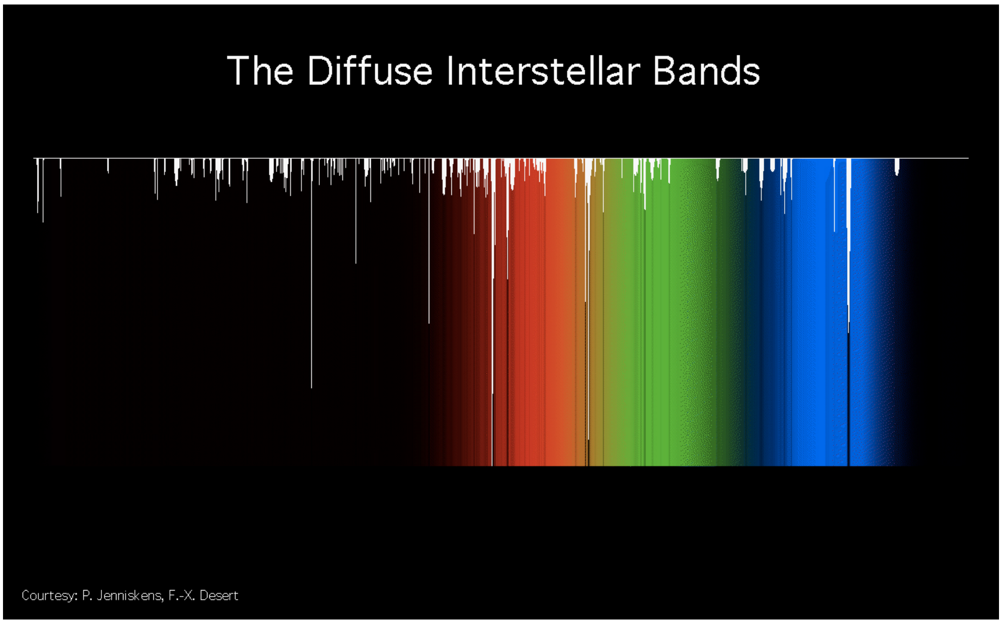

Figure 1.6: Relative strengths of observed diffuse interstellar bands.

DIBs carriers problem

Identification of diffuse interstellar bands is the longest standing unsolved problem in all of spectroscopy. The set of more than 300 features (Galazutdinov et al. 2000) contains some really diffuse, i.e. as broad as ∼60 Å DIBs (4430, 6177) as well as many really narrow (less than 1 Å), sometimes very weak features (see Figure 1.6). The only common property of DIBs is the lack of identification; their carriers remain unidentified since the discovery of the first two: 5780 and 5797 diffuse bands (Heger 1922).

Many carriers have been proposed, but for none of them convincing arguments exist so far (for a review see Fulara & Krelowski 2000). The most promising hypothesis are:

- long carbon chains, like polyacetylenes (Douglas 1977)
- PAH cations (Allamandola et al. 1999; Salama et al. 1999)
- fullerenes (Foing & Ehrenfreund 1997)

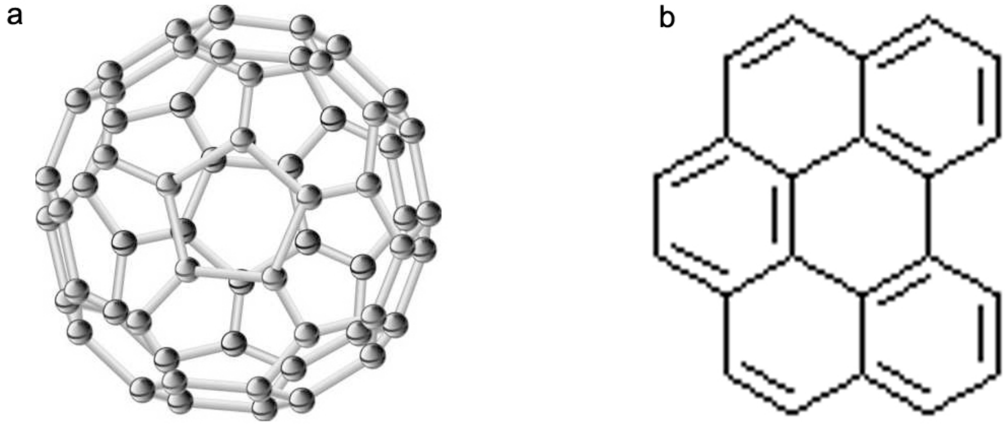

FIGURE 1.7: The fullerene $C60$ molecule (*a*), and a cationic simple PAH (Benzo(ghi)perylene) (*b*).

It is rather commonly believed that DIBs are carried by some complex, carbon–bearing molecules (Fulara & Krelowski 2000) but no certain identifications exist until now (see Figure 1.7)

Douglas (1977) proposed linear carbon molecules as possible carriers of the DIBs. Bare carbon chains, homo-nuclear species, do not create rotational transitions observed at radio wavelengths and thus only their electronic or vibrational spectral features can be compared with those observed in the spectral range from vacuum UV until far infrared. The first pure carbon molecule, the two–atom homo-nuclear C_2, was discovered by means of near infrared spectroscopy in 1977 by Souza & Lutz (1977) in the spectrum of the opaque cloud obscuring the star Cyg OB2 No. 12. Until now the most extensive survey of $\mathrm{C_2}$ abundances, based on the Phillips 2–0 band was published by van Dishoeck & Black (1989). The more recent compilation of Federman et al. (1994) was able to give estimates of the $\mathrm{C_2}$ column densities towards 32 reddened stars plus a couple of upper limit estimates. The next member of the possible family of carbon molecules C_3 is much more difficult to be observed. It was discovered by Hinkle et al. (1988) in the infrared spectrum of the circumstellar shell of the star IRC +10216. The high precision structure of this band was found towards three nearby reddened stars in July 2000 (Maier et al. 2001). The abundance of this species seems to be an order of magnitude below that of C_2.

Longer linear hydrocarbons are potential candidates for being DIB carriers. However, their spectral features, acquired in laboratory gas–phase experiments do not match any of the observed DIBs (Motylewski et al. 2000). Anyway, some of the profiles of the observed DIBs resemble to a certain extent the experimental ones (they are usual wavelength–shifted), which makes the hypothesis attractive and further experiments are going on (mostly in Leiden laboratory of H. Linnaertz). Also polycyclic aromatic hydrocarbons (PAHs) are considered as attractive candidates; however, the recent attempts to identify any of (simplest) PAHs as DIB carriers gave the negative result (Salama et al. 1999). Diffuse bands' carriers are believed to be concentrated in neutral interstellar clouds which are revealed by KI line or the methylidyne (CH) features (Megier et al. 2005).

DIBs detection

There are some commonly accepted principles/conditions which facilitates in detection of DIBs in stellar spectra:

- the best choice would be a relatively bright star of an early spectral type (they have relatively smooth continuum in optical part of the spectra with only few strong stellar - ideal case to look for shallow DIBs lines).
- relatively big telescope and high-resolution optical or near-infrared spectrograph capable to produce spectra of sufficiently high resolution ($R > 30000$) and of high signal–to–noise–ratio ($SNR > 200$).
- presence of a transparent interstellar diffuse cloud(s) in line of sight causing reddening of the target star.

The most recent high-quality observational data and the parallel theoretical studies allow us to define some constraints on the DIBs problem:

(i) the presence of DIBs is related to the color excess, in the sense that the lack of reddening implies the absence of the DIBs; but the DIBs intensity along one line of sight is only loosely correlated to the value of the reddening in that direction,

(ii) the DIBs intensity is not strongly correlated with the 2200 angstroms extinction bump: dust and carriers of DIBs, although coexisting in the inter- stellar medium, have an independent history,

(iii) the line profile of the DIBs seem to be quite stable,

(iv) the DIBs seem to be generated not by a single agent but by several carriers; they can therefore be grouped into families, the members of which show well-defined intensity ratios (e.g., 5780 and 5797 DIBs have different carriers because the ratio of their intensities may substantially vary from one line of sight to the other).

All known DIBs form very in-homogenous sample. Some of them are relatively strong, contrary to the others which are extremely weak. There exist DIBs which are narrow, with widths of about 1 angstrom (e.g. 5797), but there are also very broad DIBs, with widths of about 20 angstroms (e.g. 4430).

The identification of a feature as interstellar cannot depend on a single spectrum. As far as possible several tests must be applied: are the suspected features stationary in spectra of spectroscopic binaries ? Are their profiles independent of stellar rotational velocity? Are their intensities correlated with a color excess? Are they absent from the spectra of unreddened stars ? Does the wavelength separation from interstellar atomic lines remain constant ? Do they have counterparts in synthetic spectra with parameters resembling the program stars?

1.3 Goal and structure of this thesis

The goal of this thesis is two fold: 1) at the largest scales we want to explore a new technique to detect and analyze the basic large scale properties of giant molecular clouds in nearby galaxies via near infrared (NIR) color maps. At the smallest scales we want to 2) investigate the detailed physical and chemical properties of diffuse interstellar clouds. The thesis is structured in the following way:

In Chapter 2 we present our study of molecular clouds in the giant elliptical galaxy NGC5128 (Centaurus A). We develop a novel method of tracing molecular hydrogen using dust as a tracer. Applying a wavelet based multi-scale technique we detect the clouds on near-infrared color–color maps of the galaxy. We derive basic properties of 436 molecular clouds, such as sizes, masses and their apparent orientations. For the first time for this galaxy, the GMC mass spectrum has been obtained. It turns out to be steeper, then the one of GMCs in the Milky Way galaxy.

In Chapter 3 we present a discovery of a "peanut-shape" structure in the nucleus region of the giant elliptical galaxy NGC1316 (Fornax A). The original idea of determining the mass spectrum of the GMCs did not work out due to insufficient data quality. We estimated the diameter of the structure, which turns out to be 0.76 kpc ($\sim 8''$) and projected minor axis of about 430 pc. The analysis of previously published and our new kinematical data shows that discovered brightness excess might be explained by presence of a kinematically decoupled core in the inner $4''$ region of Fornax A.

In Chapter 4 we present a discovery of a new kind of interstellar clouds – Ca-Fe clouds. These are rare (just a few examples among ~ 300 lines of sight) objects with the Ca I 4227 Å, Fe I 3720 Åand 3860 Ålines stronger than those of K I (near 7699 Å) and Na I (near 3302 Å). Apparently they occupy different volumes from the well-known interstellar H I clouds where the K I and ultraviolet Na I lines are dominant features. We have found the CaFe clouds only along sight-lines toward hot, luminous (and thus distant) objects with high rates of mass loss.

In Chapter 5 we analyze intensity ratios of unsaturated methylidyne (CH) A–X, B–X and C–X bands and suggest inconsistency of the published oscillator strengths. While the latter are consistent for the main B–X and C–X transitions we suggest the new oscillator strength of the CH A–X band 4300.313 Å to be equal to $434 \pm 31 \times 10^{-5}$. We also estimate methylidyne column densities, using the new, consistent system of the oscillator strengths.

In Chapter 6 we study spatial correlations of some DIBs and simple molecules. We find that radial velocities of CH, CH$^+$ features and two narrow diffuse interstellar bands: 6196 and 4964 suggest that 6196 DIB carrier is spatially correlated with CH$^+$ while 4964 DIB carrier prefers environments where CH molecule is abundant.

2

Giant molecular clouds in NGC 5128 (Centaurus A): the mass spectrum

to be submitted to Astronomy & Astrophysics
Beletsky, Y., Alves, J., Kainulainen,J.

Abstract

Context: The physics of the formation of GMCs is one of the major unsolved problems of the interstellar medium. A study of GMCs in external galaxies can address the fundamental questions of whether the molecular ISM in external galaxies is organized differently than in the Milky Way and whether GMCs play the same central role in massive star formation as in the Milky Way, and are then responsible for galaxy evolution.

Aim: To investigate the spatial structure and properties of giant molecular clouds in NGC5128.

Method: We use a wavelet-based technique of locating clumpy structures on the images and apply it to near-infrared maps of the Centaurus A galaxy (NGC5128). The masses of the molecular clouds are calculated using the dust column density as a tracer of N(H_2).

Results: For the first time we derived a mass spectrum for GMCs in NGC5128, in a way which does not rely on CO observations. The obtained power index $\alpha = -2.31$ corresponds to a quite steep slope, indicating that a large number of low mass clumps were found. The value of -2.31 is in good agreement with the results for M33 ($\alpha =$ -2.6) and steeper than that found in the inner Milky Way ($\alpha =$ -1.5).

2.1 Introduction

The physics of the formation of GMCs is one of the major unsolved problems of the interstellar medium. Although many papers have been written on the subject (see for a review Elmegreen 1993, and references therein) it is not yet known what the dominant formation mechanism is, or even what the relative importance of gravity, shocks, and magnetic fields are in the cloud formation process. Our present understanding of molecular clouds and of star formation within them is almost exclusively based on Milky Way observations. This is a natural result of the much higher sensitivity and much better angular resolution required for comparable observations of external galaxies. It is only fair to say that our knowledge is still rather limited and is often not based on a derivation from fundamental principles, but is largely phenomenological.

One avenue for testing GMC formation theories is to study molecular clouds in a wide range of environments, ideally from a view point outside the galaxy's plane, and to determine which aspects of the environment set the cloud properties. A study of GMCs in external galaxies can address the fundamental questions of whether the molecular ISM in external galaxies is organized differently than in the Milky Way and whether GMCs play the same central role in massive star formation as in the Milky Way, and are then responsible for galaxy evolution. Moreover, in an external galaxy we can easily disentangle molecular clouds and assess their basic properties and star forming status, as opposed to the confused "inside view" of Galactic molecular clouds. Ironically, GMCs are perhaps the most overlooked parameter in extragalactic star formation studies, and only recently, with the development of millimeter (CO) interferometry, they are beginning to be consistently incorporated into the picture.

Determining cloud properties from observable quantities such as intensities and profiles of certain spectral lines used as the standard tracers, always requires additional assumptions, justified largely only because proven to give consistent answers for the local Milky Way clouds. To what degree these assumptions also hold for the interstellar matter in external galaxies, given their different chemical composition and environment, is not a priori clear.

The most common techniques widely used to study properties of molecular clouds employ the following tracers : i) the integrated intensity of emission lines of various molecular or atomic tracers, especially CO and HI, ii) the thermal emission of dust grains at far–IR and sub-mm wavelengths, and iii) the extinction of the near–IR light from background stars. However, a given molecular line, for example, is most sensitive to a limited range of gas density, above the critical excitation density, and below a density where saturation sets in due to the large optical depth. The method based on far-infrared dust observations is highly dependent on the temperature of the dust.

We propose to study extragalactic GMCs tracing the dust content of a galaxy and quantitatively deriving the dust mass using near-infrared images. Therefore we assume that the dust column density will trace N(H_2). There are good theoretical arguments (Whittet 1992) and observational evidence to guarantee that this is a fair assumption. In fact, Alves et al. (2001) show that the gas/dust in the dense cloud Barnard 68 is similar to the canonical value derived for the diffuse ISM (Bohlin et al. 1978). More recently, comparing Hydrogen column density to dust column density along line-of sights to young stars in Ophiuchus extincted by as much as 30 mags of extinction, Vuong et al. (2003) finds that dust and gas are linearly correlated down to large cloud depths. Among the advantages of this method are its independence of the temperature of the dust and excellent resolution (<0.2″; e.g., Regan & Mulchaey 1999)

While our present knowledge about dust in other galaxies is still very limited, numerous studies show striking similarity between properties of extragalactic dust and the dust in the Milky Way (Finkelman et al. 2008, and references therein). This is really interesting especially taking into account huge variety of galaxies and the possible range of physical conditions of the dust.

The mass distribution (or the mass spectrum) of molecular clouds is one of the basic characteristics of their population. Using various independent approaches, such as principal component analysis (Heyer & Schloerb 1997), delta variance techniques (Stutzki et al. 1998), spectral correlation functions (Rosolowsky et al. 1999), multifractal analysis (Chappell & Scalo 2001), etc., it has been shown that interstellar gas seems to be scale-free. However, applying intensity contouring drawing (Williams et al. 1994) or gaussian fit to absorption spectral lines (Spitzer & Jenkins 1975), the interstellar medium looks like a collection of discrete clouds. These two interpretations have led to different models for star formation and the origin of gas structure. Scale-free models typically involve turbulence and self-gravity (see Elmegreen 2002, and references therein). Therefore the mass spectrum of molecular clouds is the key contact point between those two views, providing the clouds can be isolated and well defined. Such the spectrum is also important for bound star clusters, which are better defined (Elmegreen et al. 2000), and for individual stars, whose masses are probably proportional to the primordial clump masses (Motte et al. 1998; Testi & Sargent 1998). In this paper we focus on Centaurus A (NGC5128) galaxy. Our aim is provide the best estimate to date of the mass distribution of molecular clouds in this galaxy.

2.2 The target selection

NGC 5128 (Centaurus A), at an assumed distance of 3.5 Mpc (Hui et al. 1993), is the nearest giant elliptical galaxy and is remarkable in several respects. The optical appearance is dominated by a dramatic warped dust lane at least 12.5 arcmin in east-west extent, which effectively bisects the main body of the elliptical galaxy and almost completely obscures the nucleus and all optical structure in the inner 500 pc (see, e.g., Schreier et al. 1996). The outer isophotes of Centaurus A are markedly elongated in P.A. 25. Faint shells, associated with both H I and CO emission, are evident in these outlying parts (Malin et al. 1983; Schiminovich et al. 1994; Charmandaris et al. 2000). The somewhat chaotic dust lane and especially the shells are strong evidence of a relatively recent merger (Baade & Minkowski 1954; Graham 1979; Tubbs 1980; Schreier et al. 1996; Israel 1998), which is generally believed (see Marconi et al. 2000, and references therein) to be responsible for the nuclear activity. Hα and molecular line observations (see, e.g., van Gorkom et al. 1990) indicate that the nucleus is surrounded by a rapidly rotating massive inner disk of radius 2 kpc with a pronounced warp

(Nicholson et al. 1992; Quillen et al. 1992), a scenario that is supported by modeling of the structure of the obscuring dust seen in near-infrared (Quillen et al. 1993) images.

It is a powerful radio source, with a double-lobed structure extending approximately 3.5×8.5 degrees on the sky (Bolton et al. 1949; Clarke et al. 1992; Tingay et al. 1998). At the other extreme of scales, a central source less than 0.4 mas (0.008 pc) in extent (Kellermann et al. 1997) is prominent on radio through X-ray images. This compact object feeds subparsec-scale relativistic outflows that are approximately aligned with, and clearly the generators of, the vast outer radio lobes (see, e.g., Tingay et al. 1998).

FIGURE 2.1: Tricolor ($JHKs$) composite image of the NGC 5128 based on SOFI/NTT data. Colors: *Red* - Ks, *Green* - H, *Blue* - J

2.3 Observations and Data Reduction

The observations were made on the 5th and 6th of March 2001 using the near-IR imager/spectrometer SOFI ($J\,(1.25\mu\mathrm{m})$, $H\,(1.65\mu\mathrm{m})$, and $Ks\,(2.162\mu\mathrm{m})$ bands) on the 3.5 m NTT telescope in La Silla, Chile. The SOFI detector is a Hawaii HgCdTe 1024×1024 array. We used the SOFI large-field mode, with a pixel scale $0.29''$per pixel and a field of view $4.9' \times 4.9'$. Conditions during the observations were generally clear with a typical seeing better than 0.7 arcsec. The integration times were 30×10 s, 77×10 s, 60×10 s for the J, H and Ks band respectively. The observations were carried out using the “jitter” technique. Jittering was controlled by the automatic jitter template, which produce a set of dithered frames. Offsets are generated randomly within a box of 40×40 arsec centered on the galaxy center.

Due to presence of thermal emission from the sky in NIR it is important to measure carefully the sky background which can vary spatially and temporarily. Taking into account the large spatial size of the galaxy, the sky level cannot be determined on the object frames directly. Control fields a few arcminutes away from the galaxy center have been observed in order to construct median-averaged sky frames.

A classical near-infrared data reduction procedure was adopted. Dark frame subtraction, sky subtraction, flat fielding and illumination correction were applied using the IRAF[1] CCDRED package. We used illumination correction frames and the bad pixels masks, available from the ESO web page. For each object frame a master sky frame was constructed by median filtering of all adjacent sky frames. Then the master sky frame was subtracted from the corresponding object frame. The final sky-subtracted images were aligned and combined using JITTER routine in ECLIPSE (Devillard 1997a). We smoothed the image in each observed band to yield the resolution of the waveband with the poorest seeing.

The World Coordinates System in the images was secured using the *imwcs* routine written by Doug Mink and stars from the Two Micron All Sky Survey (2MASS). The resulting astrometry is accurate to within an arcsecond in right ascension and declination.

We performed photometric calibrations using 2MASS sources available in the field. The instrumental magnitudes of isolated stars were measured in a 7-pixel ($2''$) radius aperture using the IRAF task PHOT. The magnitude zeropoints of the corresponding exposures were computed as the difference between the instrumental and the cataloged magnitudes. The zeropoints are compatible with the other results published on the NTT/SOFI web page. Finally, the images were calibrated pixel-by-pixel using these calibration relations. The final color maps were constructed by subtracting the K-band image from the J- and H-band images accordingly.

The corresponding tricolor composite image compile of the reduced data frames is displayed on Figure 2.1.

---

[1] *Image Reduction and Analysis Facility* (IRAF) is distributed by NOAO, which is operated by AURA, Inc., under contract to the NSF.

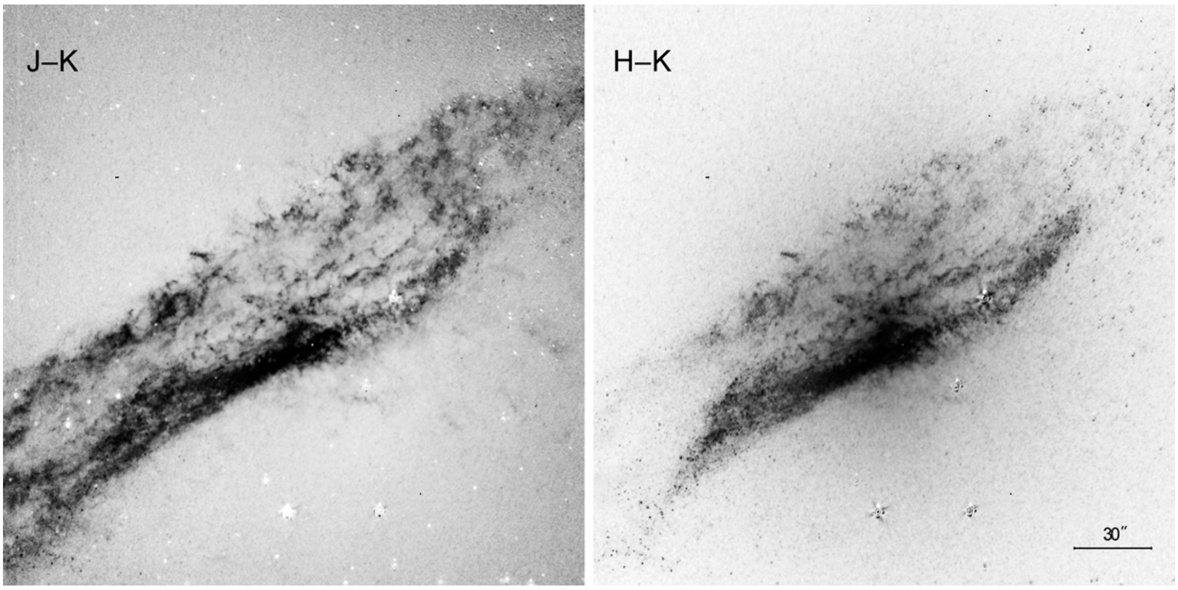

FIGURE 2.2: $J - K$ and $H - K$ color maps of Centaurus A (*left to right*, respectively). North is up, and East is to the left.

2.4 Clouds Identification: multiscale approach

Molecular cloud observations often show a complicated, self similar structure over a wide range of spatial scales. A main problem is the quantitative description of these structures.

The next step is to extract the molecular clouds from the obtained color maps (see previous section) and compute their masses. The molecular clouds appear as small smoothed dots on the image. Their typical size ranges from 5 to 10 pixels (corresponding from 2 to 4 arcsec). On the image, the body of the Centaurus galaxy is predominant in size and amplitude. The body is made of arms and complex regions with details larger than typically 30 pixels. In some cases, the distinction between molecular clouds and faint details of the galaxy is not obvious for the eyes.

The extraction of the molecular clouds should be done after the contribution of the body of the galaxy has been removed, in order to compute proper flux with no over estimation. The classical source extraction packages are able to compute the sky background before extracting the sources. This estimation relies on a *background parameter* specifying the size in pixels of a median convolution applied to the image (typical values are equal to several hundreds of pixels). This estimation is robust when the sky background is only a very smooth contribution to the image. Point like sources are not affected by this estimation, and their flux are measured with no bias. In case of the Centaurus A image, the estimation of the body of the galaxy must be done with a small background parameter which provides a biased estimation. One reaches the limitation of classical source extractions.

We identified all sources (molecular clouds, body of the galaxy) applying multi-scale approach (Starck et al. 1998) and using wavelet transformations (Bijaoui et al. 1998).

The *à trous algorithm* has been employed since it has important advantage over many other extensions of the classical discrete wavelet transforms (Mallat, 1989) – it does not favor any direction in the image and maintains the sampling at each scale.

At a given scale, a number of wavelet coefficients decimated by a factor 4 have been derived. Due to the decimation the transform depends on the origin. Since in case of the *à trous algorithm*, no direction is favored, no decimation occurs and the shift-invariance is verified. In this method, the sampled data, F (k , l), are assumed to be the scalar product of a continuous function F with a scaling function ϕ:

$$F(k,l) = \langle \mathcal{F}(x,y), \phi(x-k, y-l) \rangle \, ;$$

F(k,l) is also designated as F(0,k ,l) in order to be compatible with the equations that follow. The following scalar products give the smoothed image of F(k,l) at the scale i:

$$F(i,k,l) = \frac{1}{4^i} \left\langle \mathcal{F}(x,y), \phi\left(\frac{x-k}{2^i}, \frac{y-l}{2^i}\right) \right\rangle ,$$

where ϕ is chosen to satisfy the dilation equation (Strang, 1989).

$$\frac{1}{2}\phi\left(\frac{x}{2}, \frac{y}{2}\right) = \sum_n \sum_m h(n,m)\phi(x-n, y-m),,$$

where h is the low pass filter (Bijaoui, 1995). The wavelet coefficients are chosen as the difference between two smoothed images. They correspond to the details lost between two scales:

$$W(i,k,l) = F(i-l,k,l) - F(i,k,l).$$

We selected the following B-spline scaling function:

$$\phi(x,y) = B_1(x)B_2(y),$$

where B_1 is the B-spline function of degree one (Unser1992). Figure **??**) shows the scaling function ϕ (on the left) and the associated wavelet function ψ (on the right).

The wavelet transform space (WTS) is a three-dimensional space. Each object on an image occupies a physically connected region, where each pixel of the region can be linked to the others (Bijaoui, 1995). The connectivity in direct space has to be transferred to the WTS. At each scale, structures associated with an object are also connected. Therefore all the structures form a hierarchically organized three-dimensional set, where for a given scale structures are linked to smaller structures of the previous scale. Such a set provides the description of an object in the WTS. Figure 2.4 shows a schematic structure of the multi-scale model definition.

As a first step we apply the wavelet transformation to the image (i.e., the *à trous algorithm*). Then, in order to identify the statistically significant coefficients we perform a thresholding in the WTS. A wavelet coefficient is significant if its value is such that the probability to be only due to the noise is smaller than a given thresholding ϵ.

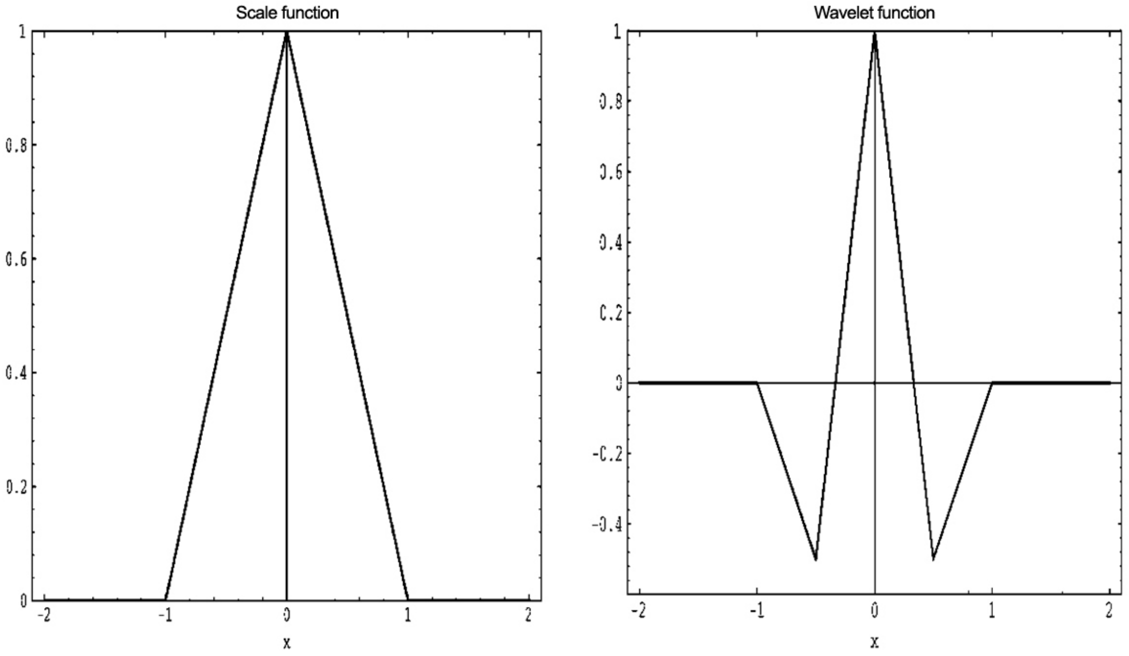

FIGURE 2.3: B-spline scaling function (on the left) and the associated wavelet function ψ (on the right).

They are gathered in connected fields using a scale-by-scale segmentation procedure in order to define the object structures. At a given scale the thresholding produces connected fields. Each one can display many local maxima coefficients. Each field is decomposed in different sub-fields using a ridge line algorithm in order to get a decomposition for which we have only one maximum, i.e. one peak, per field. An inter-scale connectivity graph is established and the object identification procedure then extracts each connected sub-graph corresponding to 3D connected sets of pixels in the WTS. Using the object definition, these can be associated with the objects. Finally, from each set of pixels the corresponding object image can be reconstructed using MVM algorithms (Bijaoui et al. 1998).

2.5 GMC sample selection

Although dust is a very good tracer of molecular hydrogen and it has been successfully proved by studies of molecular clouds in the Milky Way (Alves et al. 2001), however some care is needed in case of extragalactic molecular clouds. The problem, which does not affect Galactic works (i.e. Lada et al. 1994; Alves et al. 2001) – we do not know the relative geometry of dust clouds and stars along the line of sight. It is also unknown, how deep the clouds are embedded in the galaxy. For the stars located in front of the cloud, observed reddening will be reduced in comparison to the foreground screen geometry. The second problems is the scattering of light. The observed light is

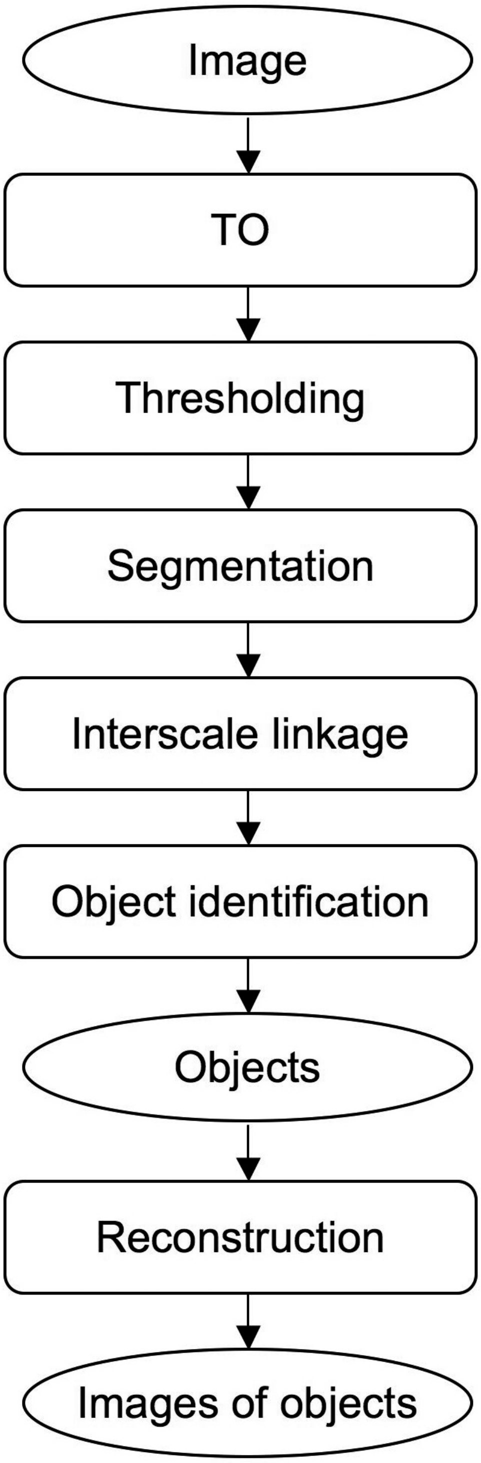

FIGURE 2.4: Algorithm of the multi-scale model.

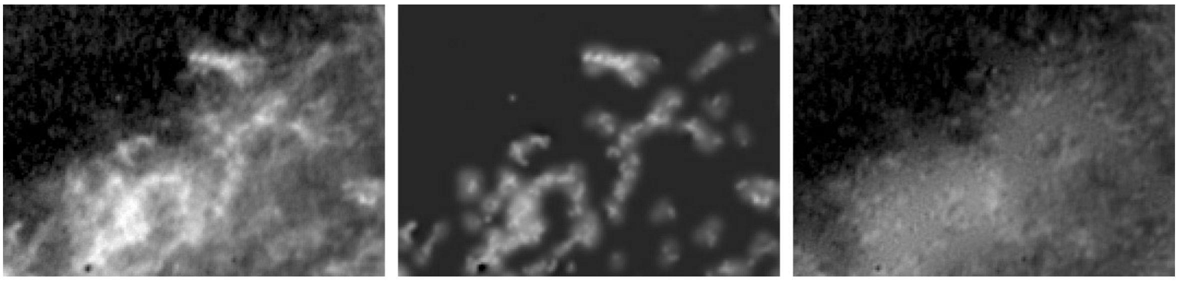

Figure 2.5: Bi-cubic wavelet transform.*Left:* A fragment of the NGC 5128 $J-K$ color map, *Middle:* wavelet transform of the fragment, *Right:* the result of subtraction of the wavelet transform from the $J-K$ color map fragment.

coming to the observer from all all directions of the galaxy, experiencing multiple scattering. Since scattering is wavelength dependent, the observed colors will be affected accordingly. Those two outlined problems makes much more difficult proper derivation of actual columns densities and some modeling might help to overcome it (Kainulainen et al. 2007).

Still we can try to minimize those problems by careful selection of targets which have prominent dust lanes in the optical. Since optical imaging (especially B-band) is very sensitive to the dust, we can use them as a "tracers" of dust located in the foreground, therefore minimizing chances of picking up more distant and embedded clouds.

In order to better constrain location of the region of NGC5128 which is least affected by foreground contamination we used the recent results of Quillen et al. (2006), who modeled the observed mid-infrared geometrical morphology by integrating the light from an emitting, thin, and warped disk, similar to that inferred from previous kinematic studies of NGC5128. According to Quillen et al. (2006) the northern part of the galaxy lays closer to the observer. Taking this fact into account, we restricted our search area to the mentioned region and the clouds from this region only were used in our analysis (see Figure 2.6).

2.6 Cloud properties

The clouds were extracted from the wavelet-reconstructed $J-K$ color map using a 2D-version of the *clumpfind* (Williams et al. 1994) - an automatic routine for analyzing the clumpy structure. The algorithm works by first contouring the data at a multiple of the rms noise of the observations, then searches for local maxima in the data which locate the clumps, and then follows them down to lower intensities. The shape of the clumps identified is arbitrary and the clumps themselves are considered as the basic building blocks of the cloud showing normally no substructure. The clouds were defined as regions containing more than 25 pixels ($7.3''$), each with a value greater than 5 σ_{rms}.

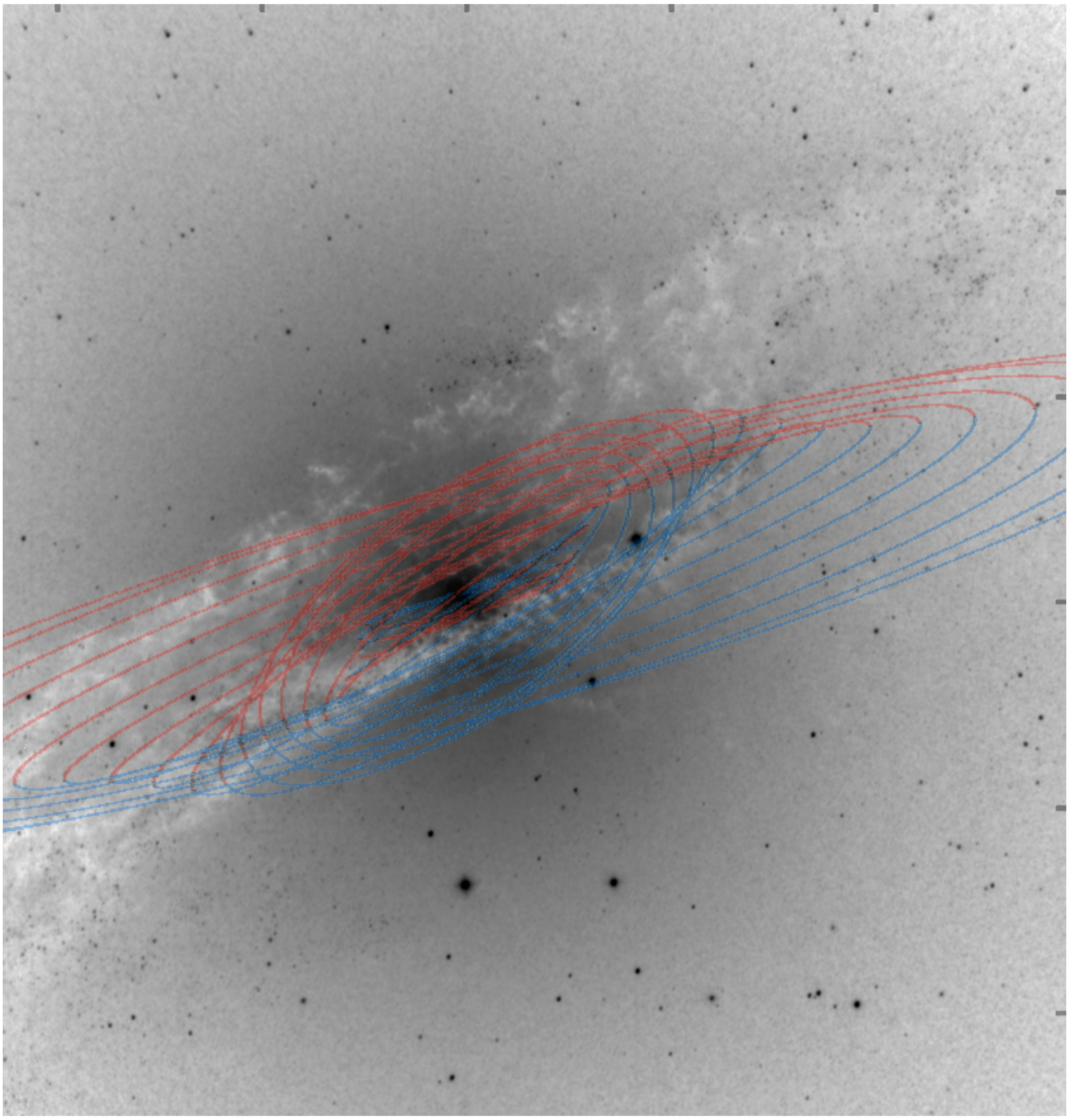

Figure 2.6: Inverted J-band image of NGC5128. Rings for the warped disk model are displayed according to Quillen et al. (2006). The semicircle of each ring nearest the observer is shown in red, and the more distant semicircle is shown in blue. At near-infrared and visible wavelengths, dust nearer the observer absorbs more background galactic starlight than does dust more distant from the observer.

2.6.1 Masses and sizes of the molecular clouds

We assume that $N(H_2)$ can be traced by the dust column density. Measurements of the near-infrared color excesses of stars (Lada et al. 1994) can provide estimates of column density along the selected line of sight toward a star located within a molecular cloud. Information on the optical depth of the cloud can be derived from the difference between the observed and the intrinsic color of a background star. Assuming a normal reddening law (Rieke & Lebofsky 1985) the following expression is valid (in case of $H - K$ color):

$$(H - K)_{\text{observed}} = (H - K)_{\text{intrinsic}} + 0.063 * A_V \tag{2.1}$$

where $(H - K)_{observed}$ and $(H - K)_{intrinsic}$ denote observed and intrinsic quantities, respectively. The quantity of A_V is s directly related to the projected mass density of the cloud (Lilley 1955; Bohlin et al. 1978). It has been also demonstrated (Bohlin et al. 1978) that most clouds have the same gas-to-dust ratio. Hence $N(H_2) = A_V \cdot 1.9 \times 10^{21}$ protons $\text{cm}^{-2} mag^{-1}$ The correspondent projected density: $\kappa = A_V \cdot 15 M_\odot \text{ pc}^{-2}$

However in other galaxies the individual stars cannot be fully resolved. Therefore instead of measuring the colors of background stars to molecular clouds, we measure the *average* color of the unresolved stars that will fall on a pixel of a NIR detector. We measure the NIR diffuse galaxy light seen through GMCs, in a simple analogy to our Galactic work. The uncertainty in the color excess is estimated by using the variance of the color in the dust-free region. By comparing to a dust-free region we avoid having to know the unreddened colors of the underlying stellar population and do not require the observations to have been made in photometric conditions.

The size of a clump is defined as the effective circular radius:

$$\Delta R = \sqrt{A/\pi},$$

where A is the projected area of the clump on the sky.

In total we detected 436 clumps over the whole field of view. After constraining the sample giving the geometrical parameters (see previous section) we end up with 172 clumps, which were used in further analysis (see Fig. 2.7). Derived parameters of the clouds are summarized in the Table A.1.

2.6.2 GMC Mass Spectrum

The mass distribution of a population of molecular clouds is often represented in differential form, i.e. the number of clouds that would be found in a range of masses. In terms of mass bins, this can expressed as

$$\frac{dN}{dM} = f(M). \tag{2.2}$$

Integration of this expression will give us the *cumulative* mass distribution:

$$N(M' > M) = \int_{M_{max}}^{M'} f(M)dM = g(M), \tag{2.3}$$

which represents the number of clouds with masses greater than some reference mass as a function of that reference mass. For molecular clouds, both forms of the mass spectrum follow power-laws: $f(M) \propto M^{\alpha}$ and $g(M) \propto M^{\alpha+1}$ with $\alpha < -1$ in all known cases.

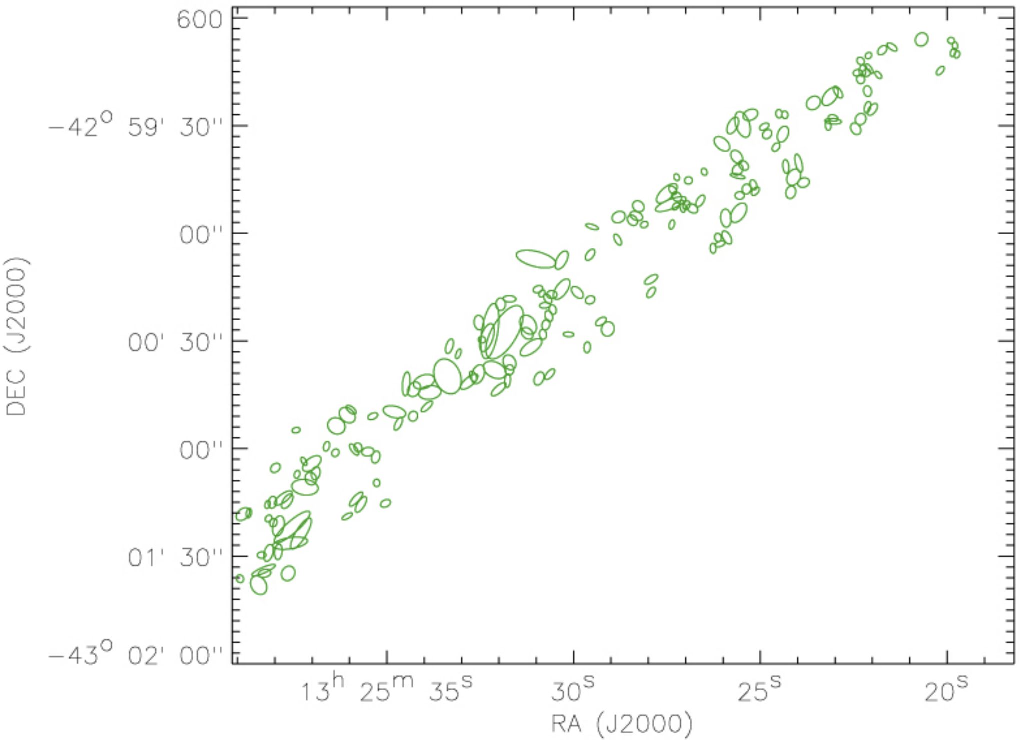

FIGURE 2.7: Spatial location of the detected clumps. The apparent size of a clump is proportional to its mass.

However it often happens that some mass distributions lack clouds above certain maximum mass M_0. In order to account that into account, a truncated power-law distribution (as suggested by Williams & McKee (1997)) was adopted. The final form of the cumulative distribution is:

$$N(M' > M) = N_0 \left[\left(\frac{M}{M_0} \right)^{\alpha+1} - 1 \right], \tag{2.4}$$

where M_0 is the maximum mass in the distribution. N_0 is the number of clouds which are more massive than $2^{1/(\alpha+1)} M_0$. This is the point where the distribution shows a significant deviation from a power law. If $N_0 \sim 1$, there is no such deviation. For this form of the cumulative mass distribution,

$$\frac{dN}{dM} = (\alpha + 1) \frac{N_0}{M_0} \left(\frac{M}{M_0} \right)^{\alpha}, \ M < M_0. \tag{2.5}$$

Histogram of the mass distribution of GMC from our sample is presented in Figure 2.8 (in log-log scale). A power law was fitted to the mass bins where the sample is complete (M > $10^{4.5}$ $M_\odot$). The observed mass distribution is well fit with the power index $\alpha = -2.31 \pm 0.14$. A bootstrapping technique was used to estimate the errors of the fit.

In case when a sample is relatively small, one of the most important problems is to properly assess errors for the data fit. Uncertainties appear in both the mass of the cloud and in the variance of a random sample being drawn from an infinite parent distribution (Rosolowsky 2005). The mass coordinate will have an uncertainty from the measurement error. The cumulative number will have an uncertainty characterized by a counting error. In order to properly estimate parameters of the fit, that has uncertainties in both coordinates, we also used the $error - in - variable$ method (Rosolowsky 2005, and references therein). The best produced fit yields $\alpha = -2.37 \pm 0.18$, which is in very good agreement with our previous result.

We see that the number of clumps gradually increases with decreasing mass until a turnover point at approximately logM = 4.5. Beyond the turnover, the number of clumps decreases again. We think that this turnover point does not indicate the Jeans mass or the minimum detectable mass and therefore does not represent a characteristic mass but results from undersampling the clumps with the lowest masses. Therefore, the data points to the left of the turnover mass are not included in a least square fit to determine α. Errors were assumed to follow Poisson statistics.

A large number of studies of molecular clouds have examined the relationship between a cloud's mass M and size R. For the mass - size relationship of the clumps, we included all clumps with masses above the minimum detectable mass and indicated the turnover mass with a dashed line. A least-squares fit of the data points yields a slope of (-2.34 +/- 0.02). See Figure 2.9.

2.7 Completeness

Completeness of such a survey is of crucial importance in the study of the mass function. The main factor affecting the completeness of the data is quite complex structure of molecular clouds which leads to crowdness. To estimate the completeness properly, we added a regular grid of artificial sources to the $J - K$ color map and computed the fraction of them recovered by *clumpfind* search algorithm. Each test source was a $6''$ $\times$ $6''$Gaussian with a constant brightness profile for all test sources regardless the flux density(mass) of the test source. All the artificial sources were spaced by $8''$in right ascension and declination. In such a way 690 sources were added to the object frame. Then we performed recovery test with masses ranging from $1.5 \times 10^4 M_\odot$ to $10^6 M_\odot$.

Figure 2.10 shows the fraction of the test sources as a function of a cloud mass. The completeness of our survey at $10^5 M_\odot$ is about 90%. In all our further experiments we never were able to achieve 100% completeness level. From our point point of view this can be explained by complexity and crowdness of the molecular clouds which usually have irregular structures.

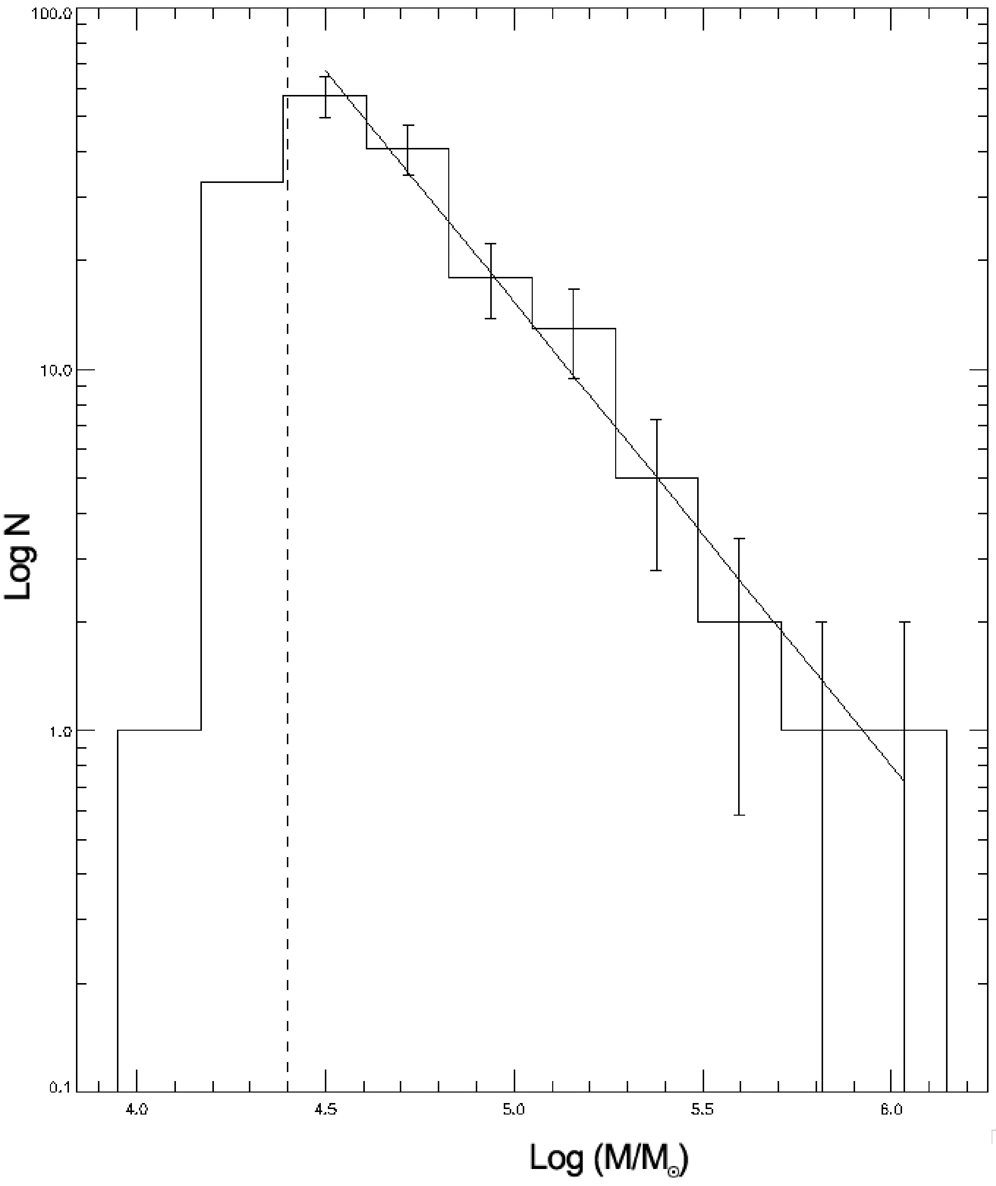

FIGURE 2.8: The mass spectrum for giant molecular clouds in NGC 5128. A power law fits the mass bin for which the catalog is complete The observed mass distribution is well fit with the power index $\alpha = -2.31 \pm 0.14$.

2.8 Discussion

For the first time we derived a mass spectrum for GMCs in NGC5128, in a way which does not rely on CO observations. The obtained power index $\alpha = -2.31$ corresponds to a quite steep slope, indicating that a large number of low mass clumps were found.

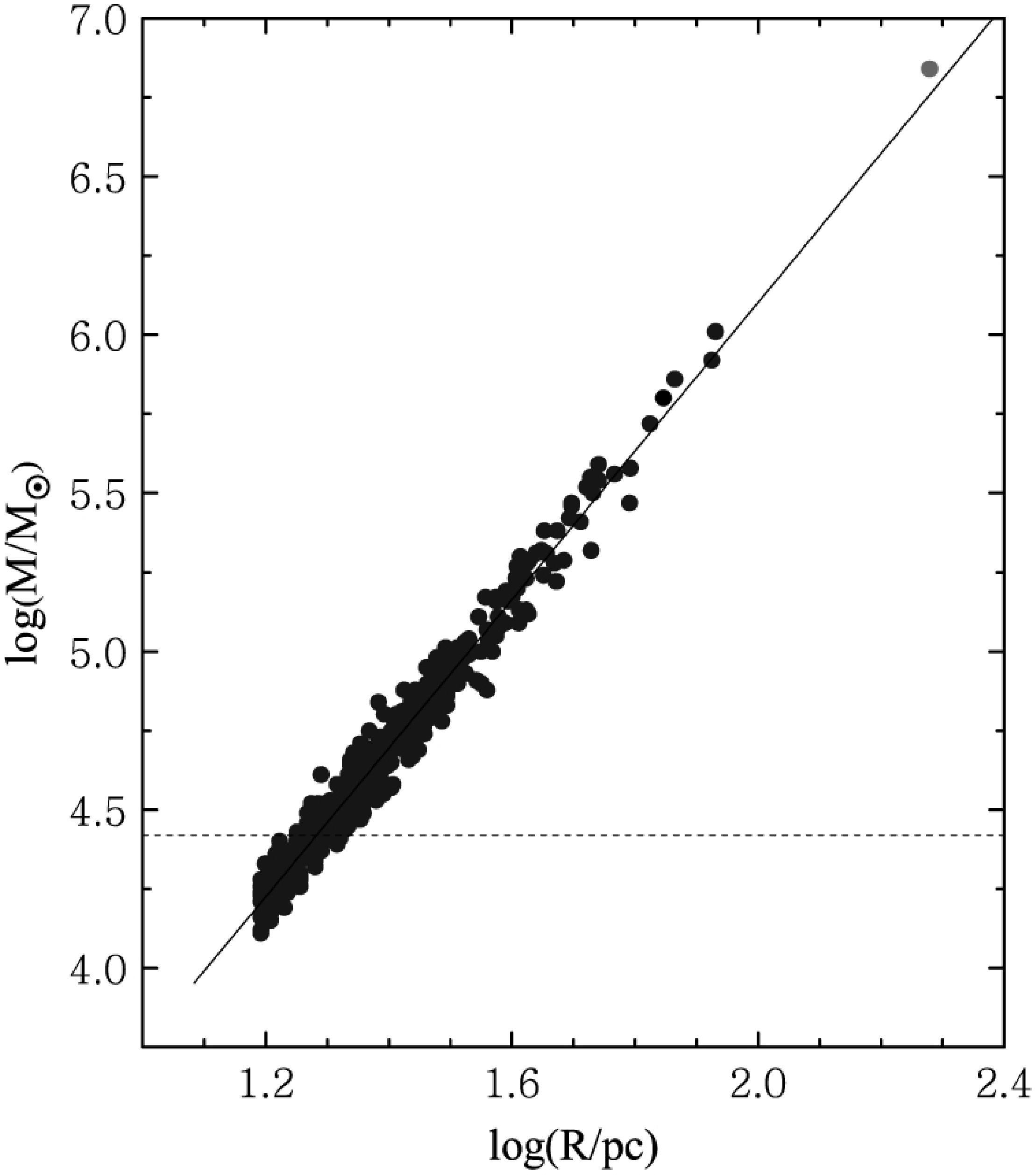

Figure 2.9: Plot of mass as a function of the radius for all detected clumps.

The value of -2.31 is in good agreement with the results for M33 (α = -2.6, Engargiola et al. 2003), and significantly larger than those ones for the Milky Way (-1.4 .. -1.9, Solomon et al. 1987; Elmegreen & Falgarone 1996; Kramer et al. 1998). It might be that the clump mass spectral index is systematically higher when determined from large to very large fields, which is probably related to the higher dynamic range of the observations (larger area, higher spatial resolution).

We can argue that overlapping on the line-of-sight clouds in NGC5128 can have

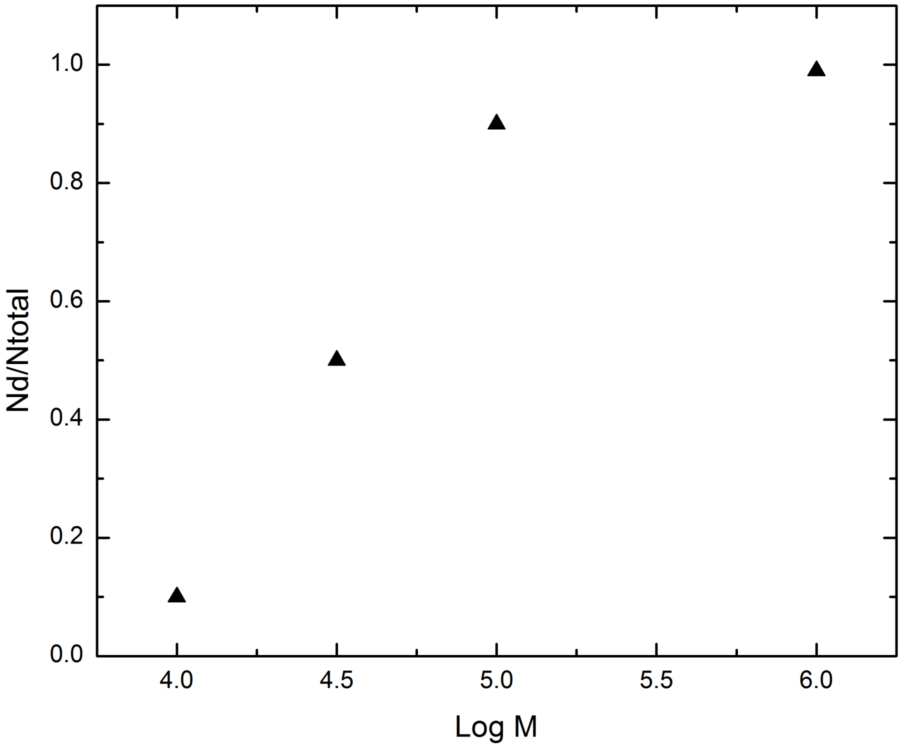

Figure 2.10: Fraction of artificial clouds recovered as a function of a cloud mass. $Y\!-\!axis$: Nd - number of detected clouds, Ntotal - total number of clouds.

some impact on the the mass spectrum slope, however in that case this would increase the number of more massive clouds and therefore lead to a "flatter" spectrum, where α is lower. Our result is closer to the one obtained by Engargiola et al. (2003) for M33 (α = -2.6). Perhaps this is due to physical and intrinsic difference between GMCs in those galaxies. On the other hand, we are much more sensitive to column density, than typical CO-observations. Also, we have an advantage in resolution.

Milky Way has the shallowest GMC mass distribution among reviewed galaxies. However, it is still not clear whether this is a real effect or there some observational biases are present. Observing from inside the Galaxy, one can get several small, i.e. less massive, clouds in the line-of-site and as a result the GMC mass spectrum index will be lowered. The second problem is the distances. Any errors in distance determination can change the GMC mass distribution, "shuffling" masses of the clouds within a sample. According to Rosolowsky (2005) such bias can increase the index of the mass distribution by 0.2 to 20%. Therefore the "real" index of the mass distribution for the Milky Way could be steeper than the present "canonical" value.

Presented study would be incomplete without assessment of reliability the method. How reliable is the dust as a tracer of molecular hydrogen in external galaxies ? For the

Galactic molecular clouds dust is proven to be a relatively good tracer (Lombardi & Alves 2001). It's biggest advantage is dynamic range. Using near infrared observations Alves et al. (2001) successfully mapped B68 Bok globule covering the range of extinction of $\sim$ 27 mag, while CO-observations of the same object have been able to reach $\sim$10 mag only. However, it's still extremely difficult to take into account variations in size and compositional distributions of dust grains which eventually affect the reddening law. Another problem of the method (and this is where CO-observations have an advantage) is inability of kinematically separate molecular clouds located along the line of sight.

In external galaxies variations in relative geometry and inhomogeneity of dust distribution will produce significant scatter and saturation of colors. Recent radiative-transfer simulations for the case of face-on geometry (Kainulainen et al. 2008) show that using near-infrared color excess values makes quite hard to directly relate "true" and observed mass functions of extragalactic molecular clouds. However, it should be noted that in face-on geometry case the most significant and important factor is the fraction of foreground flux. It is unknown. In other systems, where the positions of molecular clouds can be much better constrained with respect to the main illumination source, we can definitely get better estimates of the true mass of the clouds.

2.9 Conclusions

We have shown that using a set high-resolution near-infrared color maps of NGC5128 it is possible to quantitatively analyze clumpy structure of the dust in the galaxy. The masses of the molecular clouds were derived using a modified 2D-version of the $clumpfind$ (Williams et al. 1994) automatic routine.

We constructed a sample of molecular clouds based on the observed by SPITZER mid-infrared geometrical morphology (Quillen et al. 2006) in order to minimize effects of the light scattering and foreground screen geometry.

The mass distribution of molecular clouds in the northern part of the Centaurus A has a measured index -2.31 ± 0.14 which is higher than that found in the inner Milky Way (α = -1.5), but it is in good agreement with the results for M33 (α = -2.6).

Despite some concerns (geometry dependent results, scattering problem) we believe that use of dust as a tracer of molecular hydrogen in other galaxies is a promising approach, which allows to probe GMCs at large distances and provides new insights to the physics and morphology of the dense ISM in other galaxies.

3

The inner structure of the merger galaxy NGC 1316 (Fornax A): a decoupled boxy core ?

submitted to Astronomy & Astrophysics

Beletsky, Y., Moiseev, A., Alves, J., and Kniazev,A.

Abstract

Fornax A (NGC1316) is a giant elliptical radio galaxy with prominent dust lanes. It has been considered as a merger remnant with possibly more than one merger event. Our aim is to study central area of the galaxy using near-infrared imaging as well as optical spectroscopy around the Calcium triplet region (Ca II $\lambda\lambda$8498,8542,8662 Å).

The imaging data (J, H, and Ks bands) have been obtained with SOFI, the infrared imager-spectrograph at ESO/NTT telescope. Spectroscopic observations have been conducted at the Siding Spring 2.3 m telescope. We analyzed previously published kinematics and complemented them with our spectroscopic observations obtained along the major axis of the galaxy. In order to reveal the inner structure of the galaxy the images were fitted with a one-component model containing Sérsic function.

As a result of 2D-decomposition analysis of the images we have detected a nearly exponentially distributed central brightness excess (up to 16% of the total flux in Ks) with respect to an oblate Sersic's spheroid. A "peanut-shape" disk-like structure is visible on the residuals in all observed bands, becoming most prominent in K-band. It has estimated diameter of 0.76 kpc ($\sim 8''$) and projected minor axis of about 430 pc. The analysis of previously published and our new kinematical data shows that discovered brightness excess might be explained by presence of a kinematically decoupled core in the inner $4''$ region of Fornax A.

3.1 Introduction

NGC 1316 (Fornax A) is a giant elliptical radio galaxy with pronounced dust patches, Hα filaments, ripples, and loops (Schweizer 1980, 1981) located in the outskirts of Fornax cluster, $3^{\circ}\!.7$ away from the central giant elliptical NGC 1399. From its high luminosity and low central velocity dispersion compared to that expected from the Faber-Jackson relation (D'Onofrio et al. 1995) NGC 1316 has been considered as a merger remnant (Bosma et al. 1985) with tidal-tail system comprising five tails or loops of varying morphology, which argues for more than one merger event. Indeed, one seemed to have occurred about 3 Gyr ago (Goudfrooij et al. 2001), while evidence for two more recent mergers have also been found (Schweizer 1980; Mackie & Fabbiano 1998). Cataloged as a S0 peculiar galaxy it has been extensively observed in a wide range of wavelengths. In the radio domain Fornax A is one of the brightest objects in the sky (Ekers et al. 1983). It has prominent giant radio lobes at a position angle of $\sim$110° (Wade 1961) consisting of polarized filaments (Fomalont et al. 1989) and S-shaped nuclear radio jets (Geldzahler & Fomalont 1984). Stellar kinematics of NGC 1316 shows that the galaxy is rotating around the minor axis at a position angle of $\sim$ 140° (Bosma et al. 1985; Arnaboldi et al. 1998). The kinematics of the outer halo of NGC 1316 indicates that this early-type galaxy contains as much angular momentum as a giant spiral of similar luminosity (Arnaboldi et al. 1998). From the study of inner dust distribution and outer complex of shells and loops (Schweizer 1980) it was pointed out the similarity between NGC 1316 and NGC 5128 (Centaurus A), also an early-type giant radio galaxy with double radio lobes powered by a central engine. The surface brightness decomposition of NGC 1316 has been performed in the past. The excess of brightness in the central region (deviations from $r^{1/4}$ law) has been noted in the earliest studies (Schweizer 1980). D'Onofrio (2001) found a nuclear disk from ground-based B-band observations, while de Souza et al. (2004), also using ground-based optical data, obtained different parameters for this disk.

In this paper we reconsider those conclusions. Using ground-based near-infrared images and kinematics we show that discovered brightness excess in central region (within 4 arcsec) of the galaxy might be explained by presence of a kinematically decoupled core.

For the remainder of this paper, we adopt a distance D = 18.6 Mpc based on HST measurements of Cepheid variables (Madore et al. 1999) in NGC 1365, so that $1''$ corresponds to 90 pc.

3.2 Observations and data reduction

3.2.1 Photometry

The photometric observations were made on the 7th and 8th of March 2001 using the near-IR imager/spectrometer SOFI (J, H, and Ks bands) on the 3.5 m NTT telescope in La Silla, Chile. The SOFI detector is a Hawaii HgCdTe 1024×1024 array. We used the SOFI large-field mode, with a pixel scale $0.29''$per pixel and a field of view $4.9'$. Conditions during the observations were generally clear with a typical seeing better than 0.7 arcsec. The integration times were 20×6 s for each band. The observations were carried out using the "jitter" technique. Jittering was controlled by the automatic jitter template, which produce a set of dithered frames. Offsets are generated randomly within a box of 40×40 arsec centered on the galaxy center. Since the full size of the galaxy observed is bigger than the field of view of SOFI we obtained intermediate sky frames of the same exposure time. A classical near-infrared data reduction procedure was adopted. Dark frame subtraction, flat fielding and illumination correction were applied using the CCDRED package in IRAF[1]. The final sky-subtracted images were aligned and combined using JITTER routine of the ESO's ECLIPSE package (version 4.9.0, Devillard 1997b). The zero-points were checked by comparing the photometry of stars with measurements from the 2MASS[2].

We also obtained archival images of NGC1316 observed with the ACS Wide Field Camera (WFC) in F435W, F555W and F814W filters (GO program 9409, PI: Goudfrooij) from the HST public archive database. Ground-based optical images in the bands B,V and R, which have larger field of view and better magnitude limits comparing with HST data, have been obtained by Cheng et al. (1997).

Figure 3.1 shows the examples of images in optical and NIR domain. While at the longest wavelengths the intrinsic boxy shape of the isophotes becomes more evident, the large amount of dust present in the galaxy heavily distorts the overall picture.

---

[1] *Image Reduction and Analysis Facility* (IRAF) is distributed by NOAO, which is operated by AURA, Inc., under contract to the NSF.

[2] This publication makes use of data products from the Two Micron All Sky Survey, which is a joint project of the University of Massachusetts and the Infrared Processing and Analysis Center/California Institute of Technology, funded by the National Aeronautics and Space Administration and the National Science Foundation.

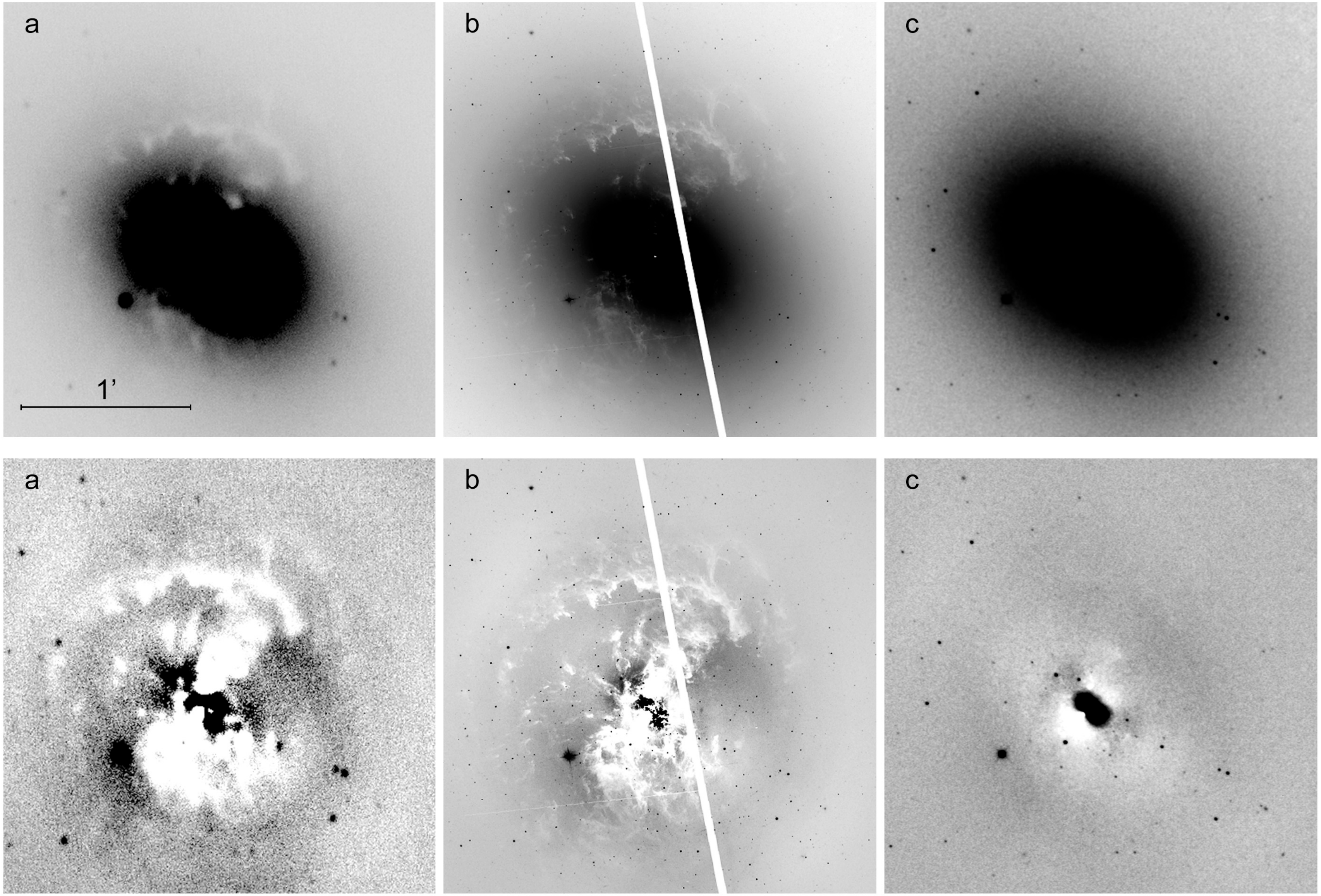

Figure 3.1: *Top*: The original images of NGC 1316 in B,V, and *Ks* bands. (*a*) B-band (CTIO, 0.9m), (*b*) HST/ASC *V(F555W)*, (*c*) NTT/SOFI *Ks* image. North is up, and east is to the left. *Bottom*: Residuals after 2D-decomposition of NGC 1316 in the B,V, and *Ks* bands respectively. The positive and negative residuals are shown in black and white respectively.

3.2.2 Spectroscopy

The spectroscopic observations were performed by R.Saglia in October 2001 at the Siding Spring 2.3m telescope, using the red arm of the Double Beam Spectrograph (Rodgers et al. 1988) in longslit (6.7 arcmin, at PA=58°), no beam splitter, slit width of 4 arcsec and the Site 1752 × 532 15-μm pixels CCD. The wavelength range was $\lambda = 8090 - 9010$Å. The integration time was 60 minutes. Template stars were also observed, trailed along the slit. The data reduction followed Saglia et al. (2002) with the usual steps: after bias subtraction and flat-fielding with dome flats, cosmic rays were eliminated using median filtering. The wavelength calibration achieved 0.1 Å rms precision. After rebinning on a natural logarithmic wavelength scale, the sky measured at the ends of the slit was subtracted. The systematic residuals after sky subtraction, estimated from the blank sky frames, were less than 1%. The galaxy spectrum was rebinned along the spatial direction to obtain nearly constant signal-to-noise ratio with radius. The kinematics were determined with the Fourier Correlation Quotient method, as in Bender, Saglia and Gerhard (Bender et al. 1994). The relative errors were computed from Monte Carlo simulations, following Mehlert et al. (2000).

3.3 2D image decomposition

In this section we investigate to which extend image fitting can be used to probe the central structures of early-type galaxies.

We performed two-dimensional modeling of the images using GALFIT (v. 2.0.3, Peng et al. 2002). The images were fitted with a one-component model containing Sérsic function (Sersic 1968). Since the galaxy has extensive dust patches and lanes, those features as well as the stars were carefully masked from the fits. The axis ratio parameter q is constant as a function of radius for each model produced by GALFIT. However, analyzing the NIR images of the galaxy we noted an increase of the axis ratio of the elliptical isophotes with radius. The formal χ^2-fitting (with q as a free parameter) leads to an underestimation of the model brightness in outer regions. In order to solve this problem, the axis ratio parameter was fixed and a set of models ($q = 0.65..0.75$) was calculated. Finally we chose the model with the best even distribution of the residual brightness in the outer regions.

Figure 3.1 shows the original images both optical and infrared as well as the results of 2D-decomposition. As discussed in Sect. 3.2.1, the slightly "peanut-shape" distorted residuals are due to the dust. However, a disk-like structure is visible in all bands. While the structure is highly patchy in the optical, in the NIR we clearly see a well resolved disk. Moreover, the residual brightness distribution along the major and minor axes is not too far from an exponential, as Figure 3.2 shows for the B, V, R, J, H and K bands. Figure 3.2 displays the cuts through residual brightness along the minor and major axes of the disk as well as results of the fitting by an exponential disk model. The parameters of the decompositions (μ_0 – central surface brightness; h_{ma} and h_{mi} – disk scales along major and minor axes; L_{10} – a ratio of exponential disc luminosity to the total galactic luminosity on $r < 10''$) are shown in Table 3.1. We note that the

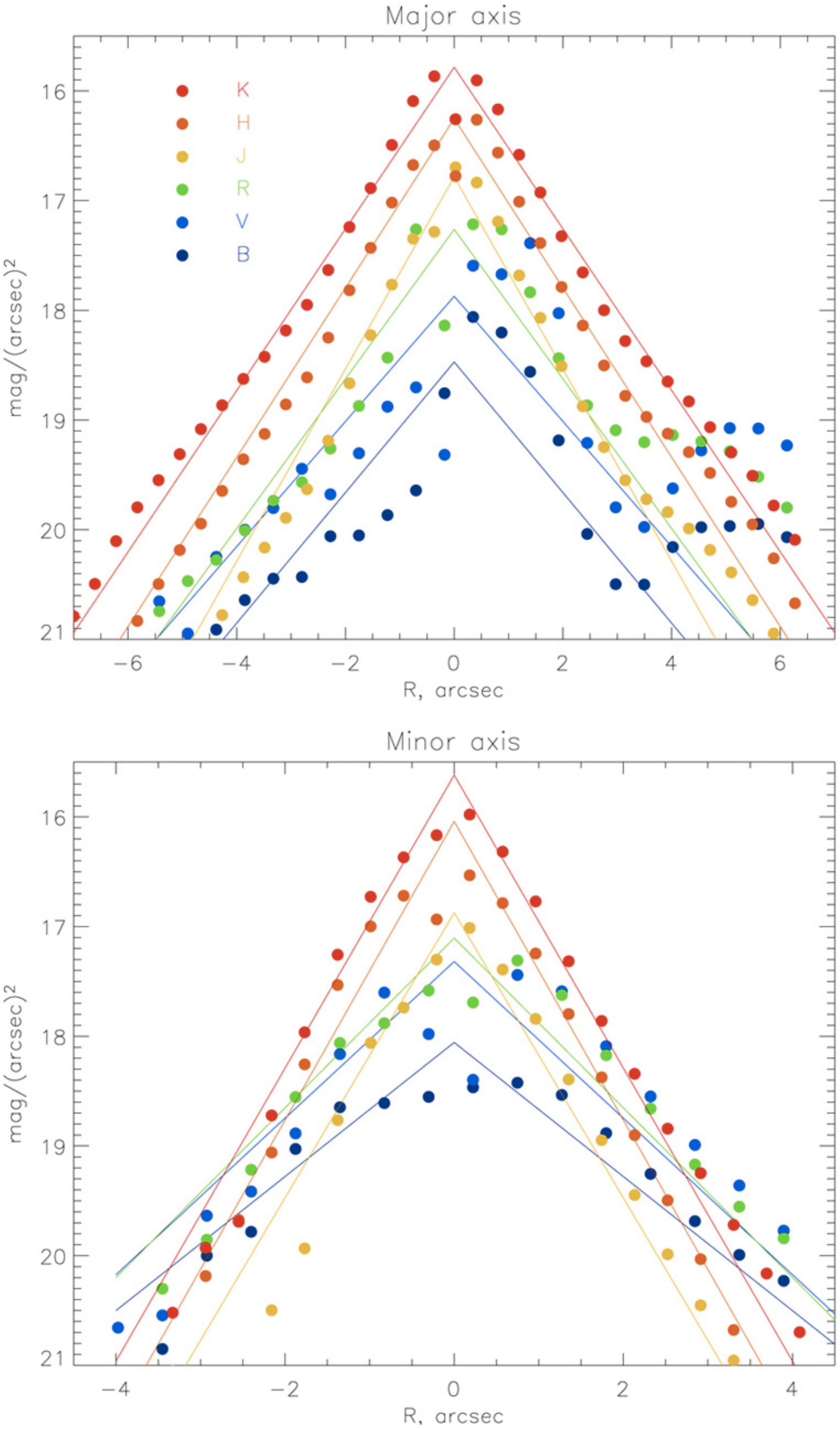

FIGURE 3.2: Cuts through residual brightness distributions along their major (top) and minor (bottom) axes. The lines show the fitting by the exponential disk approach.

TABLE 3.1: The inner 'disk' properties

Band	μ_0 $^m/\square''$	h_{ma} $''$	h_{mi} $''$	L_{10}
B	18.47 ± 0.22	1.83 ± 0.26	1.78 ± 0.19	0.072
V	17.87 ± 0.30	1.90 ± 0.37	1.52 ± 0.23	0.059
R	17.26 ± 0.19	1.59 ± 0.16	1.40 ± 0.14	0.067
J	16.78 ± 0.12	1.24 ± 0.06	0.84 ± 0.07	0.110
H	16.25 ± 0.09	1.41 ± 0.06	0.80 ± 0.04	0.117
K	15.78 ± 0.07	1.47 ± 0.05	0.81 ± 0.04	0.159

decomposition in the optical is not as certain as it is in the NIR. On the other hand, the brightness contribution from this structure to the total flux, which presumably can be an edge-on disk, is quite small (up to 16% in Ks). Nevertheless, this contribution increases in NIR. This is mainly due to both lower dust extinction at these wavelengths and in part to the fact that there is a gradient in the stellar population color towards the nucleus of this galaxy (where it is reddest).

We note that the parameters of this disk-like structure are in agreement with the $\mu_0 - h$ relation for galactic disks (van den Bosch 1998; Reshetnikov 2000) as well as for S0 and disky ellipticals (Scorza & Bender 1995). Given estimated diameter of the disk (up to 3 radial scales) of 0.76 kpc, and a projected minor axis of about 430 pc, the discovered structure looks like a compact disk in the nucleus of NGC 1316. In order to reveal physical nature of this structure we performed a kinematical study of the central region of NGC1316.

3.4 Kinematics

Here we consider kinematics of the stellar component only, because both ionized and molecular gas kinematics are significantly disturbed by the recent merging process and possibly affected by the radio-jet (Schweizer 1980; Horellou et al. 2001). In contrast with gas contribution, collision-less motions of stars should be connected with the distinct photometric structure founded in previous Section. This is due to the fact that stars are mostly responsible for observed brightness excess.

Recent long-slit kinematics of NGC 1316 is available from Arnaboldi et al. (1998) along the major (PA=50°) and minor (PA=140°) axis. The kinematics along the major axis (PA=45°) has been obtained by Longhetti et al. (1998). Also Bedregal et al. (2006) presents high quality kinematic data along the major axis of NGC1316 obtained with VLT/FORS2. All these data sets contain observations at Mgb region, ($\lambda \approx 5212$ Å) which allows to derive mean stellar velocities and velocity dispersion profiles. See Figure 3.3.

We complement these data with observations at PA=58° around the CaT region. Figure 3.4 shows the derived kinematics, based on the observations performed by R.Saglia (see Sect. 3.2.2). In the inner 5 arcsec there is no rotation and H_4 is slightly positive. Despite the reduced spatial resolution due to astigmatism, we believe that

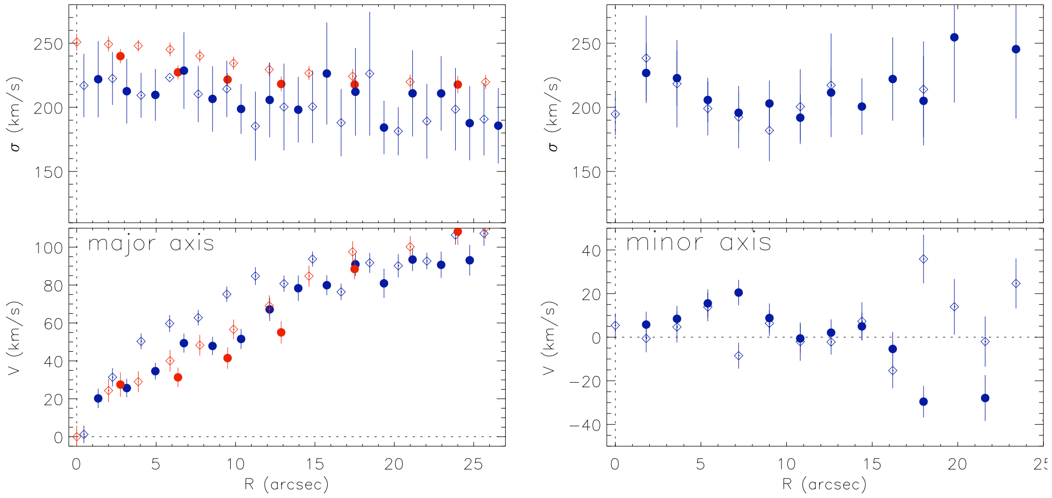

FIGURE 3.3: The stellar velocity and velocity dispersions data along major and minor galactic axes. Blue points - are data from Arnaboldi et al. (1998), red points - from Bedregal et al. (2006). The profiles are folded with respect to the photometric center. Filled and open symbols crosses show the two sides of the galaxy. The velocity profiles are zeroed to the systemic velocity and antisymmetrized.

the absence of rotation is real, since none of the other 17 ellipticals observed during the run show such a feature.

Figures 3.3 and 3.4 show that the inner region of NGC1316 most probably harbors a kinematically decoupled core. Along the minor axis the (small) detected rotation changes sign at $r \approx 10$ arcsec. Along the major axis, depending on the exact value of the PA (and possibly the centering of the slits), rotation is detected (at PA=50°) or is absent inside the inner 5 arsec (at PA=58°), or is asymmetric at PA=45° (Longhetti et al. 1998). The velocity dispersion profiles offer a hint to a dynamically colder component near the center.

It is important to note, that both Mgb and Calcium triplet (CaT hereafter; Ca II $\lambda\lambda$8498, 8542, 8662 Å) data exhibit almost the same maximal values and radial behaviors of the velocity dispersion. However, circumnuclear line-of-sight velocity profiles along the major axis are different between those spectral domains: Mgb data shows significant rotation whereas in CaT there is a deficiency of rotation within $r < 5''$.

Apparently a dynamically cold inner component is becoming more prominent in R- and NIR-bands where the dust extinction is lower than in Mgb (an extinction optical depth effect; see e.g., McKeith et al. (1993), Brosch et al. (2007) and references therein). Perhaps this component is the counter-rotating one having line-of-sight velocities superimposed with the stellar rotation. As a result we observe such a small gradient of line-of-sight velocities. This is consistent with the results of recent 2D-velocity fields observations of NGC1316 obtained with VLT/SINFONI (Nowak et al. 2008). In particular, the latter authors did not find clearly visible rotation in the central $\sim 3''$.

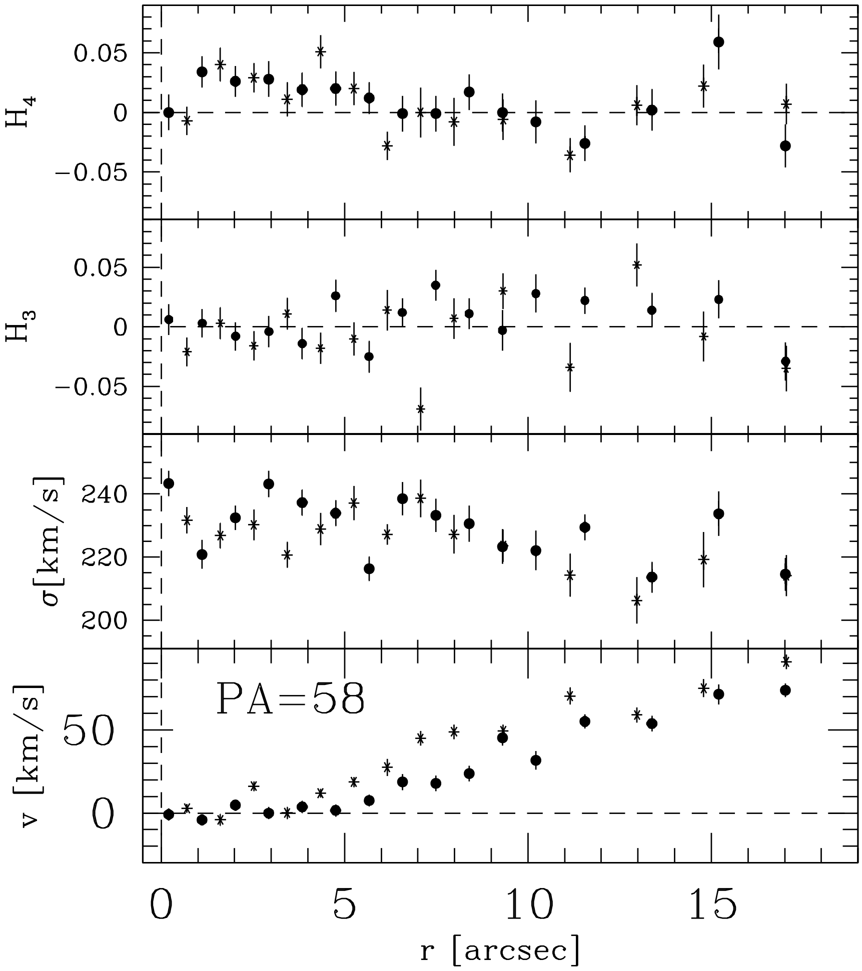

FIGURE 3.4: The stellar kinematics derived from the Calcium triplet spectrum at PA=58°. From top to bottom the H_4 and H_3 coefficients, the velocity dispersion and mean velocity profiles. The profiles are folded with respect to the photometric center. Filled circles and crosses show the two sides of the galaxy. The velocity profiles are zeroed to the median velocity and antisymmetrized (as H_3).

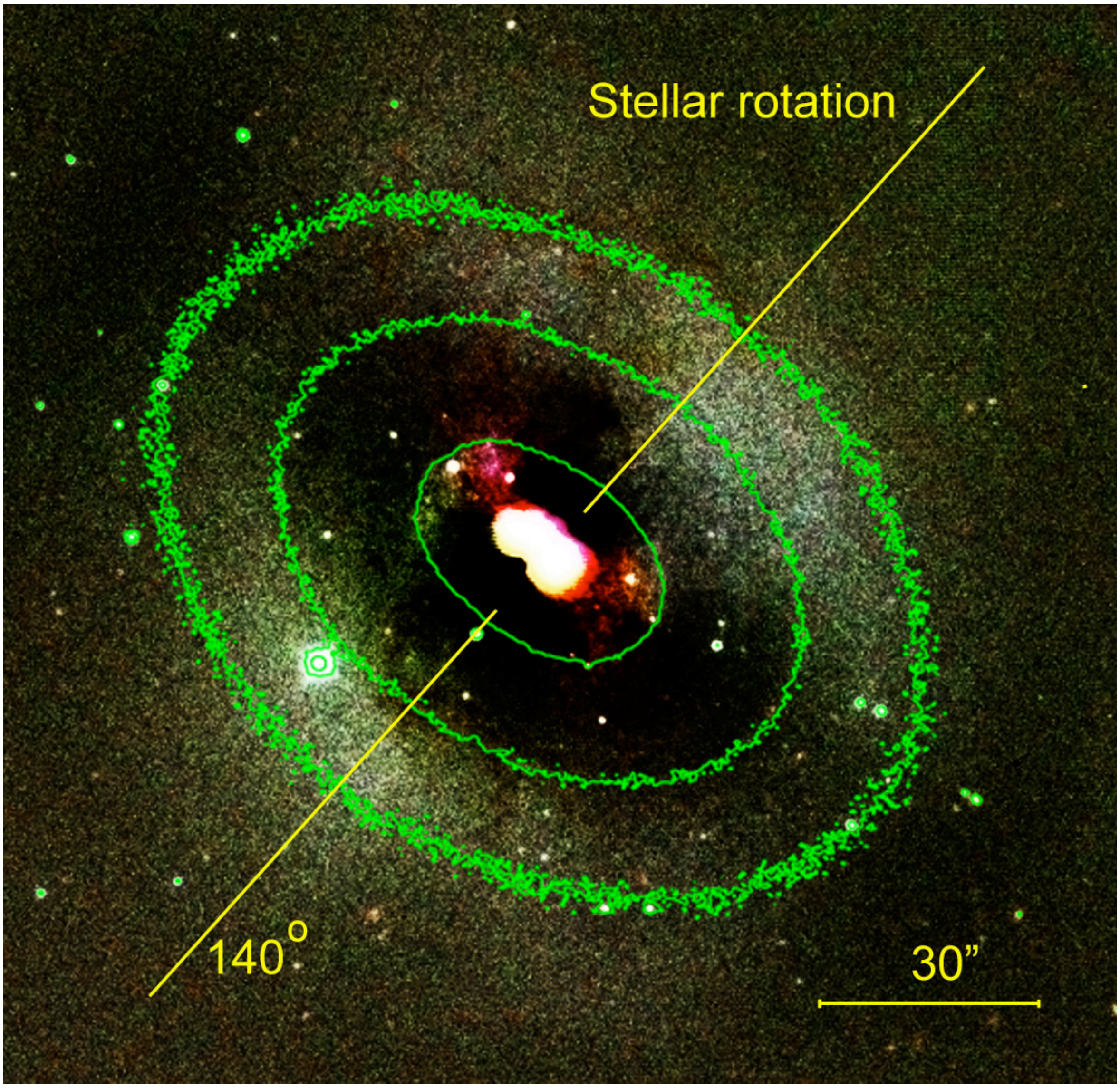

FIGURE 3.5: $J(blue)$, $H(green)$, and $Ks(red)$ color composite of NGC 1316 constructed from model subtracted frames in each filter. North is up, east is to the left. The line shows the axis of stellar rotation (Madore et al. (1999)). The green contours represent Ks-band isophotes.

3.5 Discussion

Complexity of the central regions of early-type galaxies is a well-known problem (Rest et al. 2001; Erwin & Sparke 2003). Moreover, presence of dust in the vicinity of central regions of these galaxies (NGC1316 is one of the best examples) makes a study of those regions even more complicated. We present new photometric and spectroscopic observations of the merger remnant NGC 1316.

The photometric structure of the galaxy posses central excess of brightness with boxy isophotes (Figure 3.6) and near exponential radial profile of brightness with characteristic radial scale $h_{ma} = 110 - 170$ pc. The stellar kinematics along the major axis suggests presence of a kinematically decoupled core on the same spatial scale. What is the origin of this decoupling? We propose three possible explanations of the complex morphological structure:

1. The inner boxy structure is not a rotationally supported disk. In this case the stellar velocity dispersion supports oblate shape of the structure. However, the difference between radial and vertical components of the velocity dispersion seems to be unusually large, because ellipticity of the residual brightness structures is also large.

2. Another possible explanation comes from the analysis of the disk isophotes in the near infrared. Their structure resembles a boxy-peanut bulge in edge-on galaxies. Usually those structures are associated with the presence of an edge-on bar. The recent study of stellar kinematics in boxy-peanut bulges (Chung & Bureau 2004) shows that 80% of structures in their sample are bars in fact. On other hand, there are several arguments against this explanation. Firstly, brightness distribution along the major axis is not flat and follows an exponential law (see Figure 3.2) which implies existence of a disk, not a bar. Secondly, bar is a result of a disk instability. Thus we should observe both disk and a bar. However, we do not see any signs of a disk associated with the "bar". It is a problem of bar formation (instability) in dominated spherical potential, however, numerical simulations by Di Matteo et al. (2007) show a bar formation in a gaseous disk in elliptical galaxy after merging with a spiral one.

3. This could also be a nuclear disk which has formed via recent merging event. In sect. 3.3 we outline several arguments in support of this idea based on photometric properties: exponential law of brightness distribution, $\mu_0 - h$ relation. Despite presence of a central peak in the radial distribution velocity (Figure 3.3), D'Onofrio et al. (1995) noted that central velocity dispersion is somewhat lower than the one expected for a galaxy of this luminosity from Faber-Jackson relation (260 versus 400 km/s). It could be possibly explained by presence of a dynamically cold disk-like component. However, why don't we see a significant rotation of this circumnuclear disk, but only a small-amplitude rotation in Mgb and absence of the rotation in CaT and NIR (see Sect. 3.4) ? Possibly this is due to a disk counter-rotation relatively to the main stellar spheroid. Counter-rotation phenomena is well known in lenticular and elliptical galaxies (for instance, see Davies et al. 2001). Recently, Di Matteo et al. (2007) presented a scenario of formation of counter-rotation central component in elliptical galaxies by dissipative and dissipation-less mergers of a prototype elliptical with spiral systems in retrograde orbits. In this case in the optical band (Mgb) we mostly see slow rotation of spherical component of the galaxy, however in CaT and NIR domain we can see both components along the line-of-sight: spheroid and disk. The disk is hidden and appears mostly in NIR domain, because of the dust extinction and/or specific stellar population – see Silva et al. (2007): nucleus of NGC1316 harbors two

stellar populations – old and young ones). The projected difference of rotation smaller than 50 km/s, therefore it is quite difficult to detect it in Line-of-Sight velocity distribution (LOSVD). The disk is thick because dynamical heating of the merging is still ongoing.

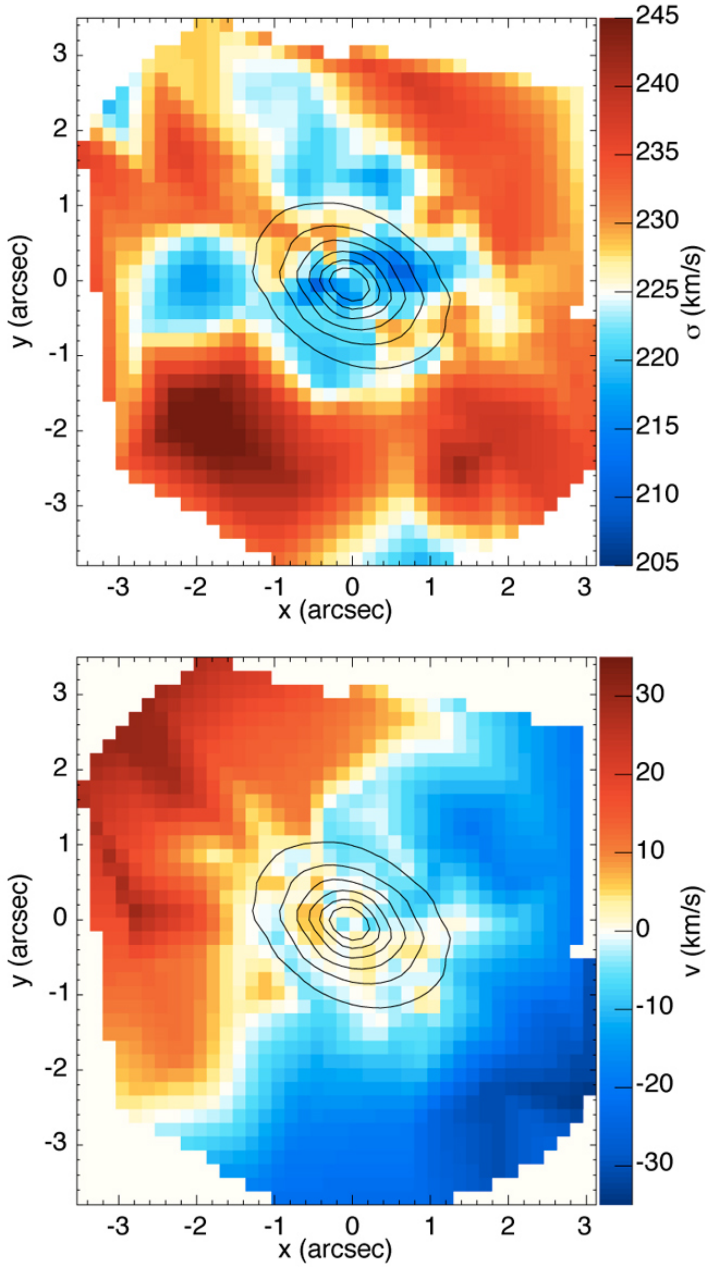

Figure 3.6: The 25 mas SINFONI kinematics (without convolution), provided by N.Nowak (private communication)

3.6 Summary

In this paper discuss the central region of the merger galaxy Fornax A, based on our ground-based near-infrared images and kinematics. Using 2D-decomposition analysis of the images we have detected a nearly exponentially distributed central brightness excess ($\sim$16% in Ks) with respect to an oblate Sersic's spheroid. A "peanut-shape" disk-like structure was found on the residuals in all observed bands, becoming most prominent in K-band. Its contribution to the total flux increases in NIR mainly due to both lower dust extinction in K-band and presence of a gradient in stellar population color towards the nucleus of Fornax A.

We analyzed already published kinematic data and complemented them with new spectroscopic observations taken in the region of CaT along the major axis of Fornax A and concluded that inner region of NGC1316 most probably harbors a kinematically decoupled core. We have outlined three possible explanations of the origin of this decoupling.

4

CaFe interstellar clouds

Monthly Notices of the Royal Astronomical Society, 2007, 378, 893

Bondar, A., Kozak, M., Gnaciński, P., Galazutdinov, G. , Beletsky,Y. and Krełowski, J.

Abstract

A new kind of interstellar cloud is proposed. These are rare (just a few examples among $\sim$ 300 lines of sight) objects with the Ca I 4227 Å, Fe I 3720 Åand 3860 Ålines stronger than those of K I (near 7699 Å) and Na I (near 3302 Å). We propose the name 'CaFe' for these clouds. Apparently they occupy different volumes from the well-known interstellar H I clouds where the K I and ultraviolet Na I lines are dominant features. In the CaFe clouds we have not found either detectable molecular features (CH, CN) or diffuse interstellar bands which, as commonly believed, are carried by some complex, organic molecules. We have found the CaFe clouds only along sight-lines toward hot, luminous (and thus distant) objects with high rates of mass loss. In principle, the observed gas-phase interstellar abundances reflect the combined effects of the nucleosynthetic history of the material, the depletion of heavy elements into dust grains and the ionization state of these elements which may depend on irradiation by neighboring stars.

4.1 Introduction

The chemical composition of interstellar clouds cannot be easily determined observationally. Clouds contain both gas and dust. The latter cannot be penetrated by spectroscopic observations. Only a limited number of atomic lines are available to ground-based observations: typically these are Ca II (H and K) lines, the sodium yellow doublet, the red doublet of potassium and very weak lines of Fe I, Ca I, Li I and Rb I. In the near-ultraviolet, another doublet of sodium (near 3302 Å) is observed, as well as several lines of ionized titanium. Lines of other elements are only very seldom available to ground-based spectrographs; the vast majority of elemental resonance absorption lines can be observed only from space-borne instruments. One can only speculate whether the total content of certain elements is the same in every cloud or varies from object to object.

Doppler splitting in the lines of interstellar gases has been a well-known phenomenon since the late 1930s (Beals 1938). High-resolution spectra usually allow us to resolve many Doppler components, proving that the sight-lines toward distant stars intersect many independent clouds (Welty et al. 2003). It has already been demonstrated that the Doppler components of different lines sometimes do not share the same radial velocities. The latter phenomenon was found to be especially striking in the case of the molecular CH+ feature versus those of Ca I and CH (Allen 1994). Different radial velocities, inferred either from Na I D_1 and D_2 lines or from the Ca II K line, were reported by Sembach et al. (1993). Recent articles by Megier et al. (2005) and Galazutdinov (2005) confirmed this effect, demonstrating that Ca II fills the interstellar medium quite uniformly while the carriers of other spectral features (typically of neutral species) are concentrated in small, probably dense clumps. The other spectral features, behaving probably in the same fashion as Ca II, are those of Ti II (Stokes & Hobbs 1976).

The last result proves that carriers of interstellar absorption features are not (or not always) spatially correlated. A set of interstellar absorptions, observed in a spectrum of a reddened star, may not be the spectrum of a well-defined environment but rather an ill-defined average of several environments, possibly characterized by different physical parameters. This motivates investigations of possible relations between Doppler components of different interstellar lines that share the same radial velocities. Single Doppler components probably form spectra of single clouds relatively homogeneous environments.

One of the most important results, derived from vacuum-ultraviolet satellite observations, is the presence of elemental depletions of the interstellar gas, since the amount of each element depleted has important consequences for theories of the formation of grains. Morton et al. (1973) analyzed the interstellar absorption lines in spectra of five reddened stars, and found evidence that several elements were depleted compared with the Sun; a very similar result was found for the well-known star ζ Oph (Morton 1974). This result was confirmed by Field (1974), who also related the elemental depletion to the condensation temperatures of several heavy elements observed. The observations proved that some of them (Ca, Ti, Al, Fe, Ni) are severely depleted while some others

(K, Na, Li) do not suffer strong depletion. The highest depletion (–3.6) is observed in the case of calcium (Welty et al. 1999); that of iron is also quite high (–2.2). Such observations certainly constrain the chemical composition of interstellar dust grains; one may assume (it cannot, however, be demonstrated observationally!) that the total content of different elements in any interstellar cloud resembles 'cosmic abundances' and thus, lacking atoms of the elements characterized by high condensation temperatures (such as Ca or Fe), must be incorporated into dust grains (Savage et al. 1992). Earlier results, based on (Orbiting Astronomical Observatory) OAO3 Copernicus data, were confirmed using the Hubble Space Telescope (HST) high-resolution Goddard High-Resolution Spectrograph (GHRS) spectrometer [see Savage & Sembach (1996) for a review]; the HST GHRS spectrograms proved also that some Doppler components carried by ionized species do not have counterparts in those of neutral carriers. The latter phenomenon can be seen in Ca II lines acquired from ground-based observatories (Megier et al. 2005).

We demonstrate that some Doppler components of interstellar lines show unusual strength ratios, possibly caused by a combined effect of elemental depletion and peculiar chemical composition. This paper is based on extensive sets of spectra from three observatories: Terskol (Russia), the European Southern Observatory (ESO) La Silla and ESO Paranal.

4.2 Observational data

The present analysis involves spectra obtained during several observing runs between 1996 to 2003 using three échelle spectrometers: Maestro, Feros and UVES.

- The first instrument is fed by the 2-m telescope of the Observatory at Peak Terskol (TE) in the Northern Caucasus. The spectrometer is equipped with a Wright Instruments CCD 1242x1152 matrix (pixel size 22.5μm $\times$ 22.5μm) camera (Musaev et al. 1999). The instrument forms echelle spectra which cover the range from 3,500 to 10,100 Å, divided into up to 92 orders. The existing set of gratings and cameras allows several resolutions: the applied ones range from R=45,000 through 80,000 to 120,000. The latter could have been applied only while observing relatively bright stars; in cases of heavily reddened, faint objects we had to restrict our data to the lowest possible resolution.

- The second instrument was the Feros echelle spectrograph of the European Southern Observatory, La Silla, which allows a fixed resolution $R \equiv \lambda/\Delta\lambda$ of 48,000. This instrument allows to get the whole available spectral range ($\sim$3700–9200 Å, divided into 37 orders) recorded in a single exposure. The flat-fielding can be done very precisely in the case of Feros as it is the fiber-fed spectrograph, but this is not of basic importance while measuring equivalent widths of reasonably narrow features.

- The third instrument is the UVES ESO – Paranal spectrograph. We used the archived data: the high resolution spectra of O and B stars. The spectrograph

TABLE 4.1: The selected targets.

Star	V	B-V	Sp	Spectrograph	R
HD 90177	7.42	0.88	B2evar	UVES	80,000
HD 93250	7.37	0.16	O3.5V	FEROS	48,000
HD 94910	6.96	0.61	B2:pe	UVES	80,000
HD 152270	6.61	0.23	WC+...	UVES	80,000
HD 157038	6.33	0.68	B4Ia+...	UVES	80,000
HD 193237	4.82	0.41	B2pe	MAESTRO	120,000
HD 207198	5.94	0.31	O9II	MAESTRO	120,000
HD 210839	5.05	0.25	O6e	MAESTRO	120,000

gives the resolution R=80,000 in the blue–UV range and R=110,000 in the yellow–red range. Only this spectrograph allows observations in the UV range i.e. below 3700 Å.

The selected targets are tabulated in Table 4.1 together with their basic data. All selected objects are reasonably reddened, hot luminous stars. We used the SIMBAD mean values for stellar parameters.

4.3 Results

In well-known 'normal' cases, the spectra of interstellar clouds demonstrate strong K I 7699 Å Na I D_1 and D_2 and Ca II H and K lines; Fe I and Ca I ones are much weaker. The near-ultraviolet Na I doublet lines at ~3302 Å usually are also much stronger than those of Ca I and Fe I. Among the spectra of more than ~300 reddened stars we found just a few objects demonstrating unusually strong Ca I 4227-Å and Fe I 3720-Å lines stronger than Na I? 3302-Å as well as K I 7699-Å ones. The dominant Fe I and Ca I Doppler components reveal specific objects which we propose to name as 'CaFe' interstellar clouds.

The data presented in this work can be provisionally divided into three groups.

- A vivid CaFe component: the cloud at ~-40 km s^{-1} seen towards HD 90177; and two overlapping ones at ~-50 km s^{-1} in the spectrum of HD 94910 (Figs 1 and 2). These clouds also produce strong Ca II lines and relatively weak sodium D ones, while K I (7699 Å) and Na I (3302 Å) lines are barely seen. Neighboring components represent 'normal' clouds, which evidently occupy different volumes of space; no components of either features of simple molecules or narrow diffuse band 6196 Å can be associated with the CaFe cloud.

- Evident but not so vivid CaFe clouds: a ~12 km s^{-1} cloud seen in spectra of HD 152270; and a weak one at ~9 km s^{-1} seen in spectra of HD 157038 (Figs 3 and 4). The potassium line is still undetectable here and the accompanying Ca II and Na I features are much weaker than in the previous case.

- Plausible candidates for CaFe clouds: HD 93250, 193237, 207198 and 210839 (Figs 58). The strong Ca I 4227-Å line is not shifted far enough from the centres of the Na I or K I lines; one can only observe a radial velocity difference relative to molecular features. Very high-resolution spectra are needed to clarify this uncertainty.

4.3.1 HD 90177 = HR Car

This star is a well-known very massive luminous blue variable (LBV) with a high mass-loss rate, 1.8×10^{-5} (White 2000). The two-component infrared nebula around HR Car was well studied in a set of publications (eg. Voors et al. 1997; White 2000). The star is very distant ($\sim$ 4.5 kpc) and thus the sight-line probably intersects many clouds between the star and the observer. In a detailed study, Nota et al. (1997) presented a kinematical picture of the HR Car nebula and estimated its chemical composition. Concerning the latter, it should be noted that they misidentified the 6614-Å diffuse interstellar band (DIB) as being the Fe I line. Very likely, we observe a mixture of circum- and interstellar features towards this object. However, it is very difficult to distinguish between them.

4.3.2 HD 94910 = AG Car

The second best CaFe example is also observed in the spectrum of a very high-luminosity star. AG Car is the prototype of the LBV class and has been extensively observed from ultraviolet to radio wavelengths with different observational techniques over several decades. Detailed information on the star can be retrieved from e.g. Groh et al. (2006). The star resides in a region that is very rich in molecular gas with complex motions. The star is characterized by a very high mass-loss rate of $2.3\text{-}6.0\times10^{-5}$ and is most probably surrounded by a circumstellar expanding shell (revealed by P Cyg-type line profiles) that provides the conditions of density and shielding necessary for survival of the detected CO molecules in the proximity of such a hot star (Nota et al. 2002).

Blue-shifted components at $\sim$–60 and $\sim$–110 s^{-1} have counterparts in the components originating in the circumstellar shell – see (Nota et al. 2002, fig. 8). However, only the cloud at $\sim$–60 s^{-1} shares its radial velocity with the CaFe cloud. It is thus difficult to decide whether the CaFe cloud is in fact a circumstellar object or whether the coincidence in radial velocities is just accidental.

4.3.3 HD 152270 = WR 79

HD 152270 is a spectroscopic binary with components WC7+O5–8 (Smith et al. 1990). Complex variability of line shapes and profiles suggests a colliding wind in the vicinity of the system (Luehrs 1997). We found no data allowing us to connect the CaFe feature with circumstellar gas, e.g. a kind of variability in correlation with the orbital period of the system. Perhaps observations covering this 8-d period may help us to discover the variability of the CaFe cloud line intensities and/or positions.

4.3.4 HD 157038

HD 157038 is a high-luminosity early-type star, having passed through the red supergiant phase and now evolving bluewards in the HertzsprungRussell diagram (according to Dufton & Lennon 1989). There are no signs of the existence of circumstellar material around it, except a weak emission in H_α. The CaFe cloud here is not as strong as in the previously discussed objects but evidently seen at ∼9 $\mathrm{km\,s^{-1}}$.

4.3.5 HD 93250, HD 193237 = P Cyg, HD 207198 and HD 210839

This group of four stars does not demonstrate evident CaFe clouds well resolved from 'normal' ones by means of Doppler splitting. All of them show a strong Ca i 4227-Å line which has no evident counterpart in Na I, Ca II or K I lines: their small radial velocity shifts put them inside the saturated profiles of strong interstellar lines. Perhaps very high resolution (R= 200 000 or higher), if applied, may allow a more confident separation of the CaFe clouds.

- HD 193237 (P Cyg) is one of the three best-known Galactic LBVs and belongs to the η Car complex. The star is one of the most luminous and massive objects in our Galaxy (Kudritzki 1980). Its very high effective temperature, Teff= 52 500 K (Kudritzki 1980), means that any cloud with neutral Na or K gas may survive only at a sufficiently large distance from the star and/or if it is shielded by a circumstellar disc.

- HD 93250 is a very hot O star, practically without any emission features, so without a circumstellar shell.

- HD 207198 is a supergiant with the lowest mass-loss rate (∼0.8-0.9$\times10^{-6}$ $M_\odot$) (Markova et al. 2004) of our sample. A strong Ca I line at ∼–9 $\mathrm{km\,s^{-1}}$ and a strong (but unfortunately noisy in our spectra) line of Fe I are slightly red-shifted relative to other interstellar features. Therefore we classify this cloud as a CaFe one. The spectrum of the star shows no signs of a circumstellar shell or a disc.

- HD 210839 is a very hot O6 star, with a luminosity higher than that of HD 207198; its mass-loss rate is estimated as quite high (Markova et al. 2004), and perhaps the star is a runaway object (Gies 1987). However, our spectra of this star do not show any sign of mass loss, except some H_α emission. Underhill (1995) studied H_α profiles and supposed that their observed form results from blending of an emission line, formed as a result of infall from a circumstellar disc, and an absorption feature formed in the column of the average wind of the star projected against the face of the star. The CaFe effect is not evident, but a weak Ca I component near ∼–2 $\mathrm{km\,s^{-1}}$ probably reveals a cloud of this type.

Table 4.2: Measured heliocentric radial velocities ($\mathrm{km\,s^{-1}}$), column densities ($\mathrm{cm^{-2}}$) and equivalent widths (mÅ).

Star	Na I 3302 Å			Fe I 3720 Å			Ca I 4227 Å			K I 7699 Å		
	V_h	Col. D.	EW	V_h	Col. D.	EW	V_h	Col. D.	EW	V_h	Col. D.	EW
HD 90177	-39.2	2.80±0.3(12)	2.5±0.3	-40.4	4.24±0.3(12)	19.7±0.2	-40.5	5.94±0.6(10)	15.7±1.2	-	-	-
	-8.8	6.93±0.4(13)	45.4±0.3	-10.2	2.15±0.1(11)	1.1±0.1	-10.6	1.78±0.6(10)	4.9±0.1	-9.6	8.16±0.3(11)	102.0±2.7
	-1.1	2.52±0.2(13)	19.6±0.2	-1.0	3.72±0.2(11)	1.9±0.1	-	-	-	0.0	4.51±0.2(11)	68.2±0.5
	5.0	6.67±0.1(13)	44.6±0.3	5.7	5.47±0.4(11)	2.7±0.1	4.4	3.23±0.9(10)	8.8±0.4	4.5	6.19±0.3(11)	80.5±0.7
HD 93250	-	-	-	-14.5	9.72±3.7(11)	2.3±0.5	-13.7	2.44±0.6(10)	6.8±0.2	-16.8	3.31±0.2(11)	51.9±1.6
	-	-	-	-3.6	1.63±0.1(12)	4.6±0.3	-3.7	5.63±1.2(10)	15.8±1.1	-2.1	1.14±0.2(11)	29.9±1.1
	-	-	-	7.5	6.81±1.8(11)	1.8±0.4	7.4	2.61±0.1(10)	4.8±0.1	3.5	2.73±0.3(11)	34.9±0.7
HD 94910	-	-	-	-60.2	4.03±0.5(11)	2.0±0.2	-60.9	6.69±0.4(09)	1.9±0.2	-	-	-
	-	-	-	-53.5	7.11±0.6(11)	3.5±0.5	-54.9	1.87±0.1(10)	5.1±0.4	-	-	-
	-13.0	7.87±0.5(12)	6.8±0.4	-	-	-	–	-	-	-14.9	2.79±0.2(10)	4.8±0.1
	-6.0	1.17±0.1(13)	9.8±0.8	-	-	-	-6.7	2.16±0.3(09)	0.6±0.1	-7.8	1.77±0.1(11)	28.4±1.0
	2.4	2.96±0.2(13)	22.9±0.3	-	-	-	0.1	1.73±0.2(10)	4.8±0.5	1.2	2.40±0.2(11)	37.0±1.1
	6.6	6.52±0.4(12)	5.5±0.2	-	-	-	-	-	-	5.7	1.44±0.1(11)	23.2±0.8
	10.4	1.52±0.2(13)	13.3±0.4	-	-	-	-	-	-	10.1	1.22±0.1(11)	19.9±0.2
HD 152270	1.2	4.89±0.3(13)	33.5±1.2	0.6	4.53±0.2(11)	2.3±0.2	1.3	7.91±2.2(09)	2.2±0.2	1.9	7.01±1.0(11)	99.0±2.0
	15.7	6.25±1.0(11)	0.6±0.1	13.6	1.75±0.1(11)	0.9±0.2	13.4	6.49±1.3(09)	1.8±0.2	12.4	1.74±0.5(10)	3.0±0.5
HD 157038	-31.1	3.53±0.2(12)	3.1±0.1	-	-	-	-	-	-	-32.1	5.44±0.3(09)	1.0±0.1
	-25.5	4.61±0.3(12)	4.0±0.2	-	-	-	-24.7	3.35±0.2(09)	0.9±0.0	-23.9	5.71±0.3(10)	9.8±0.5
	-15.9	3.08±0.1(13)	24.8±1.0	-	-	-	-14.5	3.22±0.2(09)	0.9±0.0	-14.3	2.74±0.1(11)	44.4±0.2
	-7.8	1.59±0.1(13)	13.0±0.5	-8.3	7.10±0.5(11)	3.6±0.2	-6.5	1.48±0.1(10)	4.1±0.2	-6.8	2.36±0.1(11)	37.2±0.3
	-2.4	1.76±0.2(13)	14.3±0.4	–	-	-	-	-	-	-1.7	1.58±0.0(11)	25.5±0.2
	-	-	-	9.2	1.96±0.1(11)	1.0±0.1	8.7	4.13±0.3(09)	1.2±0.0	6.1	1.50±0.1(10)	2.6±0.1
HD 193237	-	-	-	-17.5	1.05±0.3(12)	5.2±1.2	-18.8	1.68±0.2(10)	4.6±0.2	-17.4	6.94±0.3(10)	11.8±0.2
	-	-	-	-6.2	4.68±1.0(11)	2.3±0.6	-9.5	9.93±0.5(09)	2.7±0.1	-10.3	1.44±0.1(11)	23.8±0.3
HD 207198	-	-	-	-	-	-	-13.7	3.72±0.5(10)	10.2±1.3	-14.7	1.87±0.1(12)	211.3±3.6
	-	-	-	-9.5	1.05±0.3(12)	5.1±1.4	-8.6	1.97±0.2(10)	5.4±0.4	-8.4	2.09±0.1(11)	31.9±1.5
HD 210839	-	-	-	-12.5	4.83±1.5(11)	2.4±0.7	-11.3	2.71±0.1(10)	7.4±0.6	-14.0	7.86±0.3(11)	101.6±1.9
	-	-	-	-	-	-	-2.3	7.40±0.3(09)	2.0±0.4	-4.8	2.36±0.1(11)	38.0±0.2

Table 4.2 summarizes the column densities of Ca I, Na I, Fe I and K I of all observed Doppler components together with their radial velocities and equivalent widths; in the case of Na i they refer to the shorter wavelength member of the doublet. It is evident that the abundance ratios vary by several orders of magnitude.

4.4 Discussion

The typical weakness of the Ca I or Fe I lines observed in 'normal' H I clouds follows from the serious depletion of their carriers. In a cloud composed of pure atomic gas of solar composition, the Ca i 4227-Å line should be as strong as any of the members of the yellow sodium doublet (D_1 and D_2). Apparently a large fraction of the calcium and/or iron atoms are included in dust particles. It is also possible that the total chemical composition (i.e. involving both gas and dust) changes from cloud to cloud because of, for example, a nearby supernova explosion or a mass-loss process that takes place in the nearby stars. The observed intensity of atomic lines may also depend on the ionization of the observed clouds, but a serious change of the spectra would require a selective ionization which does not seem likely.

The atomic abundances of the gaseous component of the LBV nebulae might be different from the cosmic one at the time of the ejection as a result of several effects:

1. a fraction of C and O may have been locked into CO, and several atomic species

may be depleted because of dust, in particular O and Si;

2. the nebula may have mixed with the gas of the interstellar bubble into which it was ejected;

3. the nebula may have mixed with the wind from the star after it was ejected (Lamers et al. 2001).

Infrared studies of LBV nebulae have shown that they contain a significant amount of CO and dust (e.g. McGregor et al. 1988). Most LBV nebulae contain O-rich dust, with a small contribution of C-rich polycyclic aromatic hydrocarbons (PAHs). Thus dust is mainly in the form of amorphous silicates, such as MgFeSiO4 and Fe2SiO4, plus a minor contribution from crystalline silicates, such as olivines and pyroxenes (Voors et al. 2000). Different effects may have changed the gas composition of the nebula since it was ejected: mixing with the swept-up gas from the wind-blown bubble or with the gas from the faster wind of the central star, and depletion by CO and dust. The above processes may lead to the formation of CaFe clouds only if they are formed in circumstellar space. Various properties of our targets and the scarcity of the sample do not allow us to state definitely whether the CaFe clouds are circumstellar or really interstellar objects.

The CaFe clouds must be optically thin as the mass should be roughly proportional to the column density of Na I or K I; abundances of these elements are roughly proportional to the total hydrogen abundance (H I+ H2) see Fig. 4.9 as they may only be slightly depleted. We have measured intensities of the K i lines in the spectra of all stars for which the hydrogen column densities have already been published (Savage et al. 1977) or (Rachford et al. 2002). These measurements are collected in Table 4.3.

Apparently K I correlates reasonably well with the total hydrogen (Fig. 4.9). The scatter is probably the result of the ionization of potassium – an element of very low ionization potential (4.3 eV). The neutral potassium is almost perfectly correlated with the neutral sodium (Fig. 4.9). According to the published results of Savage & Sembach (1996) and Welty et al. (1999), both sodium and potassium are of similar abundance in the interstellar gas (approximately 10 times lower than solar) and the depletion of iron is at least an order of magnitude greater; that of calcium, even more. The presence of CaFe clouds, apparently free of molecular species (at least they do not contain an observable amount of DIB carriers), must make a correlation between Ca i or Fe i lines and other interstellar absorptions quite poor as already demonstrated by Welty et al. (2003).

Fig. 4.9 demonstrates that the column density of iron in the gas phase remains roughly constant while that of K I is growing above a certain limit. Apparently, the fraction of iron (and calcium) atoms incorporated into dust grains grows proportionally to the mass of the cloud. Possibly these elements are fully consumed by dust particles in cloud cores and the observed abundances represent only peripheral layers. Interstellar clouds are exposed to the radiation of neighboring hot stars, which may change their physical parameters significantly. In particular, a large fraction of potassium atoms could be ionized. Unfortunately, we cannot reliably measure the distances of interstellar

Table 4.3: Total column densities of hydrogen (HI+H_2)$\times 10^{20}$ and equivalent widths of KI 7699 Å line (mÅ).

Star	EW KI	N(H)	Star	EW KI	N(H)
HD 2905	83.8	19.8	HD 144470	21.9	17.3
HD 10516	14.5	3.7	HD 145502	36.6	15.6
HD 22951	54.1	16.8	HD 148184	83.4	22.6
HD 23180	93.7	16.1	HD 148605	6.2	9.1
HD 24398	75.4	15.8	HD 149038	58.1	15.6
HD 24760	3.5	3.2	HD 149757	65.3	14.1
HD 24912	63.5	19.8	HD 150898	31.7	10.3
HD 30614	62.9	12.4	HD 151804	30.0	15.6
HD 37742	10.1	2.6	HD 155806	47.0	13.7
HD 38771	9.9	3.3	HD 184915	28.9	12.1
HD 40111	23.7	9.1	HD 188209	52.9	10.0
HD 47839	16.7	2.5	HD 200120	11.1	2.2
HD 91316	4.3	1.8	HD 203064	76.5	14.0
HD 112244	50.6	14.8	HD 209975	86.1	15.4
HD 141637	14.0	15.8	HD 210839	147.8	25.0
HD 143275	31.3	14.5	HD 214680	19.0	5.3
HD 144217	23.6	13.7	HD 224572	58.5	10.9

clouds, and even those of stars are known with a rather limited accuracy. This limits the possibility of building a quantitative model of the depletion.

One of the important questions is whether CaFe clouds contain interstellar molecules and, especially, the carriers of DIBs, commonly believed to be some complex, carbon-bearing molecules. In Figs 4.1–4.8 we have compared the radial velocities of iron, calcium, sodium and potassium with those of CH, CH+ and DIB 6196. The intrinsic wavelengths of the latter have been taken from Galazutdinov et al. (2000). In this survey, DIB wavelengths have been estimated based on spectra of HD 23180 where almost no Doppler splitting is observed in interstellar lines (at least not of the magnitude seen in Figs 1–8).

It is clear that both simple molecular species and the complex ones (DIB carriers) are typically situated in the clouds characterized by a rather strong depletion of heavy elements. Apparently, the CaFe clouds contain very little if any CH or DIB carriers. It seems thus ill-advised to determine the rest wavelengths of DIBs by measuring the radial velocities of interstellar clouds from current wavelengths of Fe I or Ca I lines. The correlation between the two latter is also far from being perfect. They do not behave in unison and thus the process of grain formation involving heavy elements is simultaneous. It is interesting to consider whether the CaFe clouds may be thought of as building blocks for more massive clouds. The currently available sample does not permit us to estimate the mass contained in CaFe clouds; we observe just a few of them. They have been discovered in the spectra of very luminous stars the only objects that can be observed spectroscopically with high resolution and signal-to-noise ratio at large distances. This may suggest a relative scarcity of CaFe clouds. High-resolution spectra should allow us to make a statistically meaningful survey of these newly discovered objects. It is also important to survey extraterrestrial spectra to search for other elements that behave either like Ca I and Fe I or like K I and Na I.

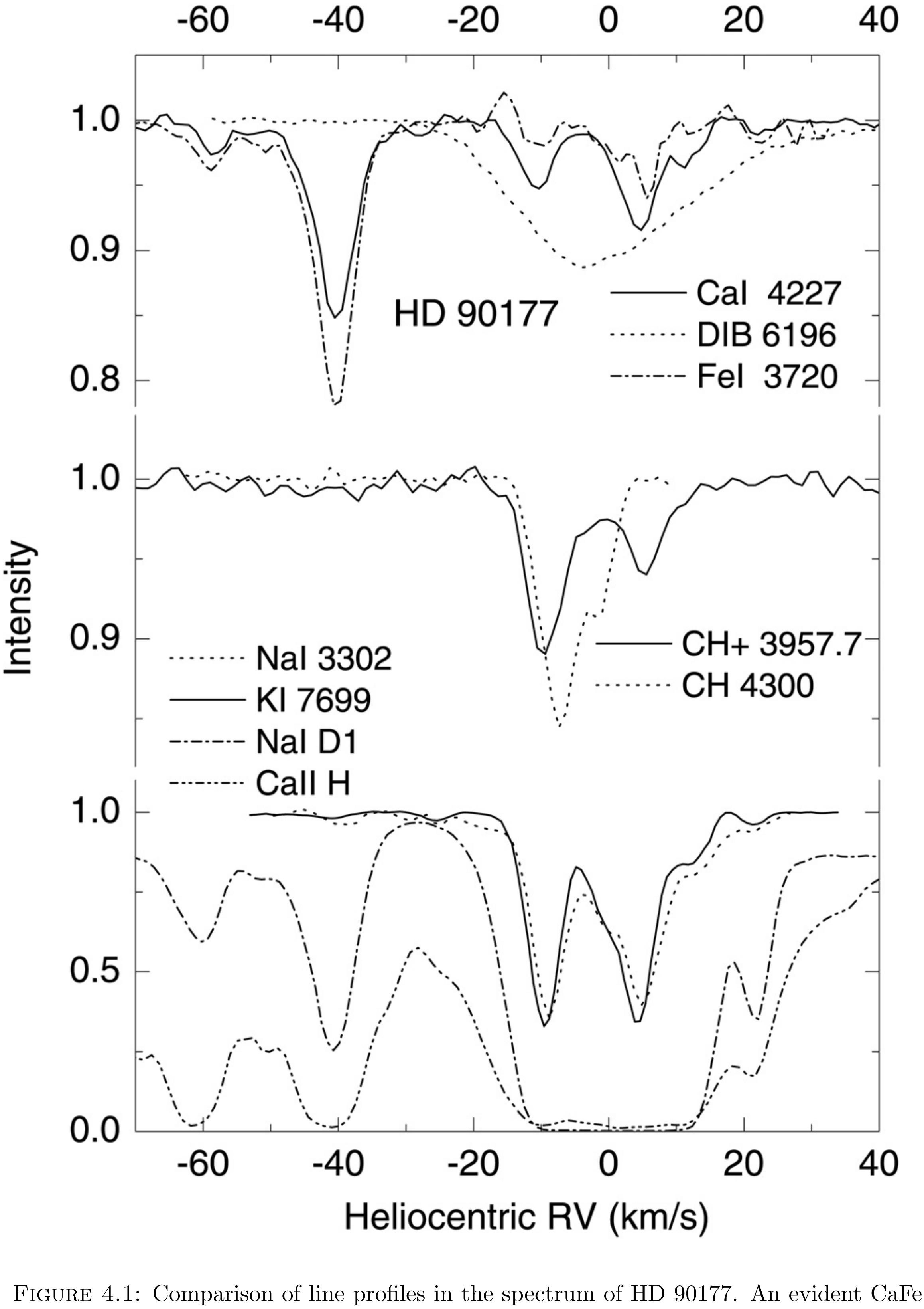

Figure 4.1: Comparison of line profiles in the spectrum of HD 90177. An evident CaFe Doppler component is seen at ∼–40 km s^{-1}.

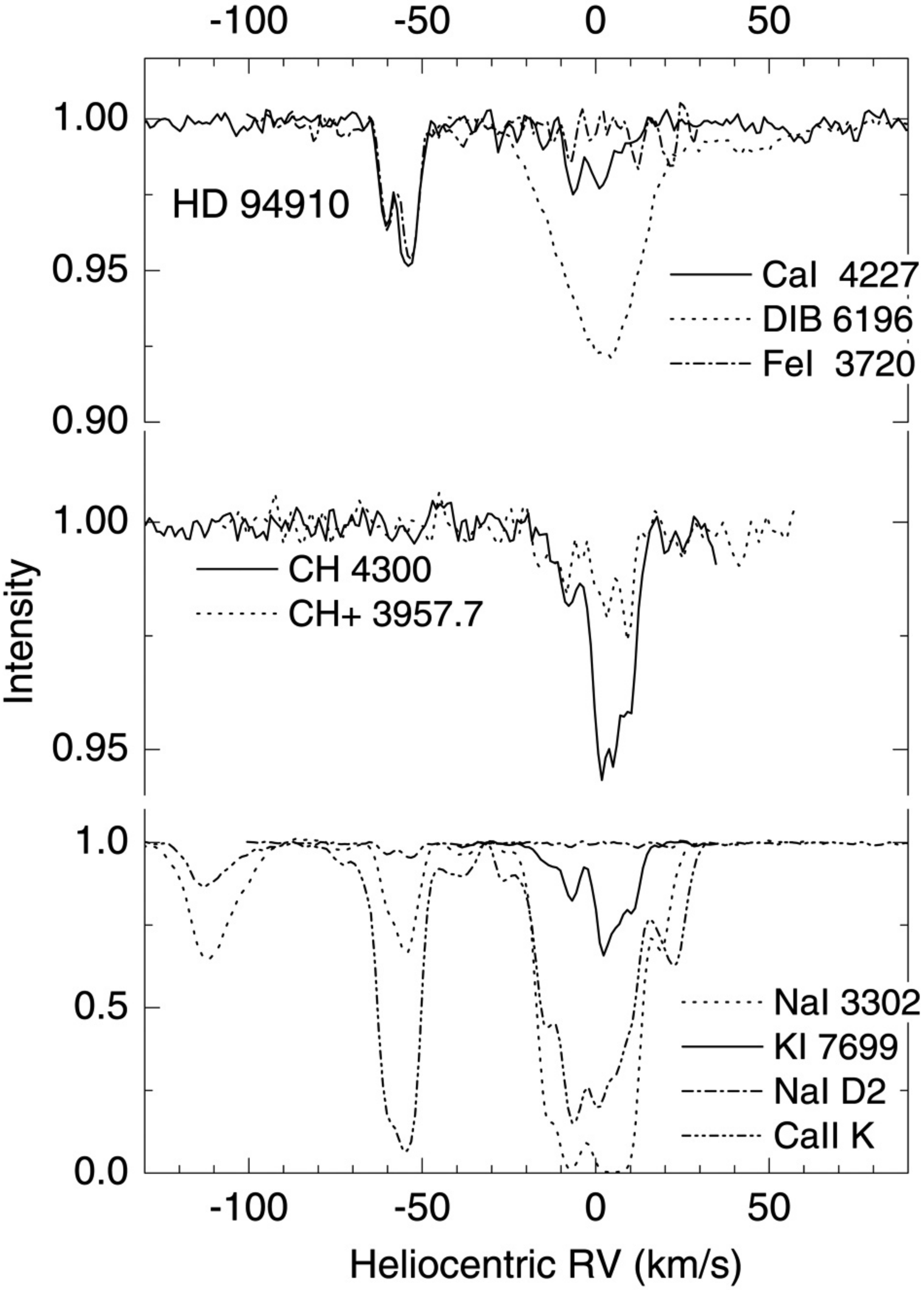

FIGURE 4.2: Comparison of line profiles in the spectrum of HD 94910. An evident CaFe component, perhaps a blend of two, is seen at ∼–50 km s^{-1}. The K I CaFe component is blended with a strong telluric feature.

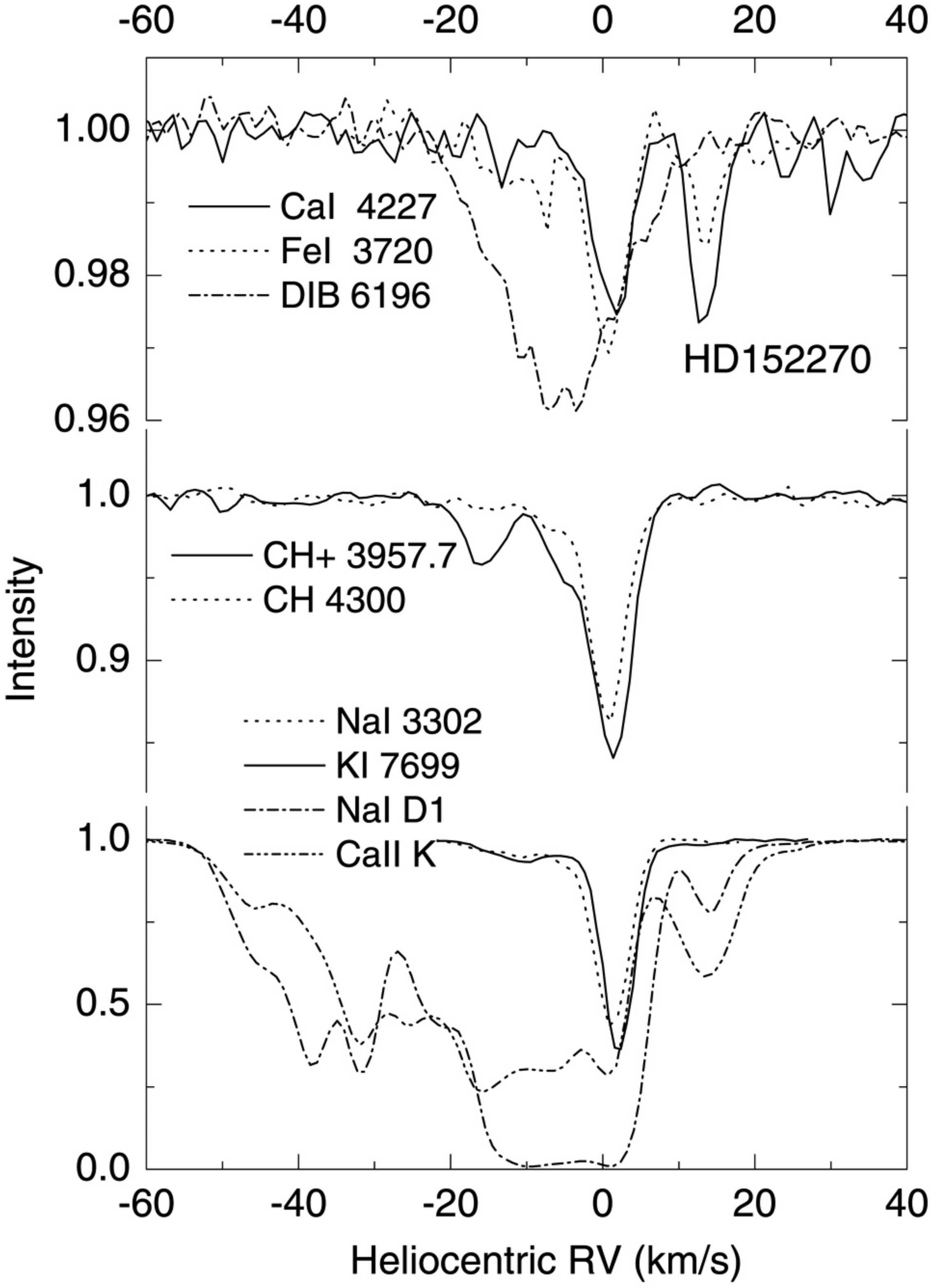

Figure 4.3: As in Figs 4.1 and 4.2 but for HD 152270. A CaFe cloud can be found at $\sim$12 $\mathrm{km\,s^{-1}}$.

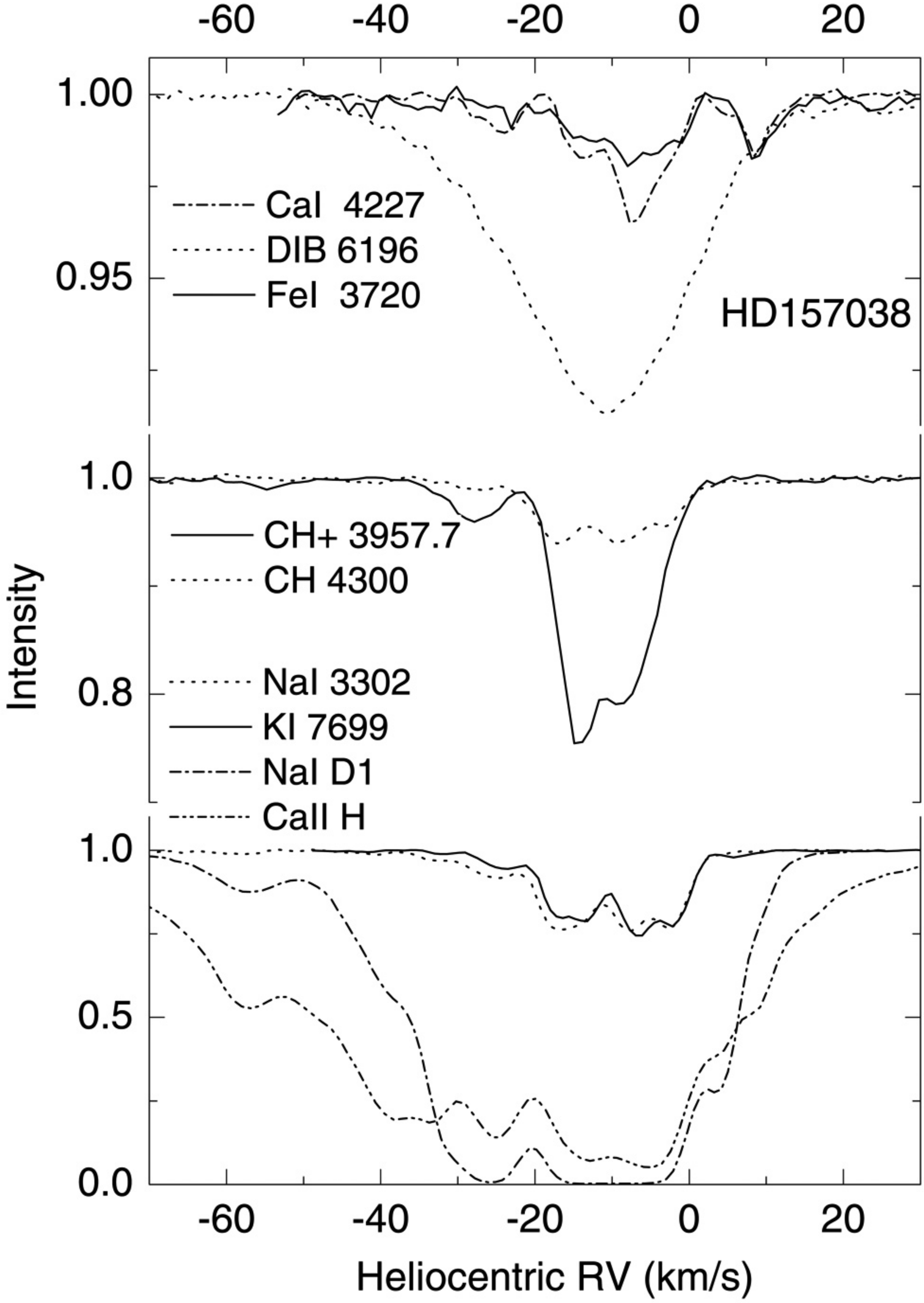

FIGURE 4.4: As in previous figures but for HD 157038. A weak CaFe cloud is seen at ∼–9 km s^{-1}.

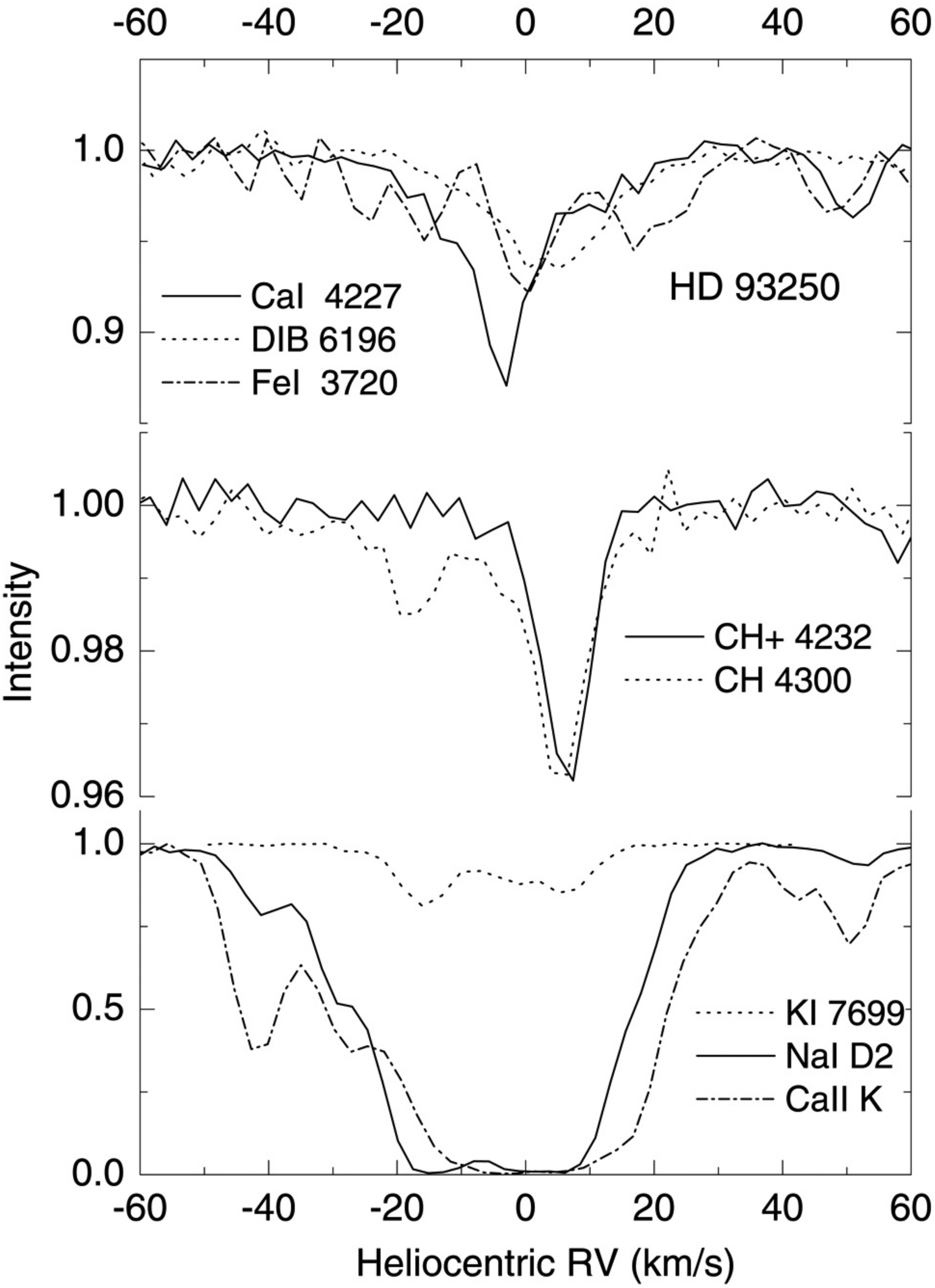

Figure 4.5: A possible CaFe component at $\sim$–3 km s^{-1} in the spectrum of HD 93250.

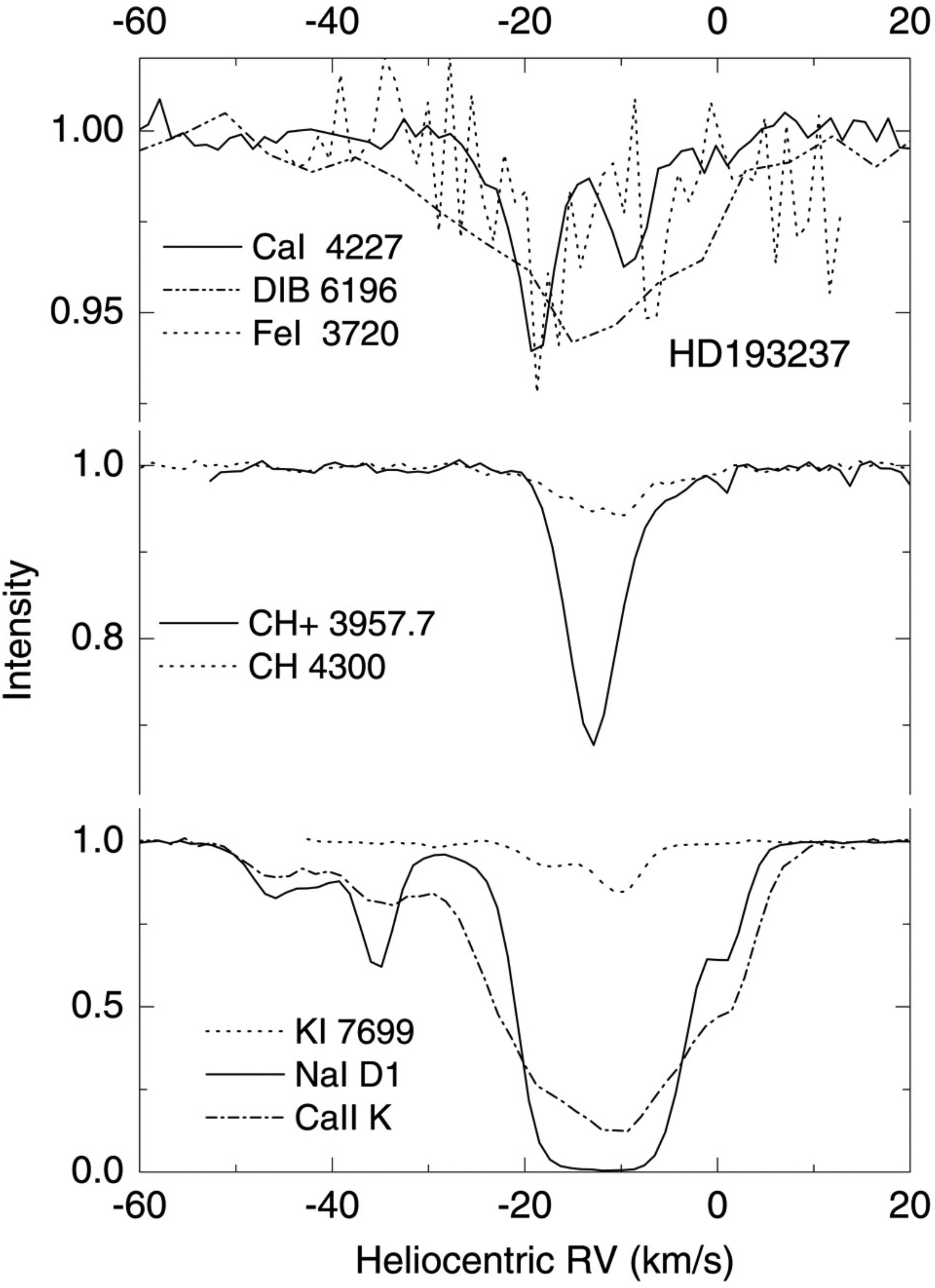

FIGURE 4.6: A possible CaFe component at ∼–20 km s^{-1} in the spectrum of HD 193237.

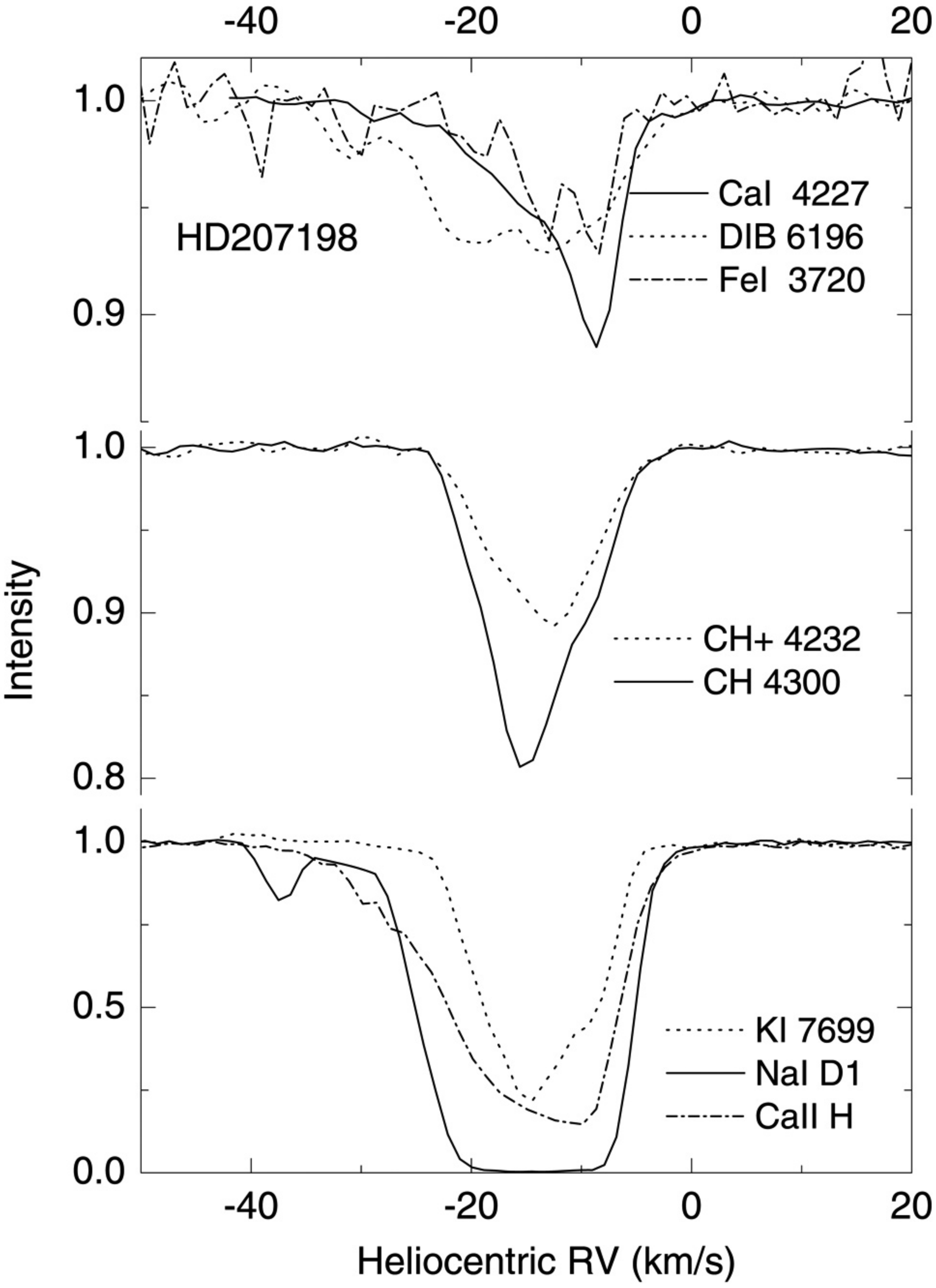

Figure 4.7: A possible CaFe component at ∼–9 $\mathrm{km\,s^{-1}}$ in the spectrum of HD 207198.

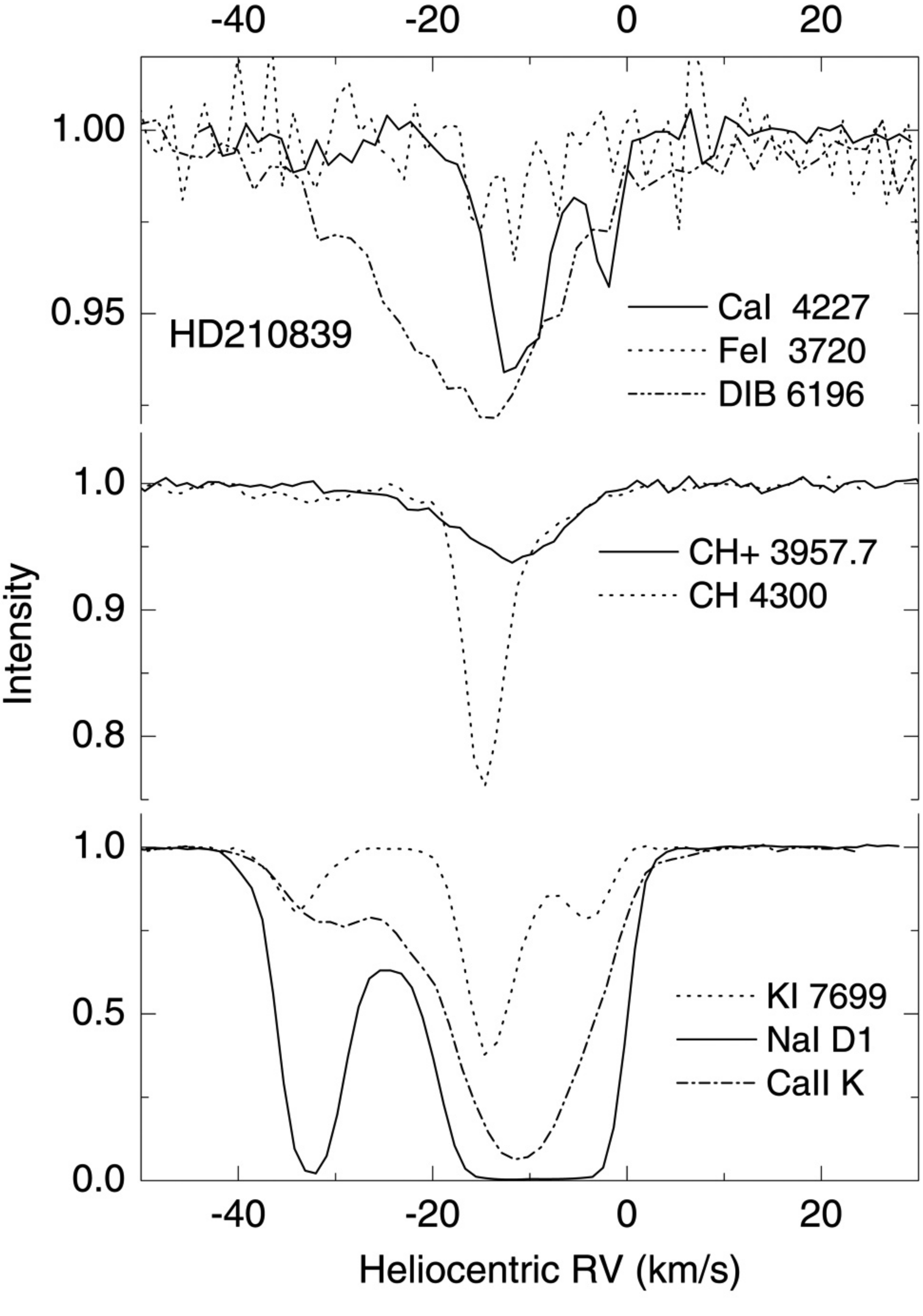

FIGURE 4.8: A possible CaFe component at ∼–2 km s^{-1} in the spectrum of HD 210839.

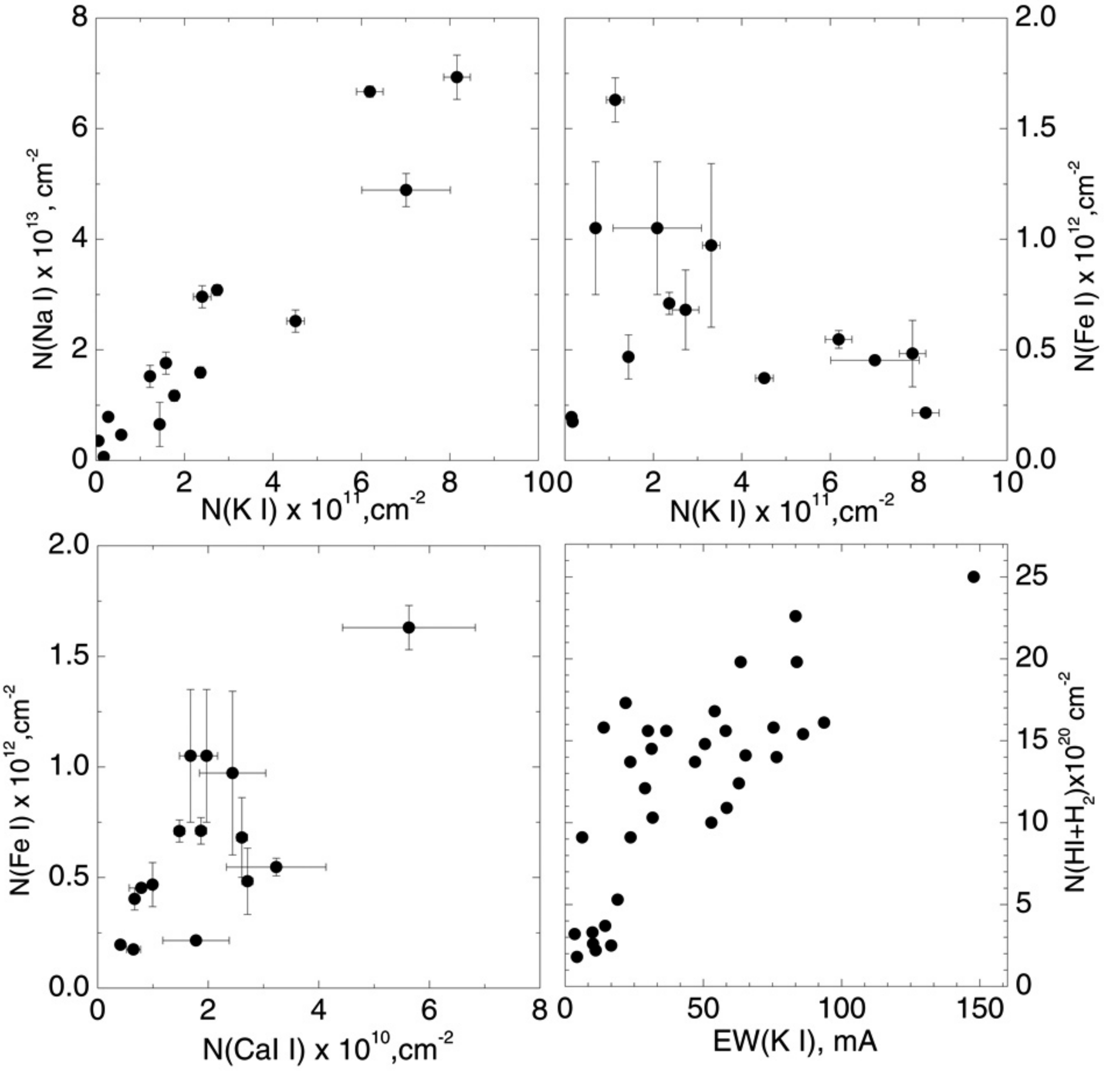

Figure 4.9: Correlations between column densities of the elements under consideration. The last panel depicts the data from Table 4.3.

5

A self-consistent system of CH molecule oscillator strengths

submitted to Astronomy& Astrophysics

Weselak, T., Galazutdinov, G., Beletsky, Y., Musaev, F. , and Krełowski, J.

Abstract

Detailed analysis of intensity ratios of unsaturated methylidyne (CH) A–X, B–X and C–X bands suggests inconsistency of the published oscillator strengths. While the latter are consistent for the main B–X and C–X transitions we suggest the new oscillator strength of the CH A–X band 4300.313 Å to be equal to $434 \pm 31 \times 10^{-5}$. This result is based on the assumption that f-values of CH B-X system (at 3886 and 3890 Å), i.e. 320 and 210×10^{-5} respectively are correct. We also recommend the oscillator strengths of the CH C–X lines at 3137.5582, 3143.1647 and 3145.9965 Å to be (in 10^{-5} each) 415±30, 640 and 267±17 respectively. This result is obtained on the basis of spectra of 52 stars (in 39 objects all CH features are unsaturated) acquired with four echelle spectrographs situated in both the Northern and Southern hemispheres. The estimated methylidyne column densities, obtained using the new, consistent system of the oscillator strengths, toward the observed targets are given as well.

5.1 Introduction

Interstellar lines of CH molecule have been discovered by the Mount Wilson observers and identified by McKellar (1940a,b) in spectra of OB stars due to its A–X feature centered near 4300 Å as the strongest observed interstellar line in the violet region easily accessible to photographic observations. Also the B–X system near 3886 Å is quite frequently observed though much weaker than the A-X band. Abundances of CH molecule were proved to be very tightly correlated with those of H_2 molecule (Mattila 1986; Weselak et al. 2004; Liszt 2007). A majority of the published column densities of CH molecule base on measurements of the equivalent widths of the strongest A-X feature; sometimes also B–X is being applied (Weselak et al. 2008b). However, in many cases the A–X feature of CH molecule is saturated which leads to differences in the column densities estimated for the same object (in the case of HD 23180 the published value of column density of Federman (1982) and Crane et al. (1995) differs by a factor of 2). Column densities of CH molecule base on experimentally determined values of oscillator strengths which also do not coincide in many cases (see Table 2 in Lien 1984) and it is not an easy task to decide which of the published oscillator strengths is the most precise and should be applied. The f-values appear in the literature in one of two forms: the band oscillator strength ($f_{\nu'\nu''}$) and oscillator strength for individual line or blend of lines ($f_{J'J''}$). The former can be derived on the basis of radiative lifetime measurements (see formulae in Larsson 1983) or ab initio calculations. The latter can be obtained from $f_{\nu'\nu''}$ through the use of the Hönl-London factor for the transition of interest. However, the conversion of $f_{J'J''}$ shows uncertainties, even of the order of 2 (Lien 1984). As a consequence accurate assessment of measured line data requires considerable attention. In this paper we examine equivalent widths (W_λ) ratios of the A–X and B–X and C–X systems of CH molecule measured on the sample of 49 high-resolution spectra of OB stars, seeking unsaturated features for the analysis. In Table 5.1 we present transition and positions in the case of each band of CH molecule tested in this paper.

5.2 Observational material

Our observational material was collected using four echelle spectrographs:

Most of our observational material, listed in Table 5.2, was obtained using the UVES (u - in Table 5.2) spectrograph at ESO Paranal in Chile with the resolution R = 80,000. Spectra cover the range from 3,040 to 10,400 Å. They were acquired as a part of the ”Library of High-Resolution Spectra of Stars across the Hertzsbrung-Russell Diagram” and are available at the website: http://www.sc.eso.org/santiago/uvespop. For more information see Bagnulo et al. (2003).

The spectra of 7 objects were obtained with the HARPS spectrometer (marked with h in Table 5.2), fed with the 3.6m ESO telescope in Chile (see http://www.ls.eso.org/lasilla/sciops/3p6/harps/). This spectrograph allows to cover the range ∼3800 – ∼6900 Å with the resolution of R = 115,000. As the instrument designed to search for exoplanets, it guarantees very precise wavelength measurements.

TABLE 5.1: Optical and ultraviolet transitions of CH molecule. Data on wavelength measurements are from ^{a} – Gredel et al. (1993), ^{b} – this work.

Transition	Band	Line	Wavelength Å
$A^2\Delta$ – $X^2\Pi$	(0, 0)	$R_{2e}+R_{2f}$	4300.3132^a
$B^2\Sigma^-$ – $X^2\Pi$	(0, 0)	$^PQ_{12}$	3890.217^a
		$^QR_{12}+Q_{12}$	3886.409^a
		R_2	3878.774^a
$C^2\Sigma^+$ – $X^2\Pi$	(0, 0)	$^PQ_{12}$	3145.9965^b
		$Q_2+{}^QR_{12}$	3143.1647^b
		R_2	3137.5582^b

The spectra of 13 objects were acquired using spectrograph MAESTRO fed by the 2-m telescope of the Observatory at Peak Terskol (t) in the Northern Caucasus (Musaev et al. 1999), see also http://www.terskol.com/telescopes/3-camera.htm). The spectrometer is equipped with a Wright Instruments CCD 1242x1152 matrix (pixel size 22.5μm × 22.5μm) camera. The instrument forms échelle spectra that cover the range from 3,500 to 10,100 Å, divided into up to 92 orders. The existing set of gratings and cameras allows several resolutions: from R = 45,000 through 80,000 to 120,000. In this project we used the R=80,000 resolution.

The most recent observations were carried out using the fiber-fed echelle spectrograph installed at the 1.8-m telescope of the Bohyunsan Optical Astronomy Observatory (BOAO) in South Korea (b). The spectrograph has three observational modes providing a resolving power of 30,000, 45,000, and 90,000. In all the cases it allows recording of the whole spectral range from ~3500 to ~10,000 Å divided into 75-76 spectral orders. We used the highest resolution mode in our project.

All the spectra were reduced with the standard packages: MIDAS and IRAF, as well as our own DECH code (Galazutdinov 1992), which provides all the standard procedures of image and spectra processing. Using different computer codes to the data reduction procedures reduces the possibility of inaccuracies following the slightly different ways of dark subtraction, flat-fielding, or excision of cosmic ray hits. Most of our spectra from UVES were also taken from the archive as pipeline-reduced products (UV-Visual Echelle Spectrograph user manual) which allowed another comparison of the precision of the measured wavelengths.

It is to be emphasized that the correct continuum placement is the main source of errors during equivalent width measurement. In case of each spectral line the procedure presented in the publication of Weselak et al. (2008a) was performed. The error estimates were done using the formulation of Smith et al. (1984). The errors obtained on the basis of each fit are also presented in Table 5.2.

For this project we selected a sample of 52 reddened stars; in their spectra both A–X, B–X and/or C–X CH bands at 4300, 3886 and 3144 Å are seen. Table 5.2 presents HD numbers, spectral types and luminosity classes as well as the E(B-V) for each star and equivalent widths (W_λs) (in mÅ) of each CH band at 3137, 3143, 3146, 3878, 3886, 3890 and 4300 Å. In the last two columns we present column densities obtained on the basis of CH B–X band and CH A–X band with the newly proposed oscillator strength discussed in the next section.

TABLE 5.2: Observational and measurement data. Given are: star name (observed at b - Bohyunsan (S. Korea), t - Terskol (Russia), h - HARPS, u - UVES Paranal (Chile)), spectral and luminosity class, reddening, equivalent widths of the CH C-X (at 3137, 3143, 3146 Å), B-X (at 3878, 3886, 3890 Å) and A-X 4300 Å band, column density derived from CH B-X bands at 3886 and 3890 Å and abundance of the CH molecule obtained on the basis of new f-value of the unsaturated A-X band at 4300 Å equal to 434×10^{-5}.

HD		Sp/L	E(B-V)	W(3137)	W(3143)	W(3146)	W(3878)	W(3886)	W(3890)	W(4300)	N(B-X)	N(A-X)
				mÅ	mÅ	mÅ	mÅ	mÅ	mÅ	mÅ		$f=434\times10^{-5}$
21291	t	B9Ia	0.44					3.94 ± 0.45		15.35 ± 1.10		21.36 ± 1.56
22951	t	B0.5V	0.24					2.74 ± 0.35		8.91 ± 0.85		12.54 ± 1.24
23180	b	B1III	0.27					4.34 ± 0.56	3.76 ± 0.45	14.87 ± 1.23	23.52 ± 2.91	20.94 ± 1.75
24398	t	B1Iab	0.29				1.34 ± 0.45	4.96 ± 0.54	3.01 ± 0.38	15.87 ± 0.20	22.30 ± 2.61	22.34 ± 0.28
24534	b	O9.5pe	0.56				3.11 ± 0.45	8.55 ± 1.23	5.57 ± 0.54	25.71 ± 2.13	39.79 ± 2.57	
24912	t	O7.5Iab	0.30					3.08 ± 0.56	2.45 ± 0.45	10.34 ± 0.97	15.91 ± 2.91	14.56 ± 1.38
27778	t	B3V	0.37				3.54 ± 0.89	8.14 ± 0.78	5.35 ± 0.64	23.82 ± 2.67	38.05 ± 3.22	
34078	b	O9.5Ve	0.49				6.02 ± 0.56	15.89 ± 1.23	10.50 ± 0.67	50.12 ± 4.87	74.48 ± 5.88	
36371	t	B5Iab	0.45					3.74 ± 0.43		13.79 ± 1.20		19.42 ± 1.71
58343	u	B2Vne	0.14	0.95 ± 0.76	1.71 ± 0.45			1.10 ± 0.34		3.36 ± 0.45		4.73 ± 0.64
68761	u	B0.5III	0.14	1.56 ± 0.57	3.56 ± 0.45		0.85 ± 0.34	3.26 ± 0.34	2.43 ± 0.30	9.23 ± 0.67	16.26 ± 1.86	13.00 ± 0.95
76341	u	B1/B2Ib	0.46	3.92 ± 1.03	9.23 ± 1.03	5.40 ± 0.87	2.81 ± 0.45	8.24 ± 0.56	5.32 ± 0.45	25.83 ± 2.10	38.18 ± 2.91	
92740	u	WN7	0.36	1.23 ± 0.56	2.32 ± 0.78			2.15 ± 0.30		7.00 ± 0.56		9.86 ± 0.80
93131	u	WN7	0.25		1.85 ± 0.56			1.41 ± 0.32		3.74 ± 0.34		5.27 ± 0.64
94963	u	O6/O7IIIe	0.20	1.28 ± 0.67	1.61 ± 0.67			1.00 ± 0.28		2.75 ± 0.30		3.87 ± 0.43
96917	u	O8	0.37	1.87 ± 0.45	5.62 ± 0.56	2.40 ± 0.20		5.20 ± 0.45	3.31 ± 0.42	17.33 ± 1.34	23.95 ± 2.55	24.40 ± 1.90
97253	u	O5IIIe	0.50		5.60 ± 0.65	3.00 ± 1.00	2.09 ± 0.45	4.52 ± 0.42	3.60 ± 0.34	16.54 ± 1.23	23.37 ± 2.19	23.29 ± 1.75
112272	u	B1Ia/Iab	0.99		20.84 ± 1.23	16.11 ± 2.40	3.93 ± 0.56	11.23 ± 0.73	7.43 ± 0.56	39.38 ± 3.20	52.67 ± 3.70	55.45 ± 4.55
115363	u	B1Ia	0.82	5.10 ± 0.67	10.8 ± 1.20	7.20 ± 0.45	2.57 ± 0.70	9.07 ± 0.65	5.85 ± 0.42	29.82 ± 2.10	42.01 ± 3.01	41.99 ± 2.98
115842	u	B0.5Ia	0.51	3.00 ± 1.20	7.92 ± 0.87	4.89 ± 0.64	2.78 ± 0.71	6.24 ± 0.54	3.61 ± 0.32	22.34 ± 1.87	27.42 ± 2.40	31.45 ± 2.66
147165	h	B1III	0.34					1.45 ± 0.25		3.10 ± 0.10		4.36 ± 0.14
147889	h/u	B2III/IV	1.00	8.44 ± 0.87	20.23 ± 0.90	13.43 ± 1.20	7.31 ± 0.56	20.20 ± 0.30	15.10 ± 0.50	50.20 ± 1.70	100.90 ± 2.48	
147934	h	B2V	0.45				1.84 ± 0.51	5.50 ± 0.20	4.22 ± 0.30	17.86 ± 0.40	27.86 ± 1.53	25.15 ± 0.57
148184	h/u	B2Vne	0.48	3.81 ± 0.05	9.75 ± 0.75	5.88 ± 1.10	2.45 ± 0.56	7.20 ± 0.20	5.20 ± 0.20	23.70 ± 0.20	35.52 ± 1.18	
148379	u	B2Iab	0.77		7.02 ± 0.65	3.31 ± 0.56	1.35 ± 0.45	5.35 ± 0.64		16.00 ± 1.45		22.53 ± 2.06
148688	u	B1Ia	0.52	1.72 ± 0.04	5.33 ± 0.30		1.45 ± 0.54	4.01 ± 0.20	2.70 ± 0.20	14.20 ± 0.60	18.98 ± 1.18	20.00 ± 0.85
148937	u	O6e	0.61		7.07 ± 0.56	3.37 ± 0.30	2.00 ± 0.48	4.91 ± 0.60	2.81 ± 0.50	17.31 ± 0.67	21.47 ± 3.18	24.37 ± 0.95
149757	h/u	O9.5V	0.28	2.85 ± 0.65	6.41 ± 1.14	5.45 ± 1.18	1.88 ± 0.19	5.50 ± 0.20	3.60 ± 0.10	18.50 ± 1.10	25.66 ± 0.82	26.05 ± 0.14
151932	u	WN7	0.50	3.36 ± 1.13	9.58 ± 1.08		2.31 ± 0.49	7.04 ± 0.78	4.20 ± 0.45	24.75 ± 1.80	31.39 ± 3.42	
152233	h	O6III	0.42				0.91 ± 0.35	3.30 ± 0.20	1.71 ± 0.20	13.07 ± 0.20	13.80 ± 1.18	18.40 ± 0.28
152235	u	B0.7Ia	0.78	4.11 ± 0.40	11.12 ± 0.43	4.70 ± 1.20	2.75 ± 0.49	8.90 ± 0.40	6.20 ± 0.20	30.20 ± 0.70	42.85 ± 1.65	
152270	u	WC7	0.50	1.68 ± 0.45	4.35 ± 0.65	2.92 ± 0.87		3.75 ± 0.43	2.72 ± 0.45	11.55 ± 0.95	18.44 ± 2.61	16.26 ± 1.35
154811	u	O9.5Ib	0.66		7.31 ± 0.68			4.80 ± 0.34	3.56 ± 0.56	17.07 ± 1.23	23.88 ± 2.79	24.03 ± 1.75
154873	u	B1Ib	0.47		6.02 ± 0.65			3.60 ± 0.43		13.20 ± 0.97		18.58 ± 1.38
156385	u	WC7	0.34		1.72 ± 0.56			1.65 ± 0.28		5.33 ± 0.43		7.50 ± 0.61
156575	u	B1Ib/II	0.40	1.90 ± 0.57	3.51 ± 1.32			3.70 ± 0.56		11.08 ± 0.60		15.60 ± 0.85
157038	u	B4Ia	0.92		6.76 ± 0.87			4.21 ± 0.37		15.73 ± 0.56		22.15 ± 0.85
163800	h/u	O7	0.57	3.18 ± 0.89	7.77 ± 0.82	4.87 ± 0.98	2.35 ± 0.39	7.10 ± 0.30	4.84 ± 0.40	22.20 ± 0.20	33.81 ± 0.24	
164794	u	O4V	0.33		3.11 ± 0.51			2.21 ± 0.54	1.83 ± 0.34	6.98 ± 0.47	11.67 ± 2.47	9.83 ± 0.67
169454	u	B1Ia	1.10	3.81 ± 0.45	10.27 ± 0.38	2.85 ± 0.45		8.51 ± 0.54	6.23 ± 0.43	27.45 ± 1.87	42.05 ± 2.29	
170235	u	B2Vnne	0.29		3.15 ± 1.23			2.33 ± 0.56	1.33 ± 0.70	6.89 ± 0.45	10.18 ± 3.80	9.70 ± 0.64
171432	u	B1/B2Iab	0.43		3.79 ± 1.10			3.30 ± 0.34	2.04 ± 0.45	11.56 ± 0.56	14.97 ± 2.39	16.28 ± 0.80
179406	h/u	B3V	0.31	2.57 ± 0.36	6.01 ± 0.45	4.09 ± 0.56	1.55 ± 0.36	4.18 ± 0.34	2.81 ± 0.10	14.10 ± 1.70	19.76 ± 1.15	19.85 ± 2.42
202214	t	B0V	0.34					3.55 ± 0.85		11.29 ± 1.30		15.90 ± 1.85
203064	t	O8V	0.25					2.30 ± 0.56	1.23 ± 0.56	7.61 ± 1.10	9.75 ± 3.30	10.71 ± 1.56
205139	t	B1II	0.34					4.17 ± 0.54		12.36 ± 1.40		17.40 ± 2.00
206165	t	B2Ib	0.46					5.10 ± 0.43	3.14 ± 0.34	20.12 ± 1.56	23.09 ± 2.21	27.82 ± 2.22
206267	t	O6	0.49					5.97 ± 0.80	3.5 ± 0.80	21.24 ± 1.67	26.40 ± 4.71	29.90 ± 2.37
207198	t	O9II	0.55					10.12 ± 1.34	6.06 ± 0.70	28.67 ± 2.04	45.21 ± 5.62	40.37 ± 2.90
207538	b	B0V	0.59					8.76 ± 0.89	6.71 ± 0.56	30.36 ± 1.78	44.34 ± 4.07	
208501	b	B8Ib	0.77					11.90 ± 0.65	7.92 ± 0.80	37.89 ± 2.21	56.62 ± 4.36	
210839	t	O6e	0.56					7.20 ± 0.56		21.39 ± 1.89		

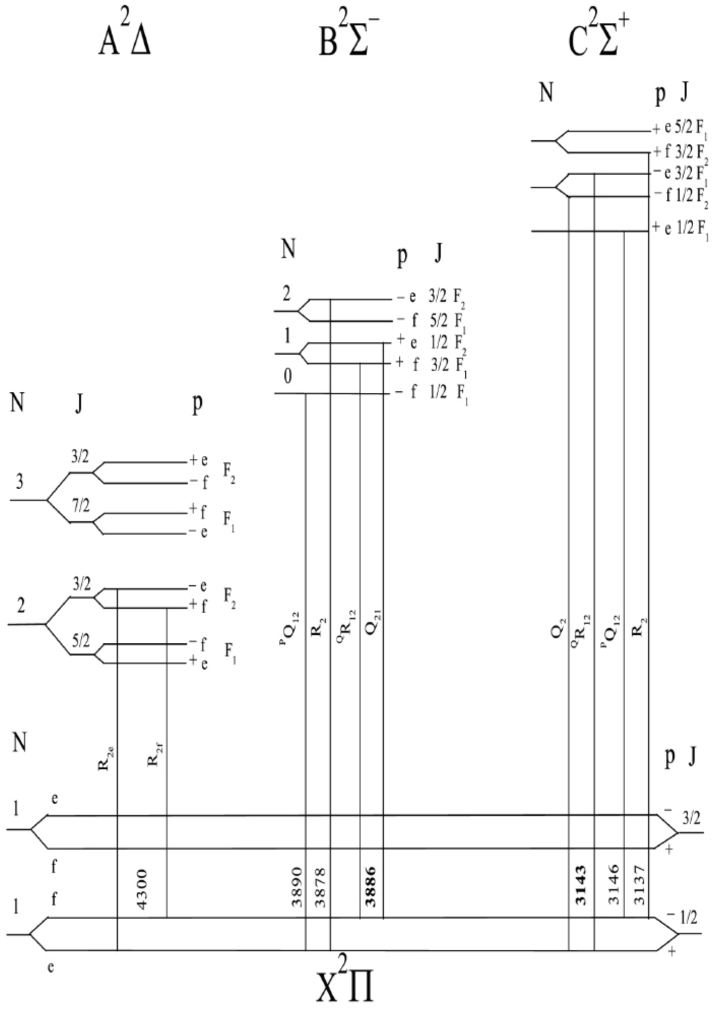

FIGURE 5.1: Term structure of the lowest three rotational levels of the $A^2\Delta$, $B^2\Sigma^-$, and $C^2\Sigma^+$ electronic systems of CH molecule. With bold line we indicate 3886 and 3143 lines which are observed as unresolvable blend.

5.3 Results and Discussion

In Figure 5.1 we present the term structure of the lowest three rotational levels of the $A^2\Delta$, $B^2\Sigma^-$, and $C^2\Sigma^+$ electronic systems of CH molecule. The dipole-permitted transitions from the J = 1/2 level of the $X^2\Pi$ ground state to the $A^2\Delta$ state is well seen as a blend 4300.3132 Å separated by 1.43 km/s (Lien 1984). In Figure 5.1 we also mark four possible transitions from the $X^2\Pi$ ground state for $B^2\Sigma^-$, and $C^2\Sigma^+$ electronic systems: two of the lines (3886 and 3143 Å) are blended with separations 1.28 and 2.17 km/s, respectively.

To obtain column density we used the relation of van Dishoeck & Black (1989) which gives proper column densities when the observed lines are unsaturated:

$$N = 1.13 \times 10^{20} W_\lambda/(\lambda^2 f), \tag{5.1}$$

where W$_\lambda$ and λ are in Å and column density in cm^{-2}.

The intensity ratio of two unsaturated spectral lines is equal to:

$$\frac{W_{\lambda_1}}{W_{\lambda_2}} = \frac{f_1}{f_2}\frac{\lambda_1^2}{\lambda_2^2} = \frac{q_1}{q_2}\frac{\lambda_1}{\lambda_2} \tag{5.2}$$

where $W_{\lambda_1}, W_{\lambda_2}$ are equivalent widths; f_1, f_2 oscillator strengths (f-values), q_1, q_2 Franck-Condon (F–C) factors, and λ_1, λ_2 wavelengths of the lines under consideration.

Equation (2) describes the ratio of equivalent widths of two different lines of the same molecule in relation to their wavelengths and the Franck-Condon factors and is true if and only if (a) the lines arise in the same lower state, (b) the lines are the same branch in both bands, and (c) the dipole moment function is constant. For more information see Larsson (1983).

A major problem in the analysis of interstellar CH is the transformation from the band oscillator strength to the line oscillator strength of an individual line. In the case of CH molecule the relation between the line (f$_J$) and the band (f$_{\nu'\nu''}$) oscillator strength is

$$f_J = \frac{S_J}{(2-\delta_{0,\Lambda'+\Lambda''})(2J''+1)} f_{\nu'\nu''} \tag{5.3}$$

where S$_J$ is the line strength or Hönl-London factor and Λ', Λ'' are the projections of the electronic angular momentum on the internuclear axis of the upper and electronic systems (see Schadee 1975, as a review). Line strengths have been tabulated by Tatum (1967) and recently by Lien (1984).

In the case of spectra with no Doppler split it was possible to improve line positions basing on the fact that our spectra from HARPS and UVES instruments are of high resolution and offer a high wavelength precision. In the case of objects obtained with HARPS instrument the error of wavelength measurement does not exceed the value of 0.001 Å (radial velocity accuracy is not higher than 30m/s in the case of one Doppler component – see HARPS user manual). In case of UVES spectra error in wavelength precision does not exceed 50m/s – see UVES user manual.

In each case our wavelength scale was shifted to the rest-wavelength velocity frame using CH A–X line at 4300.3132 Å (Gredel et al. 1993). For this procedure we used objects obscured by one cloud, in case of which CH A–X line was narrow and no Doppler-splitted (i.e. HD 76341, 147889, 148184, and 163800). Results are presented in Table 5.3. We confirm positions of B-X bands presented in the publication of Gredel et al. (1993). However in the case of 3137 and 3143 lines of CH C-X transition our values are different from those of Herbig (1968) and Lien (1984). In the case of 3146 line our result is consistent with that of Lien (1984).

In Figure 5.2 we present the 4300, 3886 and 3890 Å lines of CH molecule in the spectrum of HD 147889. It is to be emphasized that CH 4300 and 3886 Å lines are saturated (their equivalent widths exceed the value of 20 mÅ- van Dishoeck & Black

TABLE 5.3: New positions of CH C–X molecular features compared to those of Herbig (1968) and Lien (1984) (^{a} - air wavelength).

HD	3137	3143	3146
76341	3137.558	3143.166	
147889	3137.558	3143.163	3145.998
148184	3137.560	3143.166	3145.995
163800	3137.557	3143.164	
This work position	3137.5582	3143.1647	3145.9965
Error	0.0013	0.0015	0.0021
Herbig (1968)	3137.53	3143.15	3146.01
Lien (1984)	3137.576	3143.183^a	3145.996

TABLE 5.4: Oscillator strengths obtained in this work (with errors). Recently published values are of ^{a} – Larsson & Siegbahn (1983), ^{b} – Lien (1984).

Wavelength Å	Line	Recent f-value [10^{-5}]	This work f-value [10^{-5}]
4300.3132	$R_{2e}+R_{2f}$	506^a	434±31
3890.217	$^PQ_{12}$	210^b	210
3886.409	$^QR_{12}+Q_{12}$	320^b	320
3878.774	R_2	110^b	110
3145.9965	$^PQ_{12}$	430^b	415±30
3143.1647	$Q_2+{}^QR_{12}$	640^b	640
3137.5582	R_2	210^b	267±17

(1989). This effect is well seen in Figure 5.2, where the relation between measured strengths of 4300 and 3886 lines is presented (the strength ratio of 3886 to 4300 gets higher than while there is no saturation). The latter is really not seen when W(4300) does not exceed 20 mÅ.

Figure 3 presents CH B-X and C-X bands in the UVES spectrum of HD 148184. The B-X transition was first measured by Adams in spectrum of ζ Oph (McKellar 1940b). Both B–X and C–X bands have been observed by Herbig (1968) also in the case of HD 149757. Several publications of Chaffee & Lutz (1977); Danks et al. (1984); Cardelli & Wallerstein (1986) present these bands. Our results shown in Table 5.2 confirm previous results concerning A–X and B–X band (for HD 148184 we obtain 23.70, 7.20 and 5.20 mÅ in the case of 4300, 3886 and 3890 bands compared to 23.0, 6.1 and 4.4 in the publication of Danks et al. (1984). Also in the case of HD 149757 we obtain 18.50, 5.50 and 3.60 compared to 17.8, 5.0 and 3.3 in the latter publication. The spectra of Danks, Federman and Lambert, acquired using the ESO/CES instrument, are of the comparable spectral resolution to those presented in this paper.

A difference exists when we compare our results in the case of HD 147889 with those of Cardelli & Wallerstein (1986). We obtain 50.20, 20.20 and 15.10 in the case of 4300, 3886 and 3890 bands compared to 51.0, 15.6, and 9.4. It is to be emphasized that our spectra from HARPS spectrograph are of higher resolution than those of Cardelli and Wallerstein. Also - we could make our measurements in both: HARPS and UVES spectra. It was also possible to compare results of Herbig (1968) concerning C-X band of CH molecule observed toward HD 149757 (5.0, 7.4 and 4.0 in case of 3146, 3143 and 3137 lines) with our result seen in Table 5.2 – 5.45, 6.41 and 2.85, respectively.

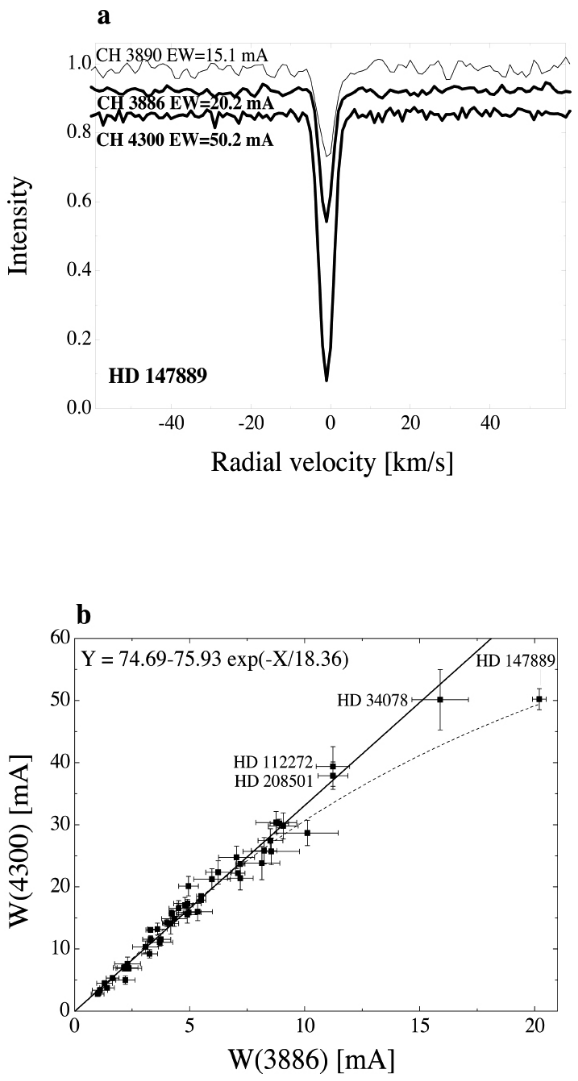

Figure 5.2: The CH A-X and B-X systems at 4300, 3886 and 3890 Å seen in the spectrum of HD 147889 from HARPS instrument in the radial velocity scale (a). Bands at 4300 and 3886 Å are saturated (bold line). At the bottom (b) we present correlation plot between equivalent widths of the bands at 4300 and 3886 Å. The stronger 4300 Å band saturates at the level of 20 mÅ. With dotted line we depict exponential fit to data-points. With solid line we present relation based on data-points which are unsaturated (W(4300)<20 mÅ).

In Figure 5.4 we compare our measurements with those already published, based on high-resolution spectra (i.e. of resolution comparable or higher than that of our spectra – Crane et al. (1995); Pan et al. (2004); Weselak et al. (2008b). It is well seen that our results are consistent with the latter (the correlation coefficients are equal to 0.98 and 0.99 for A–X and B–X bands respectively).

In Figure 5.5 we present the relation between equivalent widths of CH A–X band near 4300 Å and the two other bands: 3886 Å B–X and C-X band at 3143 Å. To avoid saturation effects we excluded the data-points for which equivalent widths exceed

20 mÅ (van Dishoeck & Black 1989, see also Fig. 2). This restriction was applied in all cases of correlation plots presented in this paper).

Our spectra are of not high enough resolution to measure directly the Doppler broadening parameter (to do that the spectral resolution should be of the order of 500,000). This is why we restricted our considerations to non-saturated features.

If the above condition is fulfilled the equivalent width ratio of A-X 4300 Å and CH B-X 3886 Å band should be equal to 3.87 (based on oscillator strengths equal to 506 and 320×10^{-5} from publications of Larsson & Siegbahn (1983) and Lien (1984), respectively). Similarly, the ratio of equivalent widths of A–X and C–X band at 3143 Å (while the oscillator strength equal to 640×10^{-5} is applied to the latter) should be equal to 2.96.

However, as seen in Figure 5.5, in the case of relation between strengths of 4300 and 3886 bands most of data-points are found under the theoretical line and this ratio is equal to 3.32±0.04 instead of 3.87. The equivalent width ratio of 4300 and 3143 bands is also lower from the theoretical value (2.96) and equal to 2.53±0.07. It is to be emphasized, that these results are based on high-resolution spectra for spectral features free of saturation effects .

To check the precision of the applied method we present (in Figure 5.6) the relations between equivalent widths of 3886 Å and 3890 Å transitions belonging to the CH B–X band. As it is seen in Fig. 6a this ratio is close to the theoretical value (1.50). It is also well seen in Figure 5.6 that the observed intensity ratio of 3886 CH B-X and 3143 C–X transitions is close to that predicted by their published f-values – 0.76 (Table 5.4). This result is consistent with the thesis of Lien (1984) that f-values in the case of CH B–X system are correct. Based on this we can obtain the correct f-value of CH A-X transition which should be equal to $434\pm31\times10^{-5}$. It is to be emphasized that this result is based on two different relations which were based on two B–X and C–X bands of CH molecule.

To test f-values of CH C-X band centered near 3143 Å we can assume that f-value of CH C-X line at 3143 Å is correct (the relation between intensities of 3886 and 3143 bands suggests that f-value of 3143 transition is correct). The relation between equivalent widths of 3143 and 3137 bands of CH C-X transition leads to the value presented in Table 3, which should be equal to $267\pm17\times10^{-5}$ in the case of 3137 band. Our result concerning the 3146 Å line ($415\pm30\times10^{-5}$) is close to the value published previously in the literature – see Table 5.3.

Finally, in Figure 5.7 we present the relation between column density of CH molecule derived from B-X bands at 3886 and 3890 Å and that obtained from unsaturated 4300 band with the new oscillator strength equal to $434\pm31\times10^{-5}$. The relation, of the correlation coefficient equal to 0.98, confirms clearly the proposed oscillator strength value.

It is to be emphasized that our result concerning new f-value of CH A-X transition at 4300 Å is consistent with the laboratory value of Linevsky (1967), who determined the f-value ratio between 3860 and 4300 lines of CH as equal to 0.61±0.10. If we assume (it is true on the basis of our observations) that f-value of 3886 line is equal to 320×10^{-5} the value of the latter should be between 450 and 627×10^{-5}. Our result

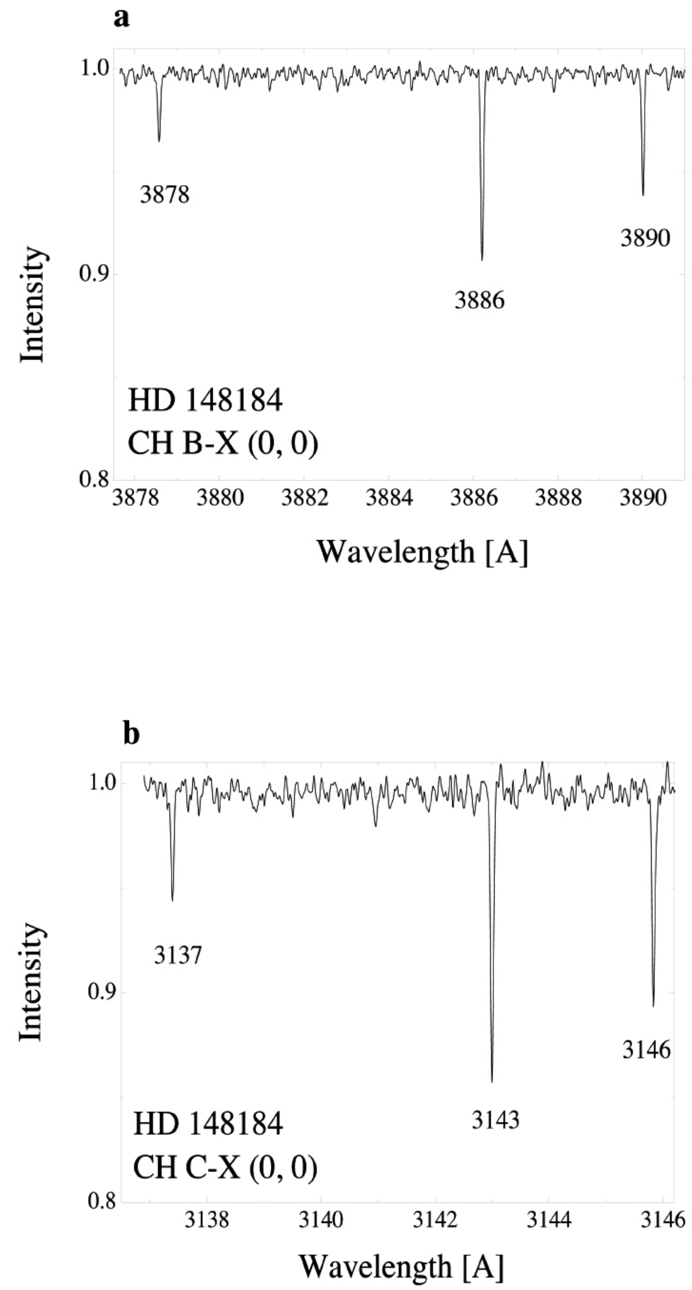

Figure 5.3: The CH B-X and C-X systems centered near 3886 Å (a) and 3143 Å (b) seen in the spectrum of HD 148184 from UVES instrument in wavelength scale. Note the same intensity ratio of 3886 to 3890 and 3143 to 3146 which should be equal to 1.50 if bands are unsaturated.

($434 \pm 31 \times 10^{-5}$) is consistent with the latter.

It is difficult to understand the difference between the new f-value of C-X transition at 3137 Å and the formerly published one since no errors are published in the literature. It is to be emphasized that our result is based on the statistically meaningful sample of stars in spectra of which saturation effects are absent.

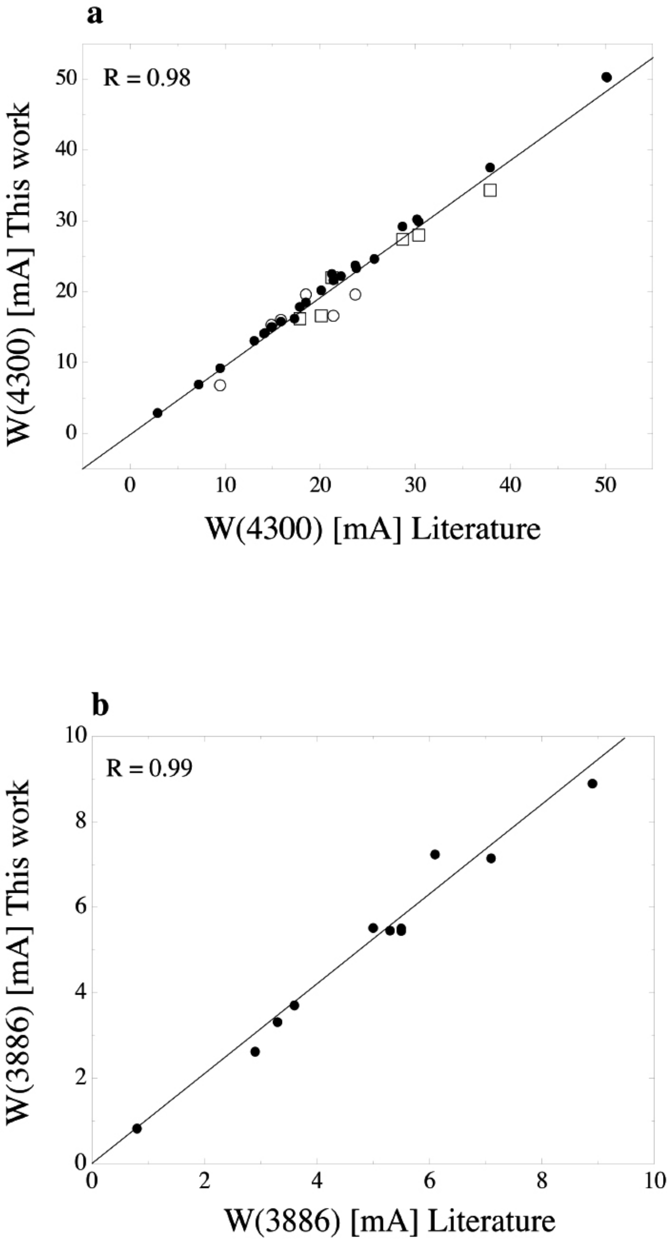

Figure 5.4: Comparison of our measurements with those from the literature in the case of CH A-X band at 4300 Å (a) B-X band at 3886 Å (b). With open circles we mark results of Crane et al. (1995), open squares – Pan et al. (2004) and filled dots – Weselak et al. (2008b). In each case the relation is very good with correlation coefficient equal to 0.98 and 0.99, respectively.

5.4 Conclusions

The above considerations led us to infer the following conclusions:

1. the statistically meaningful sample of high resolution, high S/N ratio spectra allowed to make the new estimate of the oscillator strength of CH A–X transition equal to $434\pm31\times10^{-5}$ which is consistent with the oscillator strengths of the other bands of CH.

2. we obtained new f-values of CH C-X transition at 3145 and 3137 Å equal to 415 ± 30 and $267\pm17\times10^{-5}$, respectively.

The system of f-values, proposed here for the transitions of the A–X, B–X and C–X bands of methylidyne is self-consistent: the column densities, calculated from W_λs of unsaturated transitions coincide within a small error limit. It is of importance to collect precise f-values based on observational material and compare them to experimental and theoretical results. More efforts in this area is to be done in the case of known visible transitions of diatomic molecules. It is certainly important to collect more spectra of the high signal-to-noise ratio to obtain correct f-values in the case of observable transitions. This procedure should allow to adjust column densities of all known molecules toward observed targets.

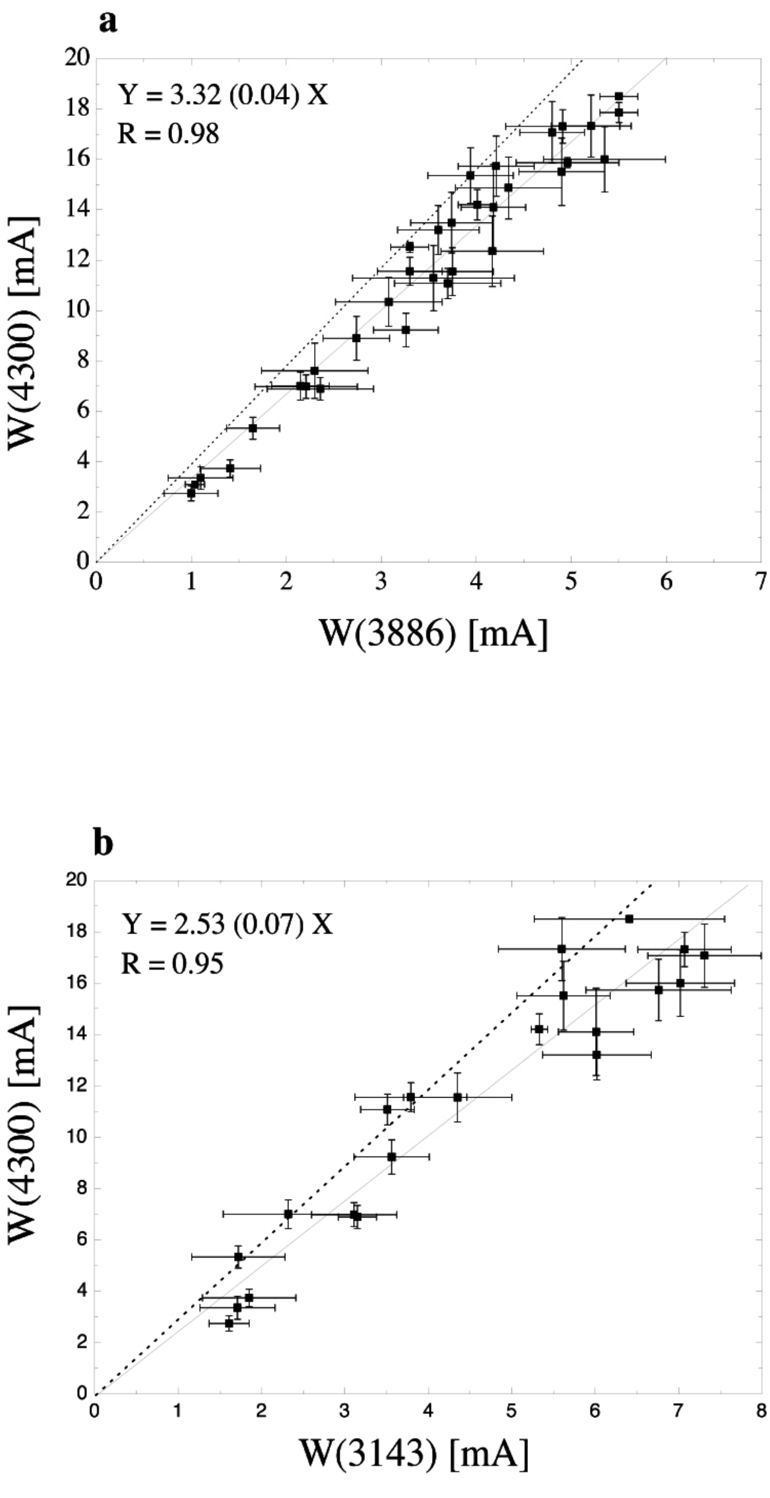

Figure 5.5: Correlation patterns between equivalent widths of CH A-X band at 4300Å and 3886 (a) and between strengths of 4300 band and 3143 (b). In each case dotted line represents the equivalent width ratio calculated in the absence of saturation using the oscillator strengths recently published in the literature (Table 5.4). Solid line is the fit to data-points.

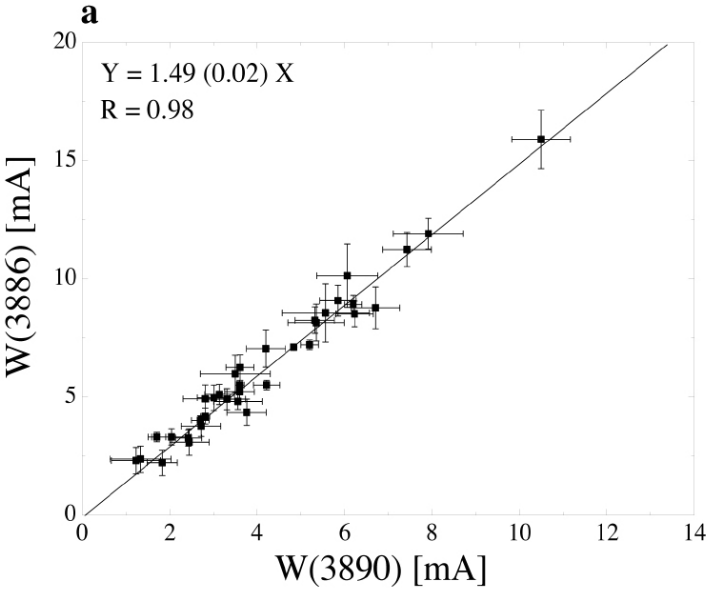

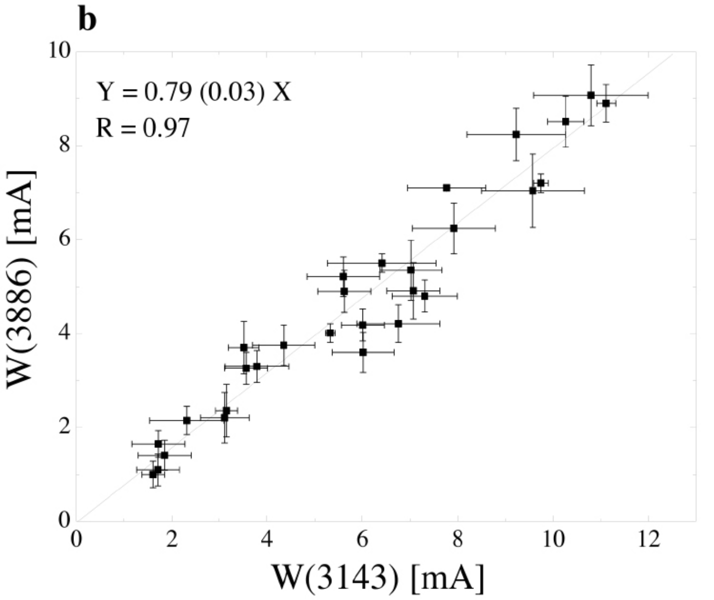

FIGURE 5.6: Correlation plots between equivalent widths of CH B-X band at 3886 Å and 3890 band (a), and between strengths of 3886 band and 3143 (b). In each case the equivalent width ratios are close to those obtained on the basis of f-values recently published in the literature (1.50 and 0.76, respectively).

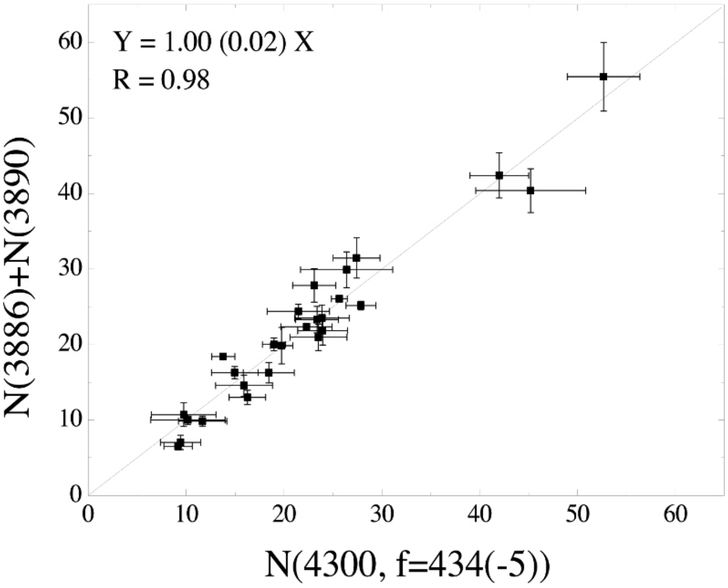

Figure 5.7: The relation between column density of CH molecule derived from B-X bands at 3886 and 3890 Å and abundance obtained from unsaturated 4300 band with new oscillator strength equal to 434×10^{-5}. Note the correlation coefficient equal to 0.98.

6

Spatial correlations of some DIBs and simple molecules

submitted to Astronomy & Astrophysics

Weselak, T, Beletsky, Y., Galazutdinov, G., LoCurto, G., and Krełowski, J.

Abstract

Radial velocities of CH, CH^+ features and two narrow diffuse interstellar bands: 6196 and 4964 suggest that 6196 DIB carrier is spatially correlated with CH^+ while 4964 DIB carrier prefers environments where CH molecule is abundant. The analysis of correlations between CH and CH^+ column densities and DIB strengths in a statistically meaningful sample of 83 reddened OB stars clearly confirms this suggestion. It is thus emphasized that a future identification of DIB carriers requires analyzes of environments in which they do exist.

6.1 Introduction

Diffuse interstellar bands (DIBs) are numerous narrow to broad absorption features mostly found in the visual to near infrared (4000-10 000Å) spectra of early type OB – stars. Despite significant observational efforts (Galazutdinov et al. 2000; Weselak et al. 2000; Hobbs et al. 2008, and references therein) DIBs remain one of the long standing puzzles in stellar spectroscopy. Since their discovery (Heger 1922) not a single DIB carrier has been identified yet, although many possible candidates have been proposed (Herbig 1995).

The molecular origin of at least some DIBs seems probable as some of the bands are complex and reminiscent of rotational structure in molecules (Sarre et al. 1995; Kerr et al. 1998). The 6614 DIB has been found to have three main components that have the appearance of unresolved P, Q and R branches of an electronic transition of a large molecule. Also good correlations with CH molecule in the case of narrow 5797 DIB (Weselak et al. 2008b) agree with thesis that carriers of DIBs are molecules.

The methylidyne (CH) molecule, which was identified by McKellar (1940a), is closely related to molecular hydrogen (H_2) as already shown by Mattila (1986) and Weselak et al. (2004). On the other hand, column densities of CH^+ and H_2 show large scatter indicating no relation between abundances of these two molecules (Gredel 1997; Weselak et al. 2008b). Formation and existence of CH cation in the ISM remains an unsolved problem (van Dishoeck & Black 1989; Gredel et al. 1993; Sheffer et al. 2008, and references therein).

Spectral observations of highly-reddened early type stars offer an excellent opportunity to probe large column densities of gas along the line of site, derive parameters of the environmental conditions and eventually unveil nature of the DIB carriers.

The aim of this work is to present relations between abundances of simple diatomic molecules as CH, CH^+ and CN and intensities of two narrow DIBs at 4964 and 6196 Å. It is important to specify the environments in which DIB carriers exist. It may shed some light on the conditions which facilitate formation/preservation of DIB carriers. The paths of CH and CH^+ formation are different (Federman 1982) which makes interesting to relate some DIBs to either CH or CH^+.

6.2 The observational data

The spectra of 6 objects listed in Table 6.1 were obtained using UVES spectrograph (u) at ESO Paranal in Chile with the resolution R = 80,000. The spectrum covers the spectral range from 3,040 to 10,400 Å. It was acquired as a part of the "Library of High-Resolution Spectra of Stars across the Hertzsbrung-Russell Diagram" and are available at the website: http://www.sc.eso.org/santiago/uvespop. For more information see Bagnulo et al. (2003).

All the spectra were reduced using MIDAS and IRAF, as well as our own DECH code (Galazutdinov 1992), which provides all standard procedures of image and spectra processing. Using different software data reduction packages allows us to get better control over proper dark subtraction, flat-fielding, or excision of cosmic ray removal and minimize possible systematic errors. We measured the equivalent widths of selected features in the spectra Gaussian.... Some of our targets have been observed several times, which facilitates an error estimate. We calculated column density of CH cation as it was done in the publication of Weselak et al. (2008b) in case of unsaturated features with oscillator strength (f-value) of 4232 Å band equal to 0.00545, which was taken from Larsson & Siegbahn (1983). The recently obtained f-value of 3957 Å band equal to 0.00342 (Weselak et al. in press) was used to calculate column density of CH^+ molecule when 4232 Å band was saturated.

6.3 Results

For this project we selected a sample of 83 reddened OB stars, which have both CH and CH^+ features is their spectra. Spectra of the two objects HD 20041 and HD 21291 (obtained by Weselak et al. (2008c) were excluded from our analysis due to poor data quality in the vicinity of the CH^+ feature. At the same time we added a UVES spectra of HD 151932.

Table 6.1 presents the HD number, spectral type, and luminosity class, as well as the E(B-V)– color excess for each star, equivalent widths (in mÅ) of CH^+ features at 3957 and 4232 Å, calculated column densities (in 10^{12} cm^{-2}) of CH^+, and EWs of diffuse 4964 and 6196 bands with errors in each bracket.

In Figure 6.1 we present the CH and CH^+ features in HARPS spectrum of HD 147889 in radial velocity scale. At the bottom of this figure we also present two narrow DIBs at 4963.85 and 6195.97 Å (Jenniskens & Desert 1994; Herbig 1975, respectively) with positions in the spectrum of HD 23180 as taken from the survey of Galazutdinov et al. (2000). In the vicinity of 6196 DIB a weak feature at 6194.76 Å is presented.

HD 147889 is highly reddened object with no Doppler spitting observed, in case of which saturation effects in both CH A-X and CH^+ A-X features are clearly visible and saturated (equivalent width of both features is greater than 20 mÅ in Figure 6.1). In this case B-X features of CH (centered near 3886 and 3890 Å) and CH cation (near 3957 Å) should be used to derive column density and avoid any saturation effects (Weselak et al. 2008b,c).

In Figure 6.2 we present a comparison of our measurements of CH cation (4332Å) and two narrow 4964 and 6196 DIBs with the results of Crane et al. (1995); Pan et al. (2004) and Thorburn et al. (2003) respectively. In both cases the agreement is very good (the correlation coefficients are 0.96, 0.99 and 0.99, respectively). Only for the CH cation feature in HD 208501 the corresponding linear relation does not hold well.

It is well known that CH cation needs different interstellar conditions than CH to be formed (Federman 1982). In many cases CH^+ features are Doppler-splitted while Doppler components in CH features are not seen (see Pan et al. 2004). However, there are also lines of sight where we observe splitting in both CH and CH^+ bands. In Figure 6.3 we present spectra of HD 151932 and 152233 in the vicinity of CH and CH^+ at 4300 and 4232 Å in radial velocity scale. At the bottom of this figure we also present spectral region of 4964 and 6196 DIBs in the same scale. Intrinsic DIB wavelengths were determined using the rest wavelength velocity frame based on KI (7698.974 Å) line

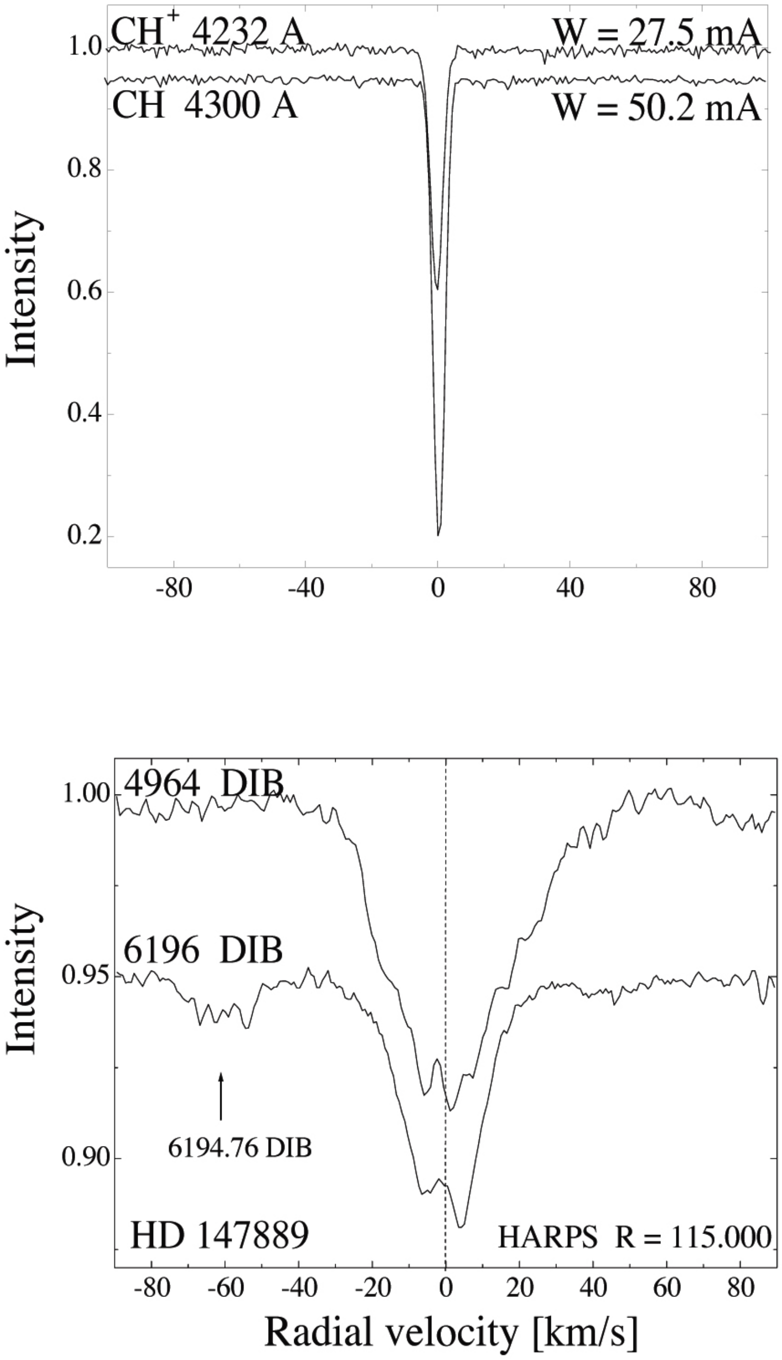

Figure 6.1: The CH A-X and CH$^+$ A-X bands centered near 4300 and 4232 Å seen in spectrum of HD 147889 in the radial velocity scale (top panel). At the bottom we present DIBs at 4963.85 and 6195.97 Å (Galazutdinov et al. 2000) in the same radial velocity scale. Weak DIB at 6194.76 Å is also seen in spectrum of this star.

(Galazutdinov et al. 2000). This method allows to measure radial velocities of profiles and in case of narrow interstellar features gives very low uncertainty smaller than 0.3

km/s. In case of DIBs, which are broader (see Figure 6.1) the precision of radial velocity measurement is not larger than 1-2 km/s. It is evident that in both cases the 6196 DIB shares the radial velocity with the CH cation component (-7.6±0.4 and -7.0±1.2 km/s in the case of HD 152233, and -6.1±0.2 and -7.0±1.0 km/s in the case of HD 151932, respectively) while the 4964 DIB – with the neutral methylidyne. Figure 6.3 illustrates this effect using the spectra where radial velocities of CH and CH^+ features are evidently different. To check the effect using a statistically meaningful sample we also examined relations between column densities of molecular features and intensities of the two narrow DIBs based on an extensive sample of objects from our database.

Figure 6.4 shows the relation between column densities of CH and CH cation and equivalent widths of 4964 and 6196 DIBs. In each case we highlight a group of 10 objects with high abundance of CH which missed the relation between column density of CH molecule and 5780, 5797 DIBs (Weselak et al. 2008c) – "CH abundant clouds". It is evident that the 4964 DIB correlates more tightly with the column density of CH while the 6196 DIB – with the abundance of CH^+. This result proves that the carriers of 4964 DIB occupy the same regions of translucent clouds as neutral methylidyne and that carriers of 6196 DIB likely share the environments with the CH^+ molecule. It is to be emphasized that if we omit "CH abundant clouds", the 6196 DIB is well correlated with column densities of both CH and CH^+ (with correlation coefficients equal to 0.85 and 0.79, respectively).

We also examined relations between intensities of both 4964 and 6196 DIBs and E(B-V) (Figure 6.5). In each case the relation is pretty tight with correlation coefficient equal to 0.80 and 0.89, respectively. However, it is well seen that objects with high abundance of CH molecule miss the relation in case of 6196 DIB. A similar effect was found in the case of 5780 and 5797 DIBs when the equivalent widths, published previously (Weselak et al. 2008c), were applied, i.e. clouds with high abundance of CH also miss the main stream of the relation in the case of 5780 DIB.

We also compared correlation coefficients of the relations between column densities of CH^+, CH and CN molecules, equivalent widths of 4964, 6196, 5780, 5797 DIBs and E(B-V)'s – given in Table 6.2 (The column densities of CH and CN molecules as well as strengths of the major 5780 and 5797 DIBs are taken from the publication of (Weselak et al. 2008c). It is evident that column densities of CH and CH^+ correlate better with E(B-V) than with CN molecule does (the correlation coefficients are equal to 0.72, 0.79 and 0.41, respectively). It is also seen that the strength of 5780 DIB correlates very tightly with that of the 6196 DIB (correlation coefficient 0.97), while 5797 is well correlated with 4964 DIB (correlation coefficient 0.83). This result suggests that 5780 occupy the same region of diffuse cloud as CH^+ (and also 6196 DIB), while 5797 DIB (as well as 4964) carrier resides in the regions where CH molecule (closely related to H_2 as it was demonstrated already (Weselak et al. 2004, 2008c) dominates. Each of the DIBs presented in Table 6.2 is well correlated with E(B-V) which makes this parameter quite useless while trying to predict strengths of many interstellar features.

Most researchers consider diffuse bands as arising from a set of carbon-based absorbers with size between dust grains (which cause visual extinction) and the large carbon–bearing molecules. Carriers of narrow DIBs are relatively abundant in media in which the energetic UV photons are scarce. In such environments dust grains effectively catalyze the formation of DIB carriers. The question arises whether CH in environments rich in DIB carriers originates as a result of DIB carriers disruption or not. An answer to this question is connected with the role of objects where an excessively high abundance of CH in relation to intensities of narrow DIBs, such as 4964 or 6196, is observed. These objects clearly worsen the relations presented in Figure 6.4. The same objects apparently deteriorate also the relation of CH to E(B-V) – see Figure 6.1 (5b and 5c). However, in average CH and CH^+ molecules are rather well correlated with E(B-V) – correlation coefficient equal to 0.72 and 0.79, respectively. This result is different from that presented by Krełowski et al. (1999) (0.86, and 0.82, respectively). Our result is surprising as it was based on more numerous sample of objects. However, in the work of Krełowski et al. (1999) one object, HD 169454, which misses the relation between equivalent width of CH^+ and E(B-V) was taken into account (not in our data sample). As a result the correlation coefficient of the relation between equivalent width of CH and E(B-V) is higher than in the case of CH^+.

Finally, in Figure 6.6 we present the relation between column densities derived from both CH^+ bands at 4232 and 3957 Å (presented in Table 6.1) and based on f-values presented in the publication by Weselak et al. (in press). It is well seen that column density obtained on the basis of 4232 Å band which was saturated may be underestimated by a factor of 4 %. To properly estimate saturation effects seen in Doppler–splitted components one should use high–resolution spectra as those of Sarre et al. (1995) or Kerr et al. (1998). Our spectra presented in this paper are not of this quality.

6.4 Conclusions

The above considerations led us to infer following conclusions:

1. The 6196 DIB carrier is spatially correlated with CH^+ while 4964 DIB carrier prefers environments where CH molecule is abundant. This conclusion follows analyzes of both: radial velocities of the considered features and correlations of their strengths.

2. Each of the presented diffuse bands is pretty tightly correlated with E(B-V). CH and CH^+ molecules are also rather well correlated with E(B-V) – correlation coefficients equal to 0.72 and 0.79, respectively. Additionally the major 5780 DIB is well correlated with 6196 one with the correlation coefficient 0.97.

3. We find specific environments with high abundance of CH molecule in relation to narrow 4964, 6196 DIB intensities (CH abundant clouds), i.e. HD 24534, 27778, 34078, 147889, 148184, 149757, 152235, 154368, 204827 and 208501. In this group we also found one object – HD 34078, characterized by very high abundance of both CH and CH^+ in relation to E(B-V) (CH&CH^+ abundant cloud). There are also objects with high abundance of CH and CN molecules in relation to E(B-V) (CH&CN abundant clouds), i.e. HD 27778, 147889, 154368, 204827, 208501.

The good correlation of the CH^+ with 6196 DIB and CH molecule with 4964 DIB likely extends to other DIBs. It would be very interesting to check the relations between column densities of other molecular features such as C_2, or CO and the strengths of strong DIBs, based on new samples of homogeneous measurements. It is certainly important to collect more spectra of the high signal-to-noise ratio to obtain correct values of column densities of simple molecules and check how far they are related to diffuse interstellar band carriers. In any case it seems to be of basic importance to relate the origin of diffuse bands to specific environments of physical parameters available from analyzes of identified atomic and/or molecular features.

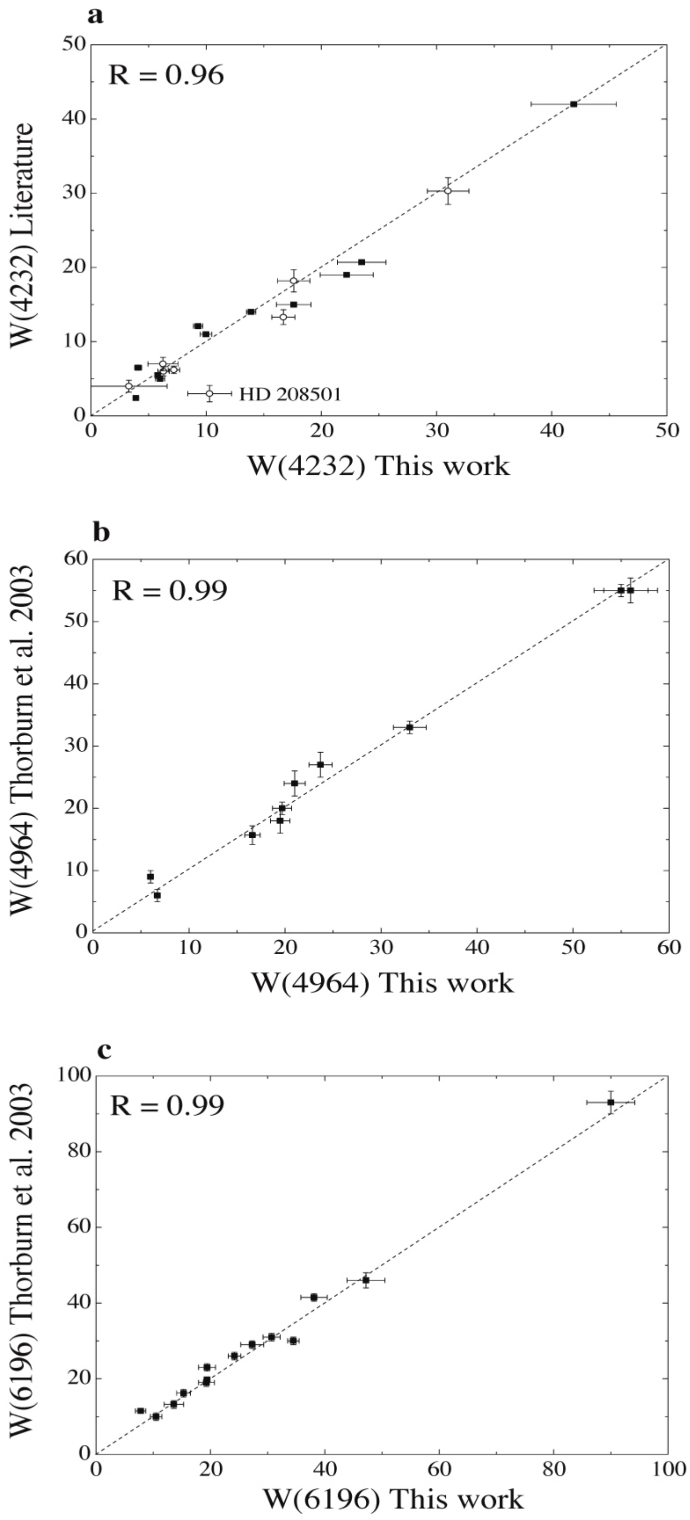

FIGURE 6.2: Our measurements of equivalent widths of CH^+ A-X feature at 4232.548 Å compared with those of Crane et al. (1995) – filled circles and Pan et al. (2004) – open circles (a). In the center and at the bottom we compare our measurements of equivalent widths of 4964 and 6196 DIB with those of Thorburn et al. (2003). In each case the relation is good with correlation coefficient equal to 0.96, 0.99 and 0.99, respectively.

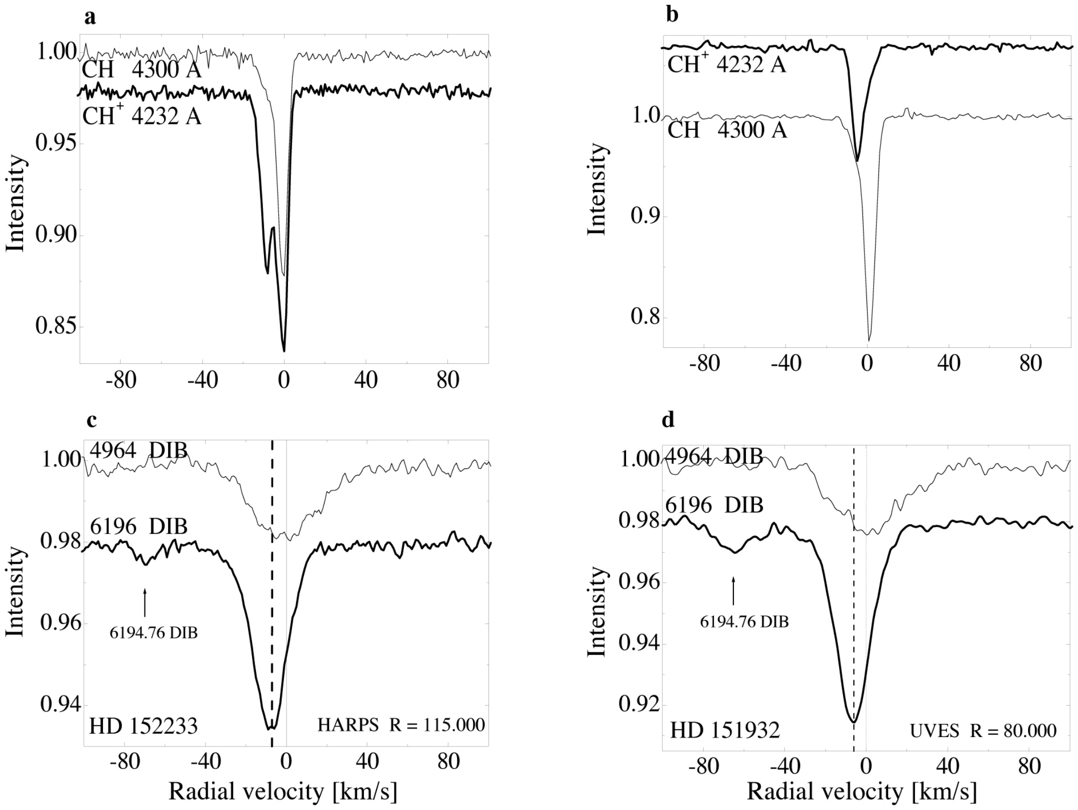

FIGURE 6.3: Comparison of the CH A-X and CH^+ A-X bands (top panels) with the 4964 and 6196 DIBs in the same radial velocity scale (bottom) in spectra of HD 152233 and 151932. The CH^+ component with the same radial velocity as 6916 DIB (bold line) and CH component with the same radial velocity as 4964 DIB is clearly seen. We also mark position of weak DIB at 6194.76 Å in each case.

TABLE 6.1: Observational and measurement data. Given are: star name (observed at b – Bohyunsan (S. Korea), h – HARPS (ESO), f – FEROS (ESO), t - Terskol (Russia), u - UVES (ESO) spectral and luminosity class, reddening, equivalent widths of CH$^+$ 3957 and 4232 Å features (in mÅ), calculated column density of CH$^+$ (in 10^{12} cm^{-2}) and equivalent widths of 4964 and 6196 DIBs (in mÅ). **With subscript x we mark lines of sight in case of which column density of CH cation were obtained on the basis of unsaturated 3957 band with f-value equal to 0.00342 – see text.** In columns Lit we present data from literature: in case of 4232 band of CH$^+$ those taken from c – Crane et al. (1995), p – Pan et al. (2004). In the case of 4964 and 6196 DIBs published data were taken from Thorburn et al. (2003). Column density of CH molecule in case of HD 151932 not presented in the publication of Weselak et al. (2008c) is equal to 32.65±3.42 (based on equivalent width of unsaturated 3957 feature equal to 7.96±0.78; column density of CN molecule is equal to 2.58±0.33 10^{12} cm^{-2} (based on unsaturated R(0) which equivalent width is equal to 7.51±0.53, and R(1) with strength equal to 2.81±0.65 mÅ).

HD	Obs.	Sp/L	E(B-V)	W(3957)	W(4232)	Lit	N(CH$^+$)	W(4964)	Lit	W(6196)	Lit
12953	t	A1Iae	0.60	9.8 (1.6)			20.67 (2.35)^x			31.2 (3.5)	
13854	t	B1Iabe	0.47		11.1 (1.5)		12.85 (1.74)			35 (3.5)	
14143	t	B2Ia	0.68	10.0 (1.4)	20 (1.6)		23.15 (1.85)			37.7 (3.4)	
23180	b	B1III	0.27	4.3 (0.7)	5.8 (0.2)	5.5^c	6.71 (0.23)	16.6 (0.8)	15.7(1.5)	13.6 (1.7)	12.7(1.0)
24398	b	B1Iab	0.29		3.9 (0.2)	2.4^c	4.51 (0.23)			15.3 (1.2)	16.2(1.0)
24534	b	O9.5pe	0.56	2.5 (0.3)	4.3 (0.5)		4.98 (0.58)	18.5 (0.9)		10.2 (1.8)	
25638	t	B0III	0.66		11.5 (3.0)		13.31 (3.47)			42 (3.3)	
27778	b	B3V	0.37	4.9 (0.7)	9.3 (0.5)		10.76 (0.58)	6 (0.3)	9.1(1.0)	7.8 (0.9)	11.5(0.5)
34078	b	O9.5Ve	0.49		47.67 (1.6)			23.7 (1.2)	27(2)	19.4 (1.5)	23(1)
45314	f	O9:pe	0.43	5.0 (0.8)	6.2 (1.7)		7.18 (1.97)	11.4 (0.6)		22.7 (1.7)	
46150	f	O6e	0.46	7.2 (0.9)	13.1 (1.3)		15.16 (1.50)	13.5 (0.7)		36.5 (2.3)	
46223	f	O5e	0.48	15.3 (1.6)	25 (1.4)		28.93 (1.62)	20.8 (1.0)		38.3 (3.2)	
46573	f	O7	0.63	14.4 (1.8)	23.7 (1.7)		30.38 (1.90)^x	22.8 (1.1)		43 (3.7)	
47432	f	O9.5III	0.42	4.8 (0.5)	8.3 (0.8)		9.61 (0.93)	9.2 (0.5)		24.6 (2.1)	
48434	f	B0III	0.21	6.2 (0.7)	9.1 (1.2)		10.53 (1.39)	5 (0.3)		13 (0.9)	
75149	f	B3Ia	0.39	7.6 (0.9)	11.5 (1.4)		13.31 (1.62)	7 (0.4)		25.7 (2.3)	
80558	f	B6Iae	0.60	13.3 (1.5)	18.5 (1.5)		21.41 (1.74)	17.2 (0.9)		47.5 (3.6)	
93130	f	O6	0.56	3.2 (0.6)	5.1 (0.3)		5.90 (0.35)	7.8 (0.4)		24 (2.1)	
94367	f	B9Ia	0.17	2.0 (0.4)	3.4 (0.3)		3.94 (0.35)	5 (0.3)		16.8 (1.1)	
99264	f	B2IVV	0.27	3.5 (0.5)	7.8 (0.5)		9.03 (0.35)	5.5 (0.3)		17.6 (1.4)	
99872	f	B3V	0.34	10.5 (1.3)	18.1 (0.9)		20.95 (1.04)	5.8 (0.3)		19.6 (1.9)	
101191	f	O8	0.37	12.5 (1.6)	24.4 (1.5)		28.24 (1.74)	6 (0.3)		18.5 (1.3)	
101205	f	O8v	0.33	6.5 (0.8)	11.1 (0.3)		12.85 (0.35)	3.6 (0.2)		17.2 (1.2)	
101223	f	O7	0.45	6.8 (1.0)	9.7 (0.6)		11.23 (0.69)	6.8 (0.3)		21.8 (2.1)	
104841	f	B2IV	0.09	5.3 (0.7)	8.8 (0.4)		10.18 (0.46)	4 (0.2)		6.8 (0.5)	
110432	f	B2pe	0.48	8.2 (0.9)	13.9 (0.4)	14.0^c	16.09 (0.46)	10.8 (0.5)		17.1 (1.5)	
116072	f	B2.5Vn	0.21	4.3 (1.1)	8.4 (0.3)		9.72 (0.35)	2.6 (0.3)		12.6 (1.1)	
141637	f	B1.5V	0.16		0.8 (0.3)		0.93 (0.35)	3.3 (0.2)		10.8 (1.0)	
147165	h	B1III	0.34	3.1 (0.4)	5.28 (0.3)		6.11 (0.35)	10 (0.5)		18.4 (0.4)	
147888	f	B3/B4V	0.46	4.1 (0.6)	7.2 (0.5)	6.2(0.5)^p	8.33 (0.58)	19.5 (1.0)	18(2)	19.3 (1.4)	19(1)
147889	h/u	B2III/IV	1.00	16.8 (1.8)	27.54 (1.7)		35.48 (1.90)^x	56 (2.8)	55(2)	47.2 (3.3)	46(2)
147932	f	B5V	0.47	3.3 (0.4)	6.3 (0.5)	6.0(0.6)^p	7.29 (0.58)	22.1 (1.1)		15.6 (1.1)	
147934	h	B2V	0.45	7.1 (0.9)	13.1 (1.4)		15.16 (1.62)	22.3 (1.1)		16.3 (0.3)	
148184	h/u	B2Vne	0.48	6.3 (0.6)	9.98 (1.2)	11.0^c	11.55 (1.39)	21 (1.1)		13.7 (0.4)	
148379	f	B2Iab	0.77	9.8 (1.0)	17.1 (1.5)		19.79 (1.73)	11.5 (0.6)		45 (2.4)	
148688	f	B1Ia	0.52	13.1 (2.0)	25.1 (1.6)		32.06 (1.79)^x	15 (0.8)		39 (3.5)	
148937	f	O6e	0.61	9.06 (1.3)	17.62 (1.6)		20.39 (1.85)	15.3 (0.8)		41.2 (1.9)	
149404	f	O9Ia	0.71	20.0 (1.9)	37.7 (1.9)		43.63 (2.20)	17.4 (0.9)		39.6 (2.3)	
149757	h/u	O9.5V	0.28	14.2 (1.7)	23.5 (2.1)	20.7^c	39.95 (2.35)^x	6.7 (0.3)	6(1)	10.5 (1.2)	10(1)
150136	f	O5	0.42	10.5 (1.2)	17.7 (1.3)		20.49 (1.55)	9.1 (0.5)		24 (1.3)	
150168	f	B1Iab/Ib	0.16	10.5 (1.3)	14.2 (1.2)		16.43 (1.39)	3.2 (0.2)		13.7 (1.1)	
151932	u	WN7	0.50	7.0 (1.6)	13 (1.2)		15.05 (1.39)	16.2 (1.0)		30.3 (2.0)	
152076	f	B0.5III	0.43	9.9 (1.5)	19.8 (1.4)		22.92 (1.62)	19.6 (1.0)		22.8 (1.2)	
152218	f	O9V	0.45	8.6 (1.2)	15.8 (1.6)		18.29 (1.85)	16.3 (0.8)		21.1 (1.7)	
152219	f	O9IV	0.44	13.1 (1.7)	21.4 (1.5)		24.77 (1.74)	11.5 (0.6)		25 (1.1)	
152233	h	O6III	0.42	13.8 (2.0)	22.1 (2.2)		29.11 (2.46)^x	13.3 (0.7)		22.5 (0.4)	
152234	f	B0.5Ia	0.42	12.6 (1.8)	22.2 (2.3)	19.0^c	26.58 (2.57)^x	13.7 (0.7)		25 (1.5)	
152235	h	B0.7Ia	0.78	25.4 (1.9)	41.91 (3.7)	42.0^c	53.65 (2.64)^x	20.4 (1.0)		37 (2.2)	
152236	f	B1Iape	0.65	9.6 (1.3)	17.6 (1.5)	15.0^c	20.37 (1.74)	18.7 (0.9)		39.1 (2.6)	
152246	f	O9Ib	0.44	7.7 (0.9)	15.6 (1.5)		18.06 (1.74)	13 (0.7)		25 (1.6)	
152249	h	O9Ib	0.48	10.4 (1.5)	17.8 (1.2)		20.60 (1.39)	10.8 (0.5)		23.1 (1.2)	
152314	f	B0.5Iab	0.39	13.7 (1.6)	20.1 (1.5)		23.26 (1.74)	14.8 (0.7)		24.3 (1.6)	
152667	f	B0.5Iae	0.47	5.7 (0.7)	11 (1.5)		12.73 (1.74)	13.5 (0.7)		30.4 (3.2)	
154090	f	B1Iae	0.45	10.4 (1.2)	18.1 (0.8)		20.95 (0.93)	13 (0.7)		20.5 (2.3)	
154368	f	O9.5Iab	0.73	10.2 (1.3)	17.5 (1.1)		20.25 (1.27)	31.2 (1.6)		27.1 (4.1)	
154445	f	B1V	0.35	9.8 (1.5)	17.1 (1.4)		19.79 (0.62)	11.6 (0.6)		24.5 (2.1)	
163800	h/u	O7	0.57	8.1 (0.9)	15.1 (1.7)		17.48 (1.97)	21.8 (1.1)		29.6 (0.9)	
164794	f	O4V	0.33	5.1 (0.7)	9.6 (1.3)		11.11 (1.50)	8.5 (2.0)		18 (1.3)	
165688	f	WN	1.00	26.1 (3.0)	46.3 (1.8)		55.06 (2.01)^x	27 (1.4)		57 (3.6)	
166734	f	O8e	1.38	25.1 (2.8)	45.5 (1.7)		52.95 (1.91)^x	33 (1.7)	33(1)	90 (4.2)	93(3)
168075	f	O7V	0.74		30.3 (1.5)		35.07 (1.74)	34 (1.7)		59 (2.5)	
168137	f	O8.5V	0.68		11.6 (1.5)		13.43 (1.74)	30 (1.5)		53 (2.7)	
168607	f	B9Ia	1.55	40.0 (3.7)	73 (1.8)		84.38 (2.01)^x	45.5 (2.3)		90 (3.6)	
168625	f	B6Ia	1.52	37.0 (3.2)	70 (1.8)		78.05 (2.01)^x	32.5 (1.6)		97 (3.7)	
179406	h/u	B3V	0.31	1.8 (0.4)	3.9 (1.7)		4.51 (1.97)	19.7 (1.0)	20(1)	19.4 (0.4)	19.8(0.7)
184915	h	B0.5III	0.19		6 (0.4)	5.0^c	6.94 (0.46)			16.1 (0.6)	
190603	t	B1.5Iae	0.71		24.5 (1.4)		28.36 (1.62)	17 (0.9)		33 (1.1)	
203064	t	O8V	0.25		4.1 (0.3)	6.5^c	4.75 (1.62)	18 (0.9)		18.3 (0.5)	
203938	t	B0.5IV	0.70	14.6 (1.6)	26.2 (2.1)		30.80 (1.45)^x	20 (1.0)		36.1 (3.4)	
204827	b	B0V	1.06	18.6 (1.9)	31 (1.8)	30.3(1.8)^p	39.24 (2.12)^x	55 (2.8)	55(1)	38.1 (2.3)	41.5(1.0)
206165	t	B2Ib	0.46		16.7 (1.0)	13.3(1.0)^p	19.33 (1.16)		15.8(1.0)	24.2 (1.1)	26(1)
206267	t	O6	0.49	8.0 (1.3)	10 (1.4)		11.57 (1.50)	21 (1.1)	24(2)	27.3 (1.4)	29(1)
207198	t	O9II	0.55		17.6 (1.4)	18.2(1.5)^p	20.37 (2.31)		29(1)	34.5 (1.7)	30(1)
207538	b	B0V	0.59		6.25 (1.3)	7.0(0.9)^p	13.77 (1.97)	27 (1.4)		33.5 (1.4)	
208501	t	B8Ib	0.77	7.1 (0.9)	10.3 (1.9)	3.0(1.1)^p	11.92 (1.16)	15.5 (0.8)		33.2 (1.8)	
209481	t	O9V	0.35		3.3 (1.0)	4.0(0.8)^p	3.82 (0.46)			22.2 (1.4)	
210839	t	O6e	0.56	6.0 (1.2)	9.3 (0.4)	12.1^c	10.76 (1.16)			30.7 (1.5)	31(1)
213087	t	B0.5Ibe	0.56	10.0 (1.1)	15.5 (1.0)		17.94 (1.50)			34.6 (3.5)	
326331	f	B	0.30	8.2 (0.9)	14.9 (1.3)		17.25 (2.31)	13.5 (0.7)		20.9 (1.9)	
BD134927	f	O7II	1.16		28.5 (2.0)		32.99 (1.97)	50 (2.5)		61 (3.4)	
BD134930	f	O9.5V	0.53		8.5 (1.7)		9.84 (1.86)	34 (1.7)		54 (3.2)	
CPD417733	f	O9III	0.49	9.6 (1.2)	15.4 (1.6)		17.82 (1.85)	12.1 (0.6)		19.4 (1.5)	
CPD417735	f	O9V	0.43	13.5 (1.5)	23 (1.6)		26.62 (1.85)	12 (0.6)		18 (1.3)	

Table 6.2: Calculated correlation coefficients with error in each case. With ^{x} we mark values published by Weselak et al. (2008c).

	N(CH)	N(CH+)	N(CN)	W(5780)	W(5797)	W(6196)	E(B-V)
W(4964)	0.84(0.04)	0.54(0.08)	0.47(0.09)	0.62(0.07)	0.83(0.03)	0.68(0.06)	0.80(0.04)
W(5780)	0.49(0.08)^x	0.79(0.09)	0.05(0.11)^x		0.86(0.03)	0.97(0.01)	0.85(0.03)^x
W(5797)	0.69(0.05)^x	0.70(0.06)	0.29(0.10)^x			0.92(0.92)	0.94(0.01)^x
W(6196)	0.57(0.07)	0.77(0.04)	0.08(0.10)				0.89(0.02)
E(B-V)	0.72(0.05)	0.79(0.04)	0.41(0.09)				

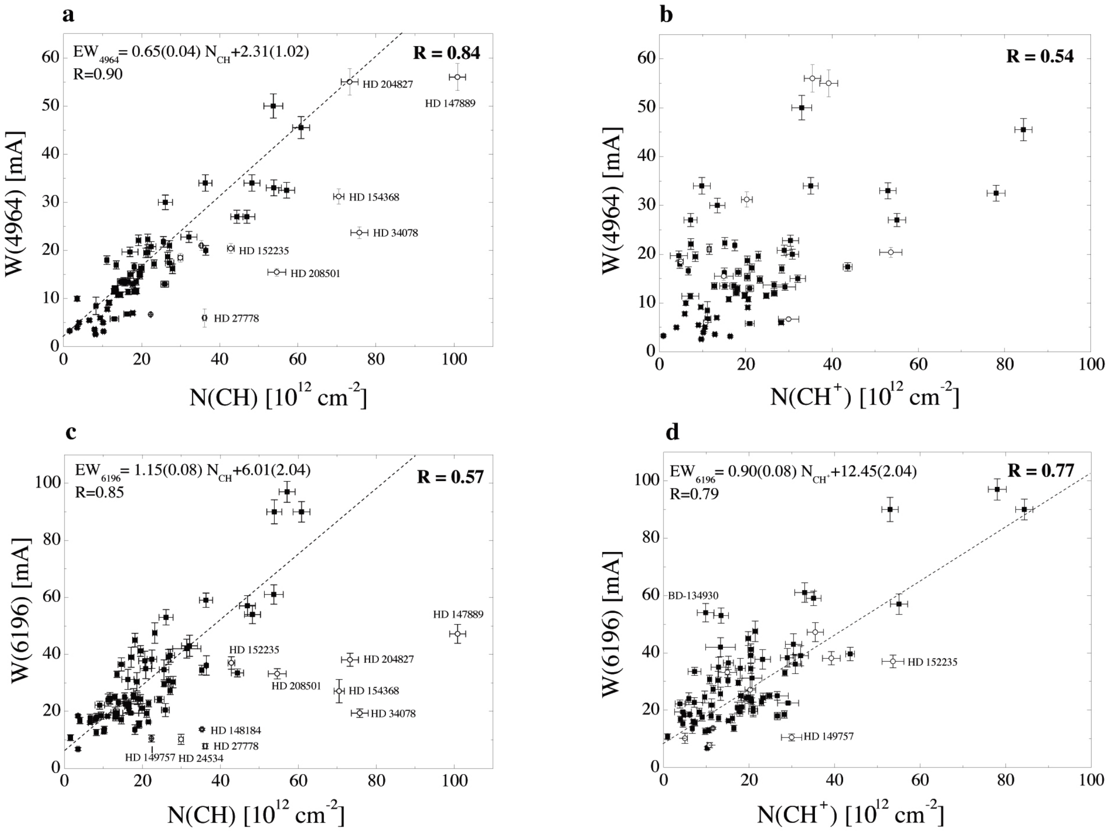

Figure 6.4: Molecular column densities of the CH (the left panel) and the CH$^+$ molecule (at the right) correlated with equivalent widths of the 4964 and 6196 DIBs. With boldface we mark correlation coefficients in the case of each relation. It is well seen that the 4964 DIB is better correlated with column density of CH molecule (panel "a"), while 6196 DIB with that of CH$^+$ (panel "d"), with correlation coefficients equal to 0.84 and 0.77, respectively. The CH abundant clouds missing the "main stream" are marked with open circles in each case (for more information see text). We also plot the relation and present the value of correlation coefficient in case of the "main stream" in (panels "a","c", and "d").

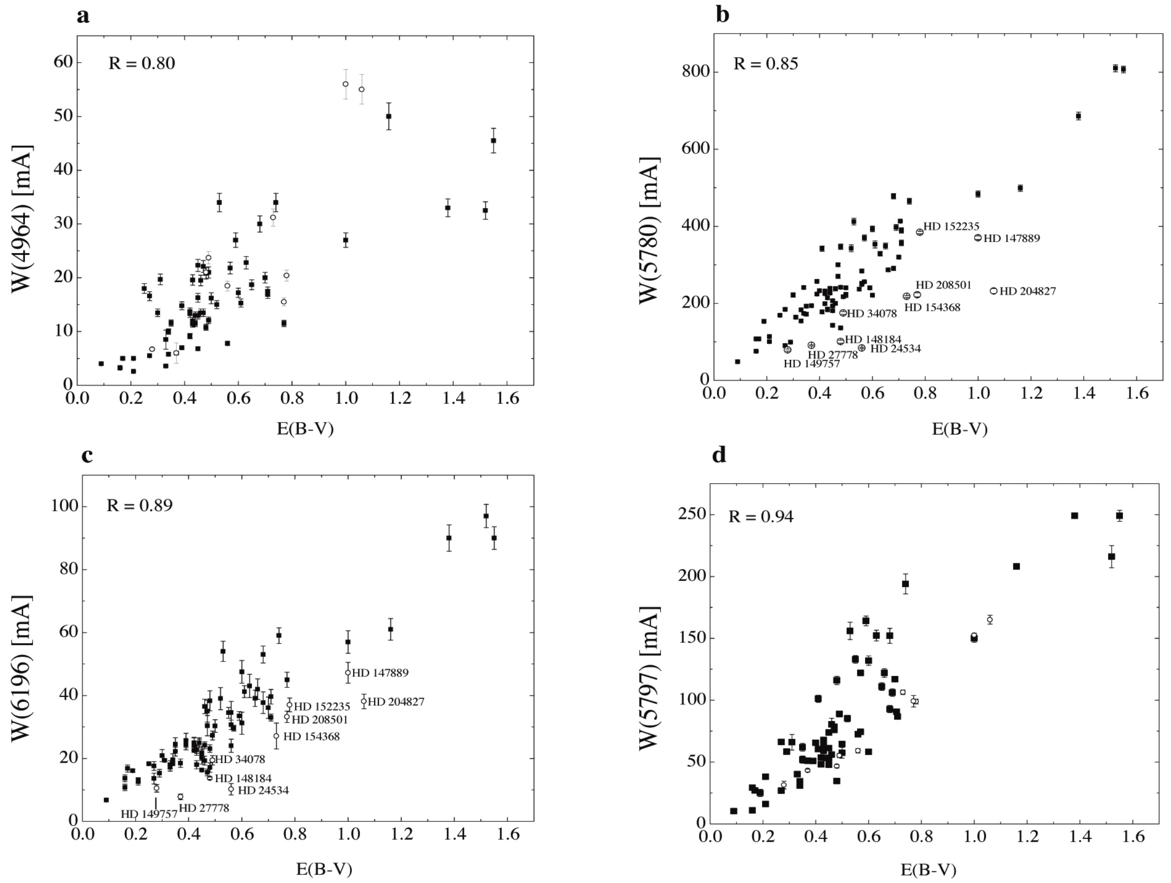

FIGURE 6.5: Strengths of 4964, 6196, 5780 and 5797 DIBs correlated with E(B-V). With open circles we mark "CH abundant clouds" in each plot. Note pretty tight correlation with E(B-V) in each case and CH abundant clouds which miss the "main stream" in the case of very well correlated 5780 and 6196 DIBs (panels "b" and "c"). Correlation coefficient between strengths of 5780 and 6196 DIBs is equal to 0.97 – see Table 6.2 in the text.

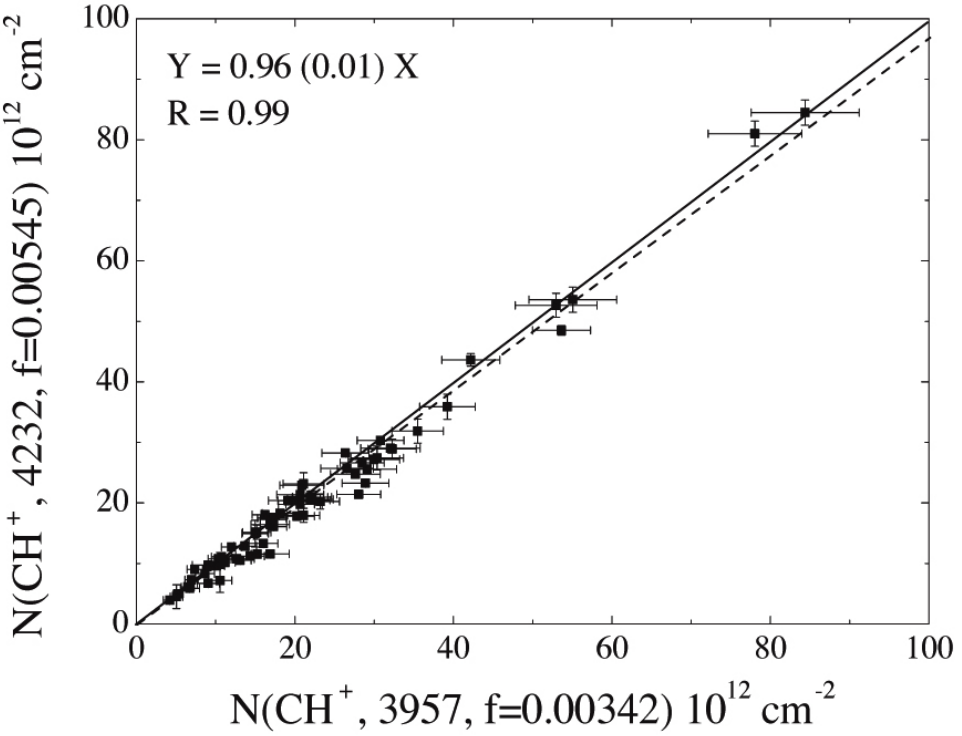

FIGURE 6.6: The relation between column densities derived from measurements of 3957 and 4232 bands. The solid line represents equal values derived from both bands based on f-values equal to 0.00342 and 0.00545, respectively. Dashed line represents fit to data–points.

7

Conclusion

This section presents summarizes the main results of this PhD project.

We have developed and demonstrated efficiency of a new method to study giant molecular clouds in other galaxies using near-infrared color maps and employing dust as a tracer of molecular hydrogen. In combination with a powerful wavelet-based multi-scale technique of clouds identification it allows to derive basic parameters of the molecular clouds, such as masses, sizes, and orientations (in respect to any preferential direction, like major or minor axis of a galaxy). In our study we focused on the Northern Dark Lane of the giant elliptical radio galaxy NGC5128 (Centaurus A). For the first time the mass spectrum of GMC's has been obtained. We found, that GMC's with masses above our completeness limit can be described by a power law distribution $dN/dM \propto M^{-2.31}$. This value is higher than the one for the Galactic GMCs. On the other hand it's in a good agreement with independent studies of GMC's in other galaxies. Such a high value infers that most of the mass of molecular hydrogen in the galaxy is located in low mass clouds. We also suggest that there is a cut-off at low masses.

In continuation of our study of dusty elliptical galaxies we analyzed the nucleus region of the giant elliptical galaxy NGC1316 (Fornax A). Using near-infrared imaging data and applying a 2-dimension decomposition analysis we have discovered a "peanut-shape" structure in the nucleus region of the galaxy, which turned out to be hidden behind dense dust lanes. We estimated the diameter of the structure of 0.76 kpc ($\sim 8''$) and projected minor axis of about 430 pc. Follow up kinematic study, using both optical and near–infrared spectroscopy, allowed us to propose few explanations of the structure:

- the galaxy most probably harbors a kinematically decoupled core

- a nuclear disk which has formed via recent merging event
- a boxy-peanut bulge ? (like in edge-on galaxies)

Our work on the chemistry of diffuse interstellar clouds led us to a discovery of a new class of objects – Ca-Fe interstellar clouds. They turned out to be rare (just a few examples among ∼ 300 lines of sight) objects with the Ca I 4227 Å, Fe I 3720 Åand 3860 Ålines stronger than those of K I (near 7699 Å) and Na I (near 3302 Å), occupying different volumes from the well-known interstellar H I clouds where the K I and ultraviolet Na I lines are dominant features. We established that the CaFe clouds can be found only along sight-lines toward hot, luminous (and thus distant) objects with high rates of mass loss. Evidently both simple molecular species and the complex ones (DIB carriers) are typically situated in the clouds characterized by a rather strong depletion of heavy elements. Apparently, the CaFe clouds contain very little if any CH or DIB carriers. It seems thus ill-advised to determine the rest wavelengths of DIBs by measuring the radial velocities of interstellar clouds from current wavelengths of Fe I or Ca I lines. We found that the correlation between the two latter is also far from being perfect.

Detailed analysis of intensity ratios of unsaturated methylidyne (CH) A–X, B–X and C–X bands revealed inconsistency of the published oscillator strengths . While the latter are consistent for the main B–X and C–X transitions we suggest the new oscillator strength of the CH A–X band 4300.313 Å to be equal to $434\pm31\times10^{-5}$. This result is based on the assumption that f-values of CH B-X system (at 3886 and 3890 Å), i.e. 320 and 210×10^{-5} respectively are correct. We also recommend the oscillator strengths of the CH C–X lines at 3137.5582, 3143.1647 and 3145.9965 Å to be (in 10^{-5} each) 415±30, 640 and 267±17 respectively. Based on optical spectra of 52 stars (in 39 objects all CH features are unsaturated) obtained by high-resolution echelle spectrographs we estimated methylidyne column densities using the new consistent system of the oscillator strengths. We emphasized the importance of collecting precise f-values based on observational material and comparing them to experimental and theoretical results.

We studied spatial correlations of some DIBs and simple molecules. We found that radial velocities of CH, CH^+ features and two narrow diffuse interstellar bands: 6196 and 4964 suggest that 6196 DIB carrier is spatially correlated with CH^+ while 4964 DIB carrier prefers environments where CH molecule is abundant. Using statistically meaningful sample of 83 reddened OB stars and analyzing correlations between CH and CH^+ column densities and DIB strengths we clearly confirm this suggestion. We found that each of the presented diffuse bands is pretty tightly correlated with E(B-V). CH and CH^+ molecules are also rather well correlated with E(B-V) – correlation coefficients equal to 0.72 and 0.79, respectively. Moreover the major 5780 DIB is well correlated with 6196 one with the correlation coefficient 0.97. We emphasize that future identification of DIB carriers requires analyzes of environments in which they do exist.

A

Appendix

Table A.1: Cloud Properties for Clouds found in Centaurus A

Number	α (J2000)	δ (J2000)	r, pc	$M(10^4 M_\odot)$	*density*	PA	e
1	13:25:27.569	-43:01:08.49	70.66	63.63	0.12	33.05	0.74
3	13:25:33.333	-43:01:07.49	73.79	72.23	0.12	-60.77	0.25
4	13:25:30.958	-43:00:36.15	55.50	39.26	0.12	-13.00	0.58
5	13:25:27.883	-43:01:01.57	24.36	6.97	0.11	28.54	0.33
6	13:25:33.448	-43:01:48.97	67.24	51.98	0.11	26.60	0.47
7	13:25:28.542	-43:01:02.71	33.62	10.69	0.09	-66.72	0.08
8	13:25:37.502	-43:01:47.71	55.50	34.84	0.11	38.54	0.74
9	13:25:31.804	-43:00:55.72	85.88	103.16	0.13	56.18	0.56
10	13:25:25.459	-43:00:46.07	45.32	23.86	0.11	26.11	0.56
11	13:25:27.383	-43:00:58.41	40.83	18.43	0.10	8.48	0.16
12	13:25:20.631	-42:59:37.60	32.19	9.01	0.08	37.43	0.12
13	13:25:22.802	-43:00:55.63	45.63	20.64	0.09	17.59	0.19
14	13:25:26.776	-43:00:54.68	40.72	17.11	0.10	-97.05	0.12
15	13:25:31.785	-43:01:31.15	50.15	29.22	0.11	33.12	0.45
16	13:25:23.829	-43:00:55.90	45.52	20.34	0.09	26.79	0.36
17	13:25:23.116	-43:00:46.69	53.07	33.46	0.11	38.44	0.31
18	13:25:36.980	-43:02:07.60	28.46	6.46	0.08	58.81	0.51
19	13:25:33.181	-43:01:34.00	53.78	35.80	0.12	26.27	0.49
20	13:25:30.275	-43:00:44.23	42.31	17.00	0.09	50.61	0.51
21	13:25:25.424	-43:00:00.26	47.55	23.72	0.10	-248.24	0.45

Number	α (J2000)	δ (J2000)	r, pc	$M(10^4 M_\odot)$	*density*	PA	e
22	13:25:29.040	-43:00:54.92	35.40	13.01	0.10	-128.26	0.08
23	13:25:25.978	-43:00:05.44	36.32	14.74	0.11	-34.98	0.40
24	13:25:24.883	-43:01:02.21	37.71	14.67	0.10	-83.90	0.13
25	13:25:25.541	-43:01:05.37	51.90	25.79	0.09	81.98	0.48
26	13:25:33.965	-43:01:08.91	42.42	18.84	0.10	17.89	0.41
27	13:25:23.250	-43:00:58.50	42.75	19.41	0.10	-111.41	0.28
28	13:25:37.157	-43:01:37.06	50.15	28.67	0.11	-5.75	0.41
29	13:25:21.720	-43:00:40.96	84.72	83.01	0.11	37.64	0.54
30	13:25:38.112	-43:02:04.98	58.88	36.67	0.10	24.26	0.48
31	13:25:24.432	-43:00:44.07	40.83	15.98	0.09	15.61	0.21
32	13:25:24.039	-43:00:54.17	26.76	7.65	0.10	-48.98	0.30
33	13:25:27.454	-43:00:18.66	41.29	20.01	0.11	38.18	0.56
34	13:25:26.725	-43:00:59.29	32.91	10.12	0.09	-10.45	0.48
35	13:25:30.360	-43:01:13.33	22.13	4.81	0.09	-32.80	0.34
36	13:25:27.328	-43:00:46.60	29.12	8.98	0.10	38.88	0.34
37	13:25:26.302	-43:00:52.68	43.84	20.49	0.10	43.23	0.55
38	13:25:32.919	-43:01:41.21	30.23	8.66	0.09	-95.30	0.27
39	13:25:31.050	-43:01:40.96	54.30	31.58	0.10	-114.22	0.37
40	13:25:34.214	-43:02:03.35	26.58	6.02	0.08	27.24	0.17
41	13:25:34.713	-43:01:56.14	26.22	5.86	0.08	52.72	0.34
42	13:25:32.843	-43:01:52.44	62.37	38.37	0.09	32.18	0.66
43	13:25:24.988	-43:01:05.67	30.23	9.60	0.10	-231.10	0.39
44	13:25:33.870	-43:01:52.99	30.38	7.65	0.08	53.05	0.33
45	13:25:21.684	-42:59:40.46	22.76	5.11	0.09	39.12	0.34
46	13:25:35.733	-43:01:26.44	21.92	4.38	0.09	-55.49	0.11
47	13:25:20.481	-43:00:28.02	18.92	3.29	0.09	29.57	0.26
48	13:25:38.401	-43:02:03.24	44.79	20.71	0.10	-50.30	0.22
49	13:25:22.111	-43:00:18.19	46.95	19.22	0.08	-78.74	0.46
50	13:25:23.904	-43:00:36.88	19.65	4.06	0.10	-123.34	0.33
51	13:25:25.213	-42:59:57.68	31.90	9.32	0.09	19.22	0.35
52	13:25:33.766	-43:02:00.49	26.40	5.91	0.08	-64.14	0.10
53	13:25:32.104	-43:01:42.67	49.68	26.31	0.10	45.25	0.57
55	13:25:24.767	-43:00:02.87	22.34	4.76	0.09	35.57	0.21
56	13:25:33.808	-43:01:11.80	36.70	10.79	0.08	7.16	0.44
57	13:25:32.943	-43:01:28.24	31.00	8.91	0.09	33.52	0.23
58	13:25:28.745	-43:00:24.96	31.30	10.24	0.10	19.16	0.24
59	13:25:34.768	-43:02:07.66	24.93	4.58	0.07	59.95	0.53
60	13:25:36.021	-43:01:17.79	39.18	15.52	0.10	-34.03	0.27
61	13:25:31.908	-43:00:48.22	27.45	6.91	0.09	-88.31	0.16
62	13:25:20.925	-43:00:03.53	26.93	5.54	0.07	-37.10	0.21
63	13:25:30.596	-43:01:06.98	22.97	5.01	0.09	44.51	0.54
64	13:25:33.498	-43:01:39.46	19.17	3.17	0.08	-127.53	0.13

Number	α (J2000)	δ (J2000)	r, pc	$M(10^4 M_\odot)$	$density$	PA	e
65	13:25:35.902	-43:02:15.70	24.55	5.36	0.08	-17.26	0.29
66	13:25:25.534	-43:00:23.89	41.97	16.92	0.09	-129.54	0.41
67	13:25:24.194	-43:00:40.91	29.28	7.91	0.09	44.24	0.37
68	13:25:34.757	-43:01:16.96	36.57	11.79	0.08	-14.20	0.46
69	13:25:22.748	-43:00:46.70	27.62	6.05	0.07	10.65	0.33
70	13:25:34.475	-43:01:52.11	26.04	6.32	0.09	-85.41	0.30
71	13:25:36.971	-43:01:30.73	40.13	14.63	0.09	33.06	0.50
72	13:25:30.885	-43:01:08.13	28.30	6.46	0.08	-120.36	0.32
73	13:25:32.488	-43:00:53.11	31.45	7.82	0.07	-80.92	0.26
74	13:25:27.191	-43:00:19.53	24.93	6.32	0.10	-34.72	0.22
75	13:25:23.081	-42:59:52.82	40.13	14.97	0.09	-133.62	0.43
76	13:25:26.453	-43:00:12.92	16.53	2.28	0.08	-56.95	0.20
77	13:25:31.995	-43:01:28.55	32.34	9.49	0.09	-99.53	0.12
78	13:25:37.508	-43:02:13.35	39.06	12.19	0.08	-119.77	0.27
79	13:25:25.558	-43:00:12.36	27.96	7.56	0.09	37.98	0.21
80	13:25:25.507	-43:00:19.28	21.70	4.05	0.08	-1.25	0.25
81	13:25:29.854	-43:00:45.10	27.79	6.82	0.08	-39.83	0.43
82	13:25:36.999	-43:01:34.76	29.60	7.67	0.08	-46.17	0.12
83	13:25:38.818	-43:01:44.21	30.69	7.92	0.08	35.07	0.36
84	13:25:35.954	-43:02:12.81	32.77	10.16	0.09	44.37	0.13
85	13:25:32.684	-43:01:46.97	30.38	7.07	0.07	5.44	0.50
86	13:25:35.639	-43:02:14.84	16.81	2.48	0.08	-12.89	0.50
87	13:25:36.795	-43:02:03.57	32.91	9.41	0.08	-70.09	0.13
88	13:25:30.644	-43:00:46.81	21.92	4.47	0.09	-49.50	0.37
89	13:25:25.378	-43:00:38.29	27.79	7.19	0.09	-118.40	0.43
90	13:25:32.339	-43:01:36.32	34.04	11.03	0.09	46.31	0.42
91	13:25:26.327	-43:00:41.73	39.30	15.48	0.09	30.19	0.57
92	13:25:34.132	-43:01:49.24	33.48	9.44	0.08	32.19	0.43
93	13:25:24.382	-43:00:59.92	45.11	17.51	0.08	11.54	0.46
94	13:25:36.164	-43:02:10.50	25.86	6.03	0.08	-91.87	0.28
95	13:25:26.538	-43:00:44.61	31.90	10.00	0.09	52.82	0.48
96	13:25:26.088	-43:00:30.50	19.17	3.05	0.08	-68.34	0.16
97	13:25:34.952	-43:02:07.08	18.67	2.73	0.07	-18.84	0.11
98	13:25:23.720	-43:00:35.16	22.13	4.19	0.08	-130.95	0.03
99	13:25:31.758	-43:01:26.83	29.91	8.43	0.09	34.27	0.44
100	13:25:31.417	-43:01:30.30	37.71	14.41	0.10	32.48	0.38
101	13:25:24.346	-43:00:02.88	33.76	9.82	0.08	64.04	0.35
102	13:25:23.330	-43:01:03.40	22.13	4.12	0.08	-42.45	0.37
103	13:25:31.675	-43:01:05.80	24.74	5.20	0.08	-107.89	0.09
104	13:25:24.381	-43:00:55.60	33.76	9.78	0.08	-32.95	0.24
105	13:25:28.779	-43:01:05.87	24.74	4.56	0.07	61.67	0.61
106	13:25:21.217	-43:00:22.53	19.17	3.09	0.08	-19.41	0.32

Number	α (J2000)	δ (J2000)	r, pc	$M(10^4 M_\odot)$	$density$	PA	e
107	13:25:20.741	-43:00:09.58	16.24	1.87	0.07	-34.79	0.67
108	13:25:28.218	-43:00:22.10	26.93	6.50	0.08	-29.32	0.17
109	13:25:31.172	-43:00:53.72	35.66	10.11	0.07	-49.59	0.26
110	13:25:25.687	-43:00:00.55	29.60	7.04	0.08	58.64	0.46
111	13:25:25.322	-43:00:17.55	24.36	5.25	0.08	-114.51	0.07
112	13:25:29.967	-43:01:20.83	28.63	6.83	0.08	32.23	0.53
113	13:25:36.294	-43:02:00.99	27.45	6.12	0.08	-97.25	0.41
114	13:25:37.265	-43:01:49.44	42.19	13.39	0.07	55.64	0.70
115	13:25:24.880	-43:00:46.37	25.68	5.36	0.08	-124.33	0.29
116	13:25:20.533	-43:00:25.43	21.26	3.41	0.07	-49.73	0.32
117	13:25:33.472	-43:01:41.48	32.04	8.40	0.08	59.65	0.44
118	13:25:37.561	-43:02:15.36	25.68	4.93	0.07	-68.88	0.20
119	13:25:34.265	-43:01:52.12	23.97	4.54	0.07	-104.43	0.11
120	13:25:31.731	-43:01:21.36	20.82	2.99	0.07	44.74	0.55
121	13:25:33.279	-43:00:59.42	25.49	5.61	0.08	69.64	0.52
122	13:25:36.188	-43:01:57.25	21.48	3.62	0.07	36.26	0.32
123	13:25:38.660	-43:01:43.93	17.90	2.71	0.08	-102.80	0.42
124	13:25:23.486	-43:00:53.60	22.55	3.86	0.07	26.87	0.08
125	13:25:31.671	-43:00:46.79	20.82	3.83	0.08	-3.51	0.45
126	13:25:23.377	-43:00:32.29	31.00	7.58	0.07	61.89	0.45
127	13:25:32.199	-43:00:55.42	41.18	13.34	0.07	79.90	0.69
128	13:25:23.013	-43:00:59.08	23.37	4.46	0.08	-130.91	0.28
129	13:25:26.560	-43:00:20.69	23.57	5.62	0.10	-126.58	0.47
130	13:25:32.658	-43:01:50.14	30.69	7.85	0.08	38.36	0.47
131	13:25:37.556	-43:01:52.03	29.60	6.45	0.07	10.96	0.57
132	13:25:35.470	-43:01:27.60	26.04	5.21	0.07	7.06	0.31
133	13:25:36.689	-43:02:02.42	26.40	5.67	0.08	-42.95	0.54
134	13:25:20.691	-43:00:25.42	19.41	3.35	0.08	70.80	0.62
135	13:25:31.094	-43:00:59.77	39.42	14.47	0.09	33.40	0.57
136	13:25:32.738	-43:01:54.75	31.45	7.20	0.07	25.80	0.80
137	13:25:30.778	-43:00:56.32	21.92	3.73	0.07	-76.44	0.22
138	13:25:33.524	-43:01:34.56	27.79	6.02	0.07	-106.95	0.41
139	13:25:22.211	-42:59:45.93	21.92	4.57	0.09	88.67	0.37
140	13:25:38.901	-43:02:01.50	18.67	2.80	0.08	-43.80	0.11
141	13:25:36.268	-43:02:03.88	26.58	6.42	0.09	-36.53	0.42
142	13:25:24.830	-43:01:04.81	16.81	2.16	0.07	-39.12	0.17
143	13:25:25.093	-43:01:02.79	34.04	9.75	0.08	44.38	0.20
144	13:25:35.346	-43:02:01.88	15.95	2.13	0.08	-63.08	0.17
145	13:25:36.296	-43:02:10.21	17.36	2.15	0.07	-115.18	0.37
146	13:25:20.533	-43:00:22.83	27.79	5.51	0.07	-0.85	0.43
147	13:25:24.058	-43:00:14.41	38.09	12.92	0.08	-127.91	0.25
148	13:25:36.430	-43:02:20.58	19.41	3.15	0.08	-10.32	0.52

Number	α (J2000)	δ (J2000)	r, pc	$M(10^4 M_\odot)$	$density$	PA	e
149	13:25:35.658	-43:01:41.71	24.93	4.95	0.07	54.87	0.59
150	13:25:29.411	-43:01:04.13	26.93	5.79	0.08	0.43	0.41
151	13:25:26.874	-43:00:15.21	18.92	2.96	0.08	7.41	0.12
152	13:25:32.655	-43:01:34.87	30.23	7.02	0.07	-59.27	0.35
153	13:25:27.908	-43:00:51.78	19.65	3.14	0.08	-110.16	0.22
154	13:25:34.874	-43:02:09.96	19.89	3.29	0.08	-96.09	0.38
155	13:25:25.329	-43:00:57.31	30.69	8.01	0.08	19.82	0.67
156	13:25:34.478	-43:02:03.64	27.62	6.45	0.08	25.48	0.44
157	13:25:35.085	-43:02:11.97	17.09	2.22	0.07	51.02	0.60
158	13:25:30.698	-43:00:53.73	23.37	4.91	0.08	-114.82	0.22
159	13:25:38.242	-43:02:00.07	23.37	4.35	0.08	11.45	0.36
160	13:25:36.166	-43:02:15.98	21.48	3.44	0.07	-122.10	0.40
161	13:25:33.951	-43:02:02.21	22.76	4.16	0.08	-128.51	0.48
162	13:25:20.611	-43:00:19.66	23.17	3.80	0.07	-85.08	0.32
163	13:25:21.298	-43:00:35.78	37.21	10.07	0.07	-241.28	0.48
164	13:25:37.296	-43:02:06.15	33.76	8.49	0.07	-92.25	0.05
165	13:25:23.795	-43:00:15.86	26.58	5.08	0.07	17.36	0.25
166	13:25:24.268	-43:00:11.52	23.37	3.90	0.07	-263.30	0.51
167	13:25:31.199	-43:00:56.02	28.63	6.20	0.07	-36.04	0.26
168	13:25:23.060	-43:00:27.97	19.17	2.38	0.06	85.43	0.54
169	13:25:35.839	-43:01:27.01	22.76	3.65	0.07	-229.55	0.57
170	13:25:32.364	-43:01:29.98	30.54	7.02	0.07	-4.71	0.44
171	13:25:27.436	-43:01:05.04	37.84	11.74	0.08	20.11	0.42
172	13:25:38.136	-43:01:54.60	30.23	7.02	0.07	71.39	0.46
173	13:25:22.349	-43:00:22.51	27.45	6.35	0.08	19.52	0.31
174	13:25:29.255	-43:01:15.37	22.13	4.08	0.08	26.62	0.65
175	13:25:20.006	-43:00:17.37	16.81	2.39	0.08	-87.46	0.48
176	13:25:35.164	-43:02:11.11	18.67	2.87	0.08	31.37	0.58
177	13:25:35.336	-43:01:18.09	19.89	3.05	0.07	22.22	0.44
178	13:25:30.628	-43:01:34.35	48.72	19.49	0.08	53.81	0.47
179	13:25:32.070	-43:01:05.79	30.54	6.21	0.06	-22.39	0.35
180	13:25:31.630	-43:01:44.12	33.48	8.56	0.07	-106.56	0.42
181	13:25:26.568	-43:01:04.48	53.95	21.12	0.07	-32.52	0.50
182	13:25:24.036	-43:00:37.46	15.65	1.92	0.07	-134.40	0.12
183	13:25:22.511	-43:00:47.00	32.77	8.01	0.07	75.42	0.50
184	13:25:21.950	-42:59:56.30	26.04	5.24	0.07	48.75	0.47
185	13:25:38.268	-43:01:59.21	22.97	3.40	0.06	24.35	0.71
186	13:25:35.317	-43:01:49.79	16.53	1.95	0.07	36.01	0.16
187	13:25:23.277	-43:01:00.23	29.44	6.95	0.08	-2.05	0.48
188	13:25:31.313	-43:01:40.38	33.62	9.96	0.08	-40.00	0.04
189	13:25:21.612	-43:00:25.41	15.95	1.90	0.07	-3.78	0.47
190	13:25:31.045	-43:01:15.32	22.55	4.44	0.08	-73.46	0.49

Number	α (J2000)	δ (J2000)	r, pc	$M(10^4 M_\odot)$	$density$	PA	e
191	13:25:37.218	-43:02:13.36	22.55	3.88	0.07	-111.85	0.29
192	13:25:38.133	-43:01:45.39	16.53	2.22	0.08	38.27	0.23
193	13:25:30.811	-43:01:29.74	24.17	4.36	0.07	-15.10	0.22
194	13:25:29.968	-43:01:29.47	17.90	2.50	0.07	-84.94	0.31
195	13:25:36.027	-43:01:44.87	17.36	2.16	0.07	27.62	0.57
196	13:25:31.863	-43:01:24.81	21.48	3.40	0.07	23.24	0.28
197	13:25:30.286	-43:01:37.53	37.71	11.10	0.07	-25.57	0.15
198	13:25:30.619	-43:00:51.42	23.57	4.75	0.08	-67.70	0.31
199	13:25:29.834	-43:01:17.08	20.36	3.37	0.08	-68.67	0.39
200	13:25:32.340	-43:01:38.92	17.36	2.18	0.07	-247.63	0.32
201	13:25:22.246	-43:00:35.19	16.81	2.37	0.08	-80.31	0.43
202	13:25:22.663	-43:00:10.69	23.17	4.12	0.07	-7.43	0.25
203	13:25:32.841	-43:01:42.94	21.48	3.56	0.07	24.95	0.54
204	13:25:33.524	-43:01:36.29	19.65	3.05	0.07	20.21	0.42
205	13:25:22.398	-43:00:01.48	27.79	5.44	0.07	-49.14	0.23
206	13:25:36.163	-43:02:02.73	19.17	2.88	0.07	-238.36	0.57
207	13:25:24.450	-42:59:57.40	18.67	2.57	0.07	-80.55	0.19
208	13:25:31.841	-43:01:46.13	24.93	4.50	0.07	-9.51	0.26
209	13:25:36.576	-43:01:26.13	19.89	2.67	0.06	-109.75	0.36
210	13:25:27.880	-43:00:45.15	21.92	3.68	0.07	50.28	0.47
211	13:25:31.470	-43:01:33.75	16.53	1.80	0.06	-42.75	0.33
212	13:25:27.124	-43:01:20.89	35.66	8.01	0.06	25.10	0.60
213	13:25:37.632	-43:01:40.79	26.76	5.17	0.07	-128.15	0.48
214	13:25:28.067	-43:01:00.42	21.04	3.27	0.07	26.48	0.23
215	13:25:35.610	-43:02:01.88	24.36	4.64	0.07	0.91	0.33
216	13:25:30.907	-43:00:44.21	20.59	3.14	0.07	16.01	0.34
217	13:25:27.201	-43:01:11.96	47.25	16.46	0.07	-35.43	0.47
218	13:25:28.271	-43:00:24.69	25.86	6.18	0.09	-24.60	0.36
219	13:25:25.277	-43:00:59.33	21.92	4.03	0.08	44.49	0.20
220	13:25:19.684	-42:59:41.65	15.65	1.73	0.07	-118.58	0.25
221	13:25:30.539	-43:00:45.66	22.55	3.98	0.07	-3.77	0.25
222	13:25:21.616	-43:00:45.28	18.92	2.25	0.06	33.23	0.39
223	13:25:24.010	-43:00:41.78	17.90	2.20	0.06	-107.85	0.36
224	13:25:37.871	-43:01:47.41	31.45	7.46	0.07	-106.34	0.42
225	13:25:30.311	-43:01:28.88	20.36	3.36	0.08	-37.06	0.33
226	13:25:19.790	-42:59:41.08	16.81	2.13	0.07	65.61	0.38
227	13:25:24.138	-43:00:18.44	26.76	4.93	0.06	-113.86	0.18
228	13:25:23.528	-42:59:54.54	31.45	7.53	0.07	28.59	0.21
229	13:25:38.002	-43:01:46.54	19.65	2.94	0.07	-134.44	0.15
230	13:25:24.835	-43:01:33.33	22.55	3.33	0.06	-225.87	0.48
231	13:25:28.990	-43:01:08.75	17.63	2.23	0.07	-58.06	0.32
232	13:25:27.296	-43:00:17.80	19.89	2.98	0.07	-44.46	0.36

Number	α (J2000)	δ (J2000)	r, pc	$M(10^4 M_\odot)$	$density$	PA	e
233	13:25:30.802	-43:00:45.37	16.53	2.11	0.07	-122.89	0.30
234	13:25:30.513	-43:00:49.70	21.04	3.31	0.07	-70.55	0.24
235	13:25:28.672	-43:00:56.94	29.28	6.30	0.07	-0.55	0.09
236	13:25:36.311	-43:01:20.66	41.06	12.44	0.07	-18.87	0.17
237	13:25:28.061	-43:00:27.00	17.63	2.31	0.07	20.54	0.24
238	13:25:30.179	-43:01:28.31	17.90	2.63	0.08	-26.19	0.37
239	13:25:23.769	-43:00:17.87	18.92	2.58	0.07	-79.90	0.28
240	13:25:31.467	-43:01:21.65	21.48	3.32	0.07	-36.93	0.33
241	13:25:22.266	-42:59:58.89	27.62	5.69	0.07	36.51	0.10
242	13:25:34.109	-43:02:05.09	17.36	2.22	0.07	37.71	0.43
243	13:25:30.547	-43:01:27.15	23.97	4.65	0.08	-9.86	0.04
244	13:25:20.080	-42:59:49.42	20.59	3.12	0.07	-109.50	0.17
245	13:25:31.074	-43:01:27.14	29.44	6.19	0.07	-3.61	0.33
246	13:25:29.307	-43:01:11.33	23.37	3.80	0.07	-26.37	0.53
247	13:25:30.836	-43:01:22.53	15.95	1.88	0.07	29.01	0.49
248	13:25:22.010	-43:00:43.26	42.64	13.23	0.07	-235.57	0.42
249	13:25:36.641	-43:02:21.73	15.65	1.68	0.06	31.57	0.21
250	13:25:27.879	-43:00:41.69	24.55	4.47	0.07	30.62	0.57
251	13:25:34.526	-43:01:42.03	19.17	2.66	0.07	-107.17	0.58
252	13:25:26.224	-43:00:59.30	23.57	3.73	0.06	-27.82	0.02
253	13:25:37.367	-43:01:33.60	17.09	1.99	0.06	-114.69	0.27
254	13:25:27.349	-43:00:21.54	29.76	6.91	0.07	22.34	0.64
255	13:25:26.220	-43:00:33.38	19.17	2.83	0.07	-88.20	0.36
256	13:25:36.109	-43:02:00.42	21.04	3.47	0.07	-46.26	0.22
257	13:25:22.696	-43:00:49.01	18.42	2.26	0.06	-37.09	0.03
258	13:25:30.494	-43:01:26.00	28.79	6.49	0.07	-134.38	0.20
259	13:25:27.034	-43:00:22.12	21.26	3.40	0.07	-260.39	0.52
260	13:25:35.691	-43:02:13.69	17.36	2.35	0.07	13.11	0.19
261	13:25:29.510	-43:00:35.03	24.93	4.47	0.07	-130.52	0.44
262	13:25:34.229	-43:01:10.92	33.48	8.43	0.07	-131.53	0.22
263	13:25:22.301	-43:00:48.73	22.34	3.47	0.07	80.09	0.53
264	13:25:33.888	-43:01:15.54	22.13	3.35	0.06	39.04	0.63
265	13:25:35.915	-43:01:16.35	18.67	2.58	0.07	-35.64	0.50
266	13:25:19.842	-42:59:37.91	16.53	1.84	0.06	-11.22	0.15
267	13:25:22.081	-42:59:51.40	23.77	3.70	0.06	-73.20	0.21
268	13:25:33.708	-43:01:33.98	18.67	2.46	0.07	-85.37	0.19
269	13:25:33.892	-43:01:35.71	23.77	4.29	0.07	-37.78	0.51
270	13:25:23.003	-42:59:58.59	18.16	2.22	0.06	-10.43	0.36
271	13:25:29.727	-43:01:09.02	22.97	3.77	0.07	-51.85	0.42
272	13:25:29.456	-43:00:27.54	17.63	2.13	0.06	-16.50	0.63
273	13:25:25.085	-43:00:18.13	19.89	3.09	0.07	43.22	0.42
274	13:25:35.135	-43:01:59.87	17.36	2.15	0.07	-29.74	0.31

Number	α (J2000)	δ (J2000)	r, pc	$M(10^4 M_\odot)$	$density$	PA	e
275	13:25:31.841	-43:01:44.69	17.90	2.61	0.08	8.55	0.19
276	13:25:27.196	-43:00:44.30	20.82	3.10	0.07	-81.29	0.17
277	13:25:23.135	-43:00:00.60	19.17	2.60	0.07	-83.60	0.36
278	13:25:36.867	-43:01:33.32	21.92	3.11	0.06	-106.67	0.31
279	13:25:25.138	-43:00:16.40	20.36	2.87	0.07	-66.33	0.34
280	13:25:24.752	-43:01:07.40	22.34	3.40	0.06	-19.93	0.32
281	13:25:25.702	-43:01:19.48	21.26	2.92	0.06	62.81	0.52
282	13:25:34.635	-43:02:01.90	19.41	2.44	0.06	-111.95	0.23
283	13:25:32.517	-43:01:06.93	30.38	6.72	0.07	-114.62	0.34
284	13:25:36.030	-43:01:58.98	22.76	4.01	0.07	-25.14	0.25
285	13:25:31.652	-43:01:22.22	20.82	2.96	0.06	54.56	0.45
286	13:25:27.274	-43:00:43.72	15.65	1.63	0.06	-90.97	0.22
287	13:25:31.812	-43:01:34.90	24.17	4.19	0.07	-24.90	0.33
288	13:25:21.193	-43:00:34.63	17.90	2.00	0.06	-226.36	0.77
289	13:25:30.723	-43:00:48.54	19.41	2.72	0.07	5.97	0.44
290	13:25:30.886	-43:01:13.02	17.90	2.12	0.06	3.30	0.46
291	13:25:31.178	-43:01:24.83	21.26	3.14	0.07	-105.68	0.17
292	13:25:36.483	-43:02:22.31	15.95	1.69	0.06	-16.87	0.34
293	13:25:22.264	-42:59:48.23	20.82	2.76	0.06	-57.53	0.06
294	13:25:33.043	-43:01:01.45	17.09	2.09	0.07	65.49	0.55
295	13:25:20.132	-42:59:45.97	19.65	2.35	0.06	44.71	0.47
296	13:25:35.789	-43:01:40.27	26.93	5.36	0.07	43.96	0.68
297	13:25:32.649	-43:01:07.51	21.04	3.20	0.07	-242.03	0.40
298	13:25:23.668	-43:00:42.07	16.24	1.87	0.07	-129.43	0.29
299	13:25:22.343	-42:59:46.50	19.17	2.67	0.07	7.02	0.32
300	13:25:28.619	-43:00:53.49	25.31	4.64	0.07	-10.46	0.42
301	13:25:32.235	-43:01:40.07	20.13	2.67	0.06	-24.84	0.10
302	13:25:21.421	-42:59:39.60	16.24	1.68	0.06	-33.08	0.55
303	13:25:35.260	-43:01:29.04	25.49	4.47	0.06	-110.16	0.29
304	13:25:29.678	-43:01:26.02	36.57	7.66	0.05	41.65	0.43
305	13:25:26.035	-43:00:32.23	17.63	2.21	0.07	18.76	0.45
306	13:25:31.674	-43:01:03.79	23.37	3.97	0.07	-52.43	0.20
307	13:25:30.231	-43:01:26.87	24.74	4.57	0.07	-79.63	0.10
308	13:25:34.257	-43:01:18.12	23.77	3.46	0.06	-131.93	0.09
309	13:25:34.082	-43:02:01.05	17.90	2.22	0.07	-130.44	0.63
310	13:25:37.872	-43:01:54.32	23.17	3.36	0.06	83.08	0.47
311	13:25:35.452	-43:02:02.17	17.36	2.23	0.07	-124.58	0.37
312	13:25:35.241	-43:02:01.02	18.92	2.74	0.07	-53.94	0.20
313	13:25:21.295	-43:00:15.33	20.36	2.63	0.06	85.56	0.43
314	13:25:32.574	-43:01:26.81	18.16	2.19	0.06	4.49	0.39
315	13:25:28.376	-43:00:25.84	24.55	4.77	0.07	-39.61	0.23
316	13:25:22.027	-42:59:45.35	16.24	1.71	0.06	-232.16	0.64

Number	α (J2000)	δ (J2000)	r, pc	$M(10^4 M_\odot)$	$density$	PA	e
317	13:25:31.074	-43:01:29.44	25.49	4.97	0.07	-54.50	0.47
318	13:25:35.875	-43:02:09.36	16.81	1.77	0.06	-41.31	0.22
319	13:25:24.562	-43:00:36.01	17.36	2.18	0.07	-59.86	0.30
320	13:25:24.515	-43:01:09.42	30.23	6.49	0.07	-131.12	0.31
321	13:25:33.813	-43:01:34.84	16.53	1.86	0.06	-50.98	0.44
322	13:25:30.418	-43:01:38.96	28.79	5.81	0.07	0.42	0.53
323	13:25:22.583	-43:00:08.68	26.76	4.91	0.06	-16.02	0.52
324	13:25:24.845	-43:00:00.85	19.41	2.60	0.06	25.94	0.43
325	13:25:25.400	-43:00:11.21	24.55	4.20	0.07	-35.51	0.28
326	13:25:22.427	-43:00:19.92	20.36	2.76	0.06	-98.98	0.33
327	13:25:28.359	-43:01:10.78	19.41	2.59	0.06	14.97	0.55
328	13:25:21.480	-43:00:17.92	16.81	1.89	0.06	-89.39	0.12
329	13:25:34.816	-43:01:46.34	22.97	3.63	0.06	-128.92	0.10
330	13:25:32.155	-43:01:37.48	23.17	4.21	0.07	65.24	0.60
331	13:25:23.803	-43:01:01.95	24.36	4.27	0.07	-43.99	0.41
332	13:25:31.309	-43:01:21.08	16.81	2.04	0.07	-100.35	0.57
333	13:25:37.034	-43:02:11.06	16.81	1.82	0.06	-94.91	0.43
334	13:25:23.003	-42:59:59.45	20.59	3.02	0.07	-6.93	0.61
335	13:25:33.687	-43:02:01.35	21.70	3.26	0.07	25.97	0.61
336	13:25:37.737	-43:01:39.92	24.55	3.75	0.06	33.85	0.62
337	13:25:25.851	-43:00:30.50	27.62	4.68	0.06	-235.90	0.46
338	13:25:31.728	-43:01:08.68	20.82	2.60	0.06	-96.79	0.54
339	13:25:20.427	-43:00:19.38	16.53	1.75	0.06	-127.53	0.34
340	13:25:27.218	-43:00:22.12	17.09	2.28	0.07	43.75	0.34
341	13:25:37.165	-43:02:11.05	16.24	2.02	0.07	-96.39	0.19
342	13:25:34.579	-43:01:45.20	20.36	2.68	0.06	-40.23	0.20
343	13:25:28.772	-43:00:31.01	20.82	3.05	0.07	-237.79	0.50
344	13:25:23.198	-43:01:03.98	18.16	2.27	0.06	12.08	0.11
345	13:25:21.665	-43:00:21.95	22.34	3.60	0.07	-108.50	0.28
346	13:25:21.455	-43:00:29.73	17.63	2.09	0.06	14.45	0.25
347	13:25:34.999	-43:01:41.44	21.48	2.98	0.06	23.23	0.34
348	13:25:22.870	-42:59:51.68	20.82	3.05	0.07	-232.46	0.52
349	13:25:25.876	-43:00:25.32	30.07	6.51	0.07	-264.22	0.38
350	13:25:22.081	-42:59:55.72	21.26	3.43	0.07	71.53	0.45
351	13:25:21.218	-43:00:28.01	22.13	3.41	0.07	-11.00	0.22
352	13:25:22.244	-43:00:23.38	25.12	4.40	0.07	72.92	0.57
353	13:25:37.391	-43:01:21.78	16.81	1.74	0.06	11.77	0.34
354	13:25:22.855	-43:00:57.65	21.70	3.35	0.07	-62.33	0.10
355	13:25:22.263	-42:59:43.33	19.41	2.69	0.07	-33.31	0.17
356	13:25:22.106	-42:59:46.50	19.17	2.70	0.07	18.43	0.17
357	13:25:34.607	-43:01:53.84	21.92	3.58	0.07	17.21	0.18
358	13:25:23.535	-43:00:34.59	23.57	3.66	0.06	65.69	0.35

Number	α (J2000)	δ (J2000)	r, pc	$M(10^4 M_\odot)$	$density$	PA	e
359	13:25:24.695	-43:00:44.07	23.57	3.72	0.06	-56.88	0.34
360	13:25:30.465	-43:01:12.17	15.65	1.81	0.07	-126.96	0.24
361	13:25:31.365	-43:01:37.50	22.55	3.69	0.07	-32.70	0.40
362	13:25:29.224	-43:00:52.90	20.36	2.69	0.06	29.95	0.47
363	13:25:26.928	-43:00:21.84	19.65	2.94	0.07	-127.54	0.22
364	13:25:29.836	-43:01:23.42	35.13	8.16	0.06	18.31	0.68
365	13:25:28.729	-43:01:16.82	62.30	29.65	0.07	43.32	0.61
366	13:25:25.350	-43:00:29.36	21.92	3.15	0.06	-117.88	0.26
367	13:25:30.570	-43:01:09.57	17.09	2.04	0.07	-30.69	0.35
368	13:25:34.439	-43:01:09.48	30.84	6.04	0.06	84.32	0.66
369	13:25:37.610	-43:02:00.09	24.93	3.80	0.06	43.67	0.14
370	13:25:24.168	-43:00:38.32	15.95	1.62	0.06	-60.45	0.22
371	13:25:24.594	-43:01:08.56	16.81	2.07	0.07	-113.76	0.24
372	13:25:26.770	-43:00:22.71	21.26	3.33	0.07	-28.33	0.30
373	13:25:24.853	-43:00:42.05	22.34	3.50	0.07	22.14	0.57
374	13:25:22.689	-43:00:12.13	20.59	2.99	0.07	-248.90	0.45
375	13:25:25.879	-43:00:42.03	31.45	6.82	0.06	-89.81	0.39
376	13:25:31.286	-43:01:36.35	22.76	3.69	0.07	4.80	0.44
377	13:25:24.588	-43:00:34.56	20.13	2.83	0.07	3.47	0.61
378	13:25:25.935	-43:00:59.89	19.65	2.43	0.06	-23.99	0.49
379	13:25:27.591	-43:00:48.90	19.41	2.55	0.06	34.92	0.29
380	13:25:18.473	-42:59:33.61	17.90	1.93	0.06	73.74	0.58
381	13:25:32.278	-43:00:57.14	21.70	2.85	0.06	69.16	0.56
382	13:25:36.339	-43:01:27.86	19.17	2.31	0.06	39.19	0.17
383	13:25:20.692	-43:00:27.15	21.70	3.19	0.06	-55.19	0.09
384	13:25:30.705	-43:01:26.86	26.58	5.26	0.07	40.33	0.14
385	13:25:25.558	-43:00:14.09	15.95	1.82	0.07	-11.10	0.61
386	13:25:23.247	-43:00:40.07	16.24	1.55	0.06	34.13	0.44
387	13:25:21.823	-43:00:26.84	16.53	1.87	0.06	80.38	0.41
388	13:25:25.178	-43:01:33.03	18.16	2.24	0.06	-50.41	0.25
389	13:25:36.216	-43:02:05.89	15.65	1.47	0.06	19.04	0.56
390	13:25:23.926	-43:00:10.67	28.30	4.93	0.06	-254.18	0.63
391	13:25:30.274	-43:00:36.45	22.55	2.97	0.05	-122.50	0.49
392	13:25:23.326	-43:00:41.22	15.95	1.53	0.06	39.37	0.47
393	13:25:31.965	-43:01:10.98	28.95	5.55	0.06	38.04	0.62
394	13:25:22.053	-42:59:41.90	16.81	1.78	0.06	30.33	0.19
395	13:25:38.320	-43:01:55.18	16.53	1.72	0.06	1.94	0.32
396	13:25:24.541	-43:01:03.09	22.97	3.28	0.06	-63.21	0.30
397	13:25:23.063	-43:00:41.80	27.28	4.87	0.06	-100.20	0.33
398	13:25:35.268	-43:02:07.07	15.95	1.65	0.06	25.22	0.26
399	13:25:24.402	-43:00:24.20	25.49	3.68	0.05	75.92	0.49
400	13:25:36.299	-43:02:22.89	19.41	2.49	0.06	-96.90	0.39

Number	α (J2000)	δ (J2000)	r, pc	$M (10^4 M_\odot)$	*density*	PA	e
401	13:25:26.959	-43:00:44.31	16.24	1.67	0.06	10.07	0.15
402	13:25:21.790	-42:59:47.09	16.81	1.67	0.06	-44.34	0.47
403	13:25:24.775	-43:00:47.52	22.97	3.11	0.06	-119.26	0.43
404	13:25:25.584	-43:00:08.90	27.28	4.54	0.06	-45.02	0.29
405	13:25:37.946	-43:01:31.85	22.97	3.10	0.06	32.69	0.28
406	13:25:30.093	-43:00:56.33	16.24	1.48	0.05	-3.15	0.51
407	13:25:34.652	-43:01:20.13	20.82	2.43	0.05	59.51	0.57
408	13:25:28.910	-43:01:01.26	22.97	3.12	0.06	16.93	0.39
409	13:25:29.512	-43:00:47.13	20.82	2.58	0.06	18.45	0.24
410	13:25:26.907	-43:00:48.05	17.63	1.91	0.06	82.99	0.68
411	13:25:22.878	-43:00:39.50	23.77	3.53	0.06	-0.83	0.31
412	13:25:29.594	-43:00:59.80	21.04	2.58	0.05	-95.68	0.35
413	13:25:32.410	-43:00:57.72	18.16	2.00	0.06	-8.47	0.16
414	13:25:30.070	-43:01:11.03	15.65	1.46	0.06	-1.52	0.21
415	13:25:38.159	-43:01:41.64	15.95	1.46	0.05	69.03	0.33
416	13:25:24.531	-43:00:06.33	19.17	2.20	0.06	-134.83	0.34
417	13:25:31.257	-43:01:23.10	16.24	1.54	0.06	-39.53	0.14
418	13:25:37.902	-43:02:10.74	18.16	1.92	0.05	64.16	0.68
419	13:25:27.190	-43:00:14.34	16.24	1.54	0.06	-55.81	0.20
420	13:25:32.755	-43:01:08.94	24.74	3.51	0.05	37.14	0.57
421	13:25:27.324	-43:00:27.01	18.16	1.95	0.06	72.49	0.42
422	13:25:35.235	-43:01:35.96	18.16	1.84	0.05	-90.00	0.08
423	13:25:22.615	-43:00:42.38	15.65	1.32	0.05	37.84	0.68
424	13:25:23.088	-43:00:33.44	22.76	2.94	0.05	61.25	0.53
425	13:25:24.292	-42:59:57.70	17.63	1.84	0.06	-74.81	0.12
426	13:25:38.027	-43:01:41.07	25.68	3.84	0.05	-104.63	0.27
427	13:25:21.611	-43:00:17.05	16.24	1.56	0.06	0.00	0.16
428	13:25:29.121	-43:01:03.27	15.65	1.30	0.05	58.30	0.63
429	13:25:33.739	-43:01:56.74	16.24	1.40	0.05	-3.45	0.47
430	13:25:33.998	-43:01:37.43	21.48	2.75	0.06	-35.73	0.53
431	13:25:19.766	-42:59:56.92	17.36	1.73	0.05	14.39	0.37
432	13:25:37.182	-43:01:30.14	16.81	1.67	0.06	-235.00	0.47
433	13:25:35.793	-43:01:58.99	19.17	2.11	0.05	11.75	0.28
434	13:25:19.737	-42:59:39.35	16.24	1.56	0.06	-85.21	0.27
435	13:25:21.819	-42:59:57.75	24.17	3.38	0.05	73.04	0.49
436	13:25:23.725	-43:01:05.70	17.09	1.54	0.05	-38.19	0.57

References

Allamandola, L. J., Hudgins, D. M., & Sandford, S. A. 1999, ApJ, 511, L115

Allen, M. M. 1994, ApJ, 424, 754

Alves, J. F., Lada, C. J., & Lada, E. A. 2001, Nature, 409, 159

Arnaboldi, M., Freeman, K. C., Gerhard, O., et al. 1998, ApJ, 507, 759

Baade, W. & Minkowski, R. 1954, ApJ, 119, 215

Bagnulo, S., Jehin, E., Ledoux, C., et al. 2003, The Messenger, 114, 10

Beals, C. S. 1938, ApJ, 87, 568

Beals, C. S. & Blanchet, G. H. 1937, PASP, 49, 224

Bedregal, A. G., Aragón-Salamanca, A., Merrifield, M. R., & Milvang-Jensen, B. 2006, MNRAS, 371, 1912

Bender, R., Saglia, R. P., & Gerhard, O. E. 1994, MNRAS, 269, 785

Bijaoui, A., Slezak, E., & Vandame, B. 1998, in Astrophysics and Algorithms

Blitz, L. & Shu, F. H. 1980, ApJ, 238, 148

Blitz, L. & Williams, J. P. 1999, ArXiv Astrophysics e-prints

Bohlin, R. C., Savage, B. D., & Drake, J. F. 1978, ApJ, 224, 132

Bolton, J. G., Stanley, G. J., & Slee, O. B. 1949, Nature, 164, 101

Bosma, A., Smith, R. M., & Wellington, K. J. 1985, MNRAS, 212, 301

Brosch, N., Kniazev, A. Y., Buckley, D. A. H., et al. 2007, MNRAS, 382, 1809

Cardelli, J. A. & Wallerstein, G. 1986, ApJ, 302, 492

Chaffee, Jr., F. H. & Lutz, B. L. 1977, ApJ, 213, 394

Chappell, D. & Scalo, J. 2001, ApJ, 551, 712

Charmandaris, V., Combes, F., & van der Hulst, J. M. 2000, A&A, 356, L1

Cheng, K. P., Collins, N., Angione, R., et al. 1997, in Bulletin of the American Astronomical Society, Vol. 29, Bulletin of the American Astronomical Society, 1107–+

Chung, A. & Bureau, M. 2004, AJ, 127, 3192

Clarke, D. A., Burns, J. O., & Norman, M. L. 1992, ApJ, 395, 444

Cowie, L. L. 1980, ApJ, 236, 868

Crane, P., Lambert, D. L., & Sheffer, Y. 1995, ApJS, 99, 107

Danks, A. C., Federman, S. R., & Lambert, D. L. 1984, A&A, 130, 62

Davies, R. L., Kuntschner, H., Emsellem, E., et al. 2001, ApJ, 548, L33

de Souza, R. E., Gadotti, D. A., & dos Anjos, S. 2004, ApJS, 153, 411

Devillard, N. 1997a, The Messenger, 87, 19

Devillard, N. 1997b, The Messenger, 87, 19

Di Matteo, P., Combes, F., Melchior, A. ., & Semelin, B. 2007, ArXiv e-prints

D'Onofrio, M. 2001, MNRAS, 326, 1517

D'Onofrio, M., Zaggia, S. R., Longo, G., Caon, N., & Capaccioli, M. 1995, A&A, 296, 319

Douglas, A. E. 1977, Nature, 269, 130

Dufton, P. L. & Lennon, D. J. 1989, A&A, 211, 397

Ekers, R. D., Goss, W. M., Wellington, K. J., et al. 1983, A&A, 127, 361

Elmegreen, B. G. 1993, ApJ, 419, L29+

Elmegreen, B. G. 2002, ApJ, 564, 773

Elmegreen, B. G., Efremov, Y., Pudritz, R. E., & Zinnecker, H. 2000, Protostars and Planets IV, 179

Elmegreen, B. G. & Falgarone, E. 1996, ApJ, 471, 816

Engargiola, G., Plambeck, R. L., Rosolowsky, E., & Blitz, L. 2003, ApJS, 149, 343

Erwin, P. & Sparke, L. S. 2003, ApJS, 146, 299

Federman, S. R. 1982, ApJ, 257, 125

Federman, S. R., Strom, C. J., Lambert, D. L., et al. 1994, ApJ, 424, 772

Field, G. B. 1974, ApJ, 187, 453

Finkelman, I., Brosch, N., Kniazev, A. Y., et al. 2008, MNRAS, 390, 969

Foing, B. H. & Ehrenfreund, P. 1997, A&A, 317, L59

Fomalont, E. B., Ebneter, K. A., van Breugel, W. J. M., & Ekers, R. D. 1989, ApJ, 346, L17

Fulara, J. & Krelowski, J. 2000, New Astronomy Review, 44, 581

Galazutdinov, G. 2005, Journal of Korean Astronomical Society, 38, 215

Galazutdinov, G. A. 1992, Bull. Special Astrophys. Obs., 92

Galazutdinov, G. A., Musaev, F. A., Krełowski, J., & Walker, G. A. H. 2000, PASP, 112, 648

Geldzahler, B. J. & Fomalont, E. B. 1984, AJ, 89, 1650

Gies, D. R. 1987, ApJS, 64, 545

Goudfrooij, P., Alonso, M. V., Maraston, C., & Minniti, D. 2001, MNRAS, 328, 237

Graham, J. A. 1979, ApJ, 232, 60

Gredel, R. 1997, A&A, 320, 929

Gredel, R., van Dishoeck, E. F., & Black, J. H. 1993, A&A, 269, 477

Groh, J. H., Hillier, D. J., & Damineli, A. 2006, ApJ, 638, L33

Heger, M. L. 1922, Lick Observatory Bulletin, 10, 141

Herbig, G. H. 1968, Zeitschrift fur Astrophysik, 68, 243

Herbig, G. H. 1975, ApJ, 196, 129

Herbig, G. H. 1995, ARA&A, 33, 19

Herbig, G. H. & Soderblom, D. R. 1982, ApJ, 252, 610

Heyer, M. H., Carpenter, J. M., & Snell, R. L. 2001, ApJ, 551, 852

Heyer, M. H. & Schloerb, F. P. 1997, ApJ, 475, 173

Hinkle, K. W., Keady, J. J., & Bernath, P. F. 1988, Science, 241, 1319

Hobbs, L. M., York, D. G., Snow, T. P., et al. 2008, ApJ, 680, 1256

Horellou, C., Black, J. H., van Gorkom, J. H., et al. 2001, A&A, 376, 837

Israel, F. P. 1998, A&A Rev., 8, 237

Jenniskens, P. & Desert, F.-X. 1994, A&AS, 106, 39

Josafatsson, K. & Snow, T. P. 1987, ApJ, 319, 436

Kainulainen, J., Juvela, M., & Alves, J. 2007, A&A, 468, 581

Kainulainen, J., Juvela, M., & Alves, J. 2008, A&A, 482, 229

Kellermann, K. I., Zensus, J. A., & Cohen, M. H. 1997, ApJ, 475, L93+

Kerr, T. H., Hibbins, R. E., Fossey, S. J., Miles, J. R., & Sarre, P. J. 1998, ApJ, 495, 941

Kramer, C., Stutzki, J., Rohrig, R., & Corneliussen, U. 1998, A&A, 329, 249

Krełowski, J., Ehrenfreund, P., Foing, B. H., et al. 1999, A&A, 347, 235

Krelowski, J. & Walker, G. A. H. 1987, ApJ, 312, 860

Krelowski, J. & Westerlund, B. E. 1988, A&A, 190, 339

Krumholz, M. R. & McKee, C. F. 2005, ApJ, 630, 250

Kudritzki, R.-P. 1980, A&A, 85, 174

Kwan, J. 1979, ApJ, 229, 567

Lada, C. J., Lada, E. A., Clemens, D. P., & Bally, J. 1994, ApJ, 429, 694

Lamers, H. J. G. L. M., Nota, A., Panagia, N., Smith, L. J., & Langer, N. 2001, ApJ, 551, 764

Larsson, H. & Siegbahn, P. E. M. 1983, J. Chem. Phys., 79, 2270

Larsson, M. 1983, A&A, 128, 291

Lien, D. J. 1984, ApJ, 284, 578

Lilley, A. E. 1955, ApJ, 121, 559

Linevsky, M. J. 1967, J. Chem. Phys., 47, 3485

Liszt, H. S. 2007, A&A, 476, 291

Lombardi, M. & Alves, J. 2001, A&A, 377, 1023

Longhetti, M., Rampazzo, R., Bressan, A., & Chiosi, C. 1998, A&AS, 130, 267

Luehrs, S. 1997, PASP, 109, 504

Mackie, G. & Fabbiano, G. 1998, AJ, 115, 514

Madore, B. F., Freedman, W. L., Silbermann, N., et al. 1999, ApJ, 515, 29

Maier, J. P., Lakin, N. M., Walker, G. A. H., & Bohlender, D. A. 2001, ApJ, 553, 267

Malin, D. F., Quinn, P. J., & Graham, J. A. 1983, ApJ, 272, L5

Marconi, A., Schreier, E. J., Koekemoer, A., et al. 2000, ApJ, 528, 276

Markova, N., Puls, J., Repolust, T., & Markov, H. 2004, A&A, 413, 693

Mattila, K. 1986, A&A, 160, 157

McGregor, P. J., Finlayson, K., Hyland, A. R., et al. 1988, ApJ, 329, 874

McKeith, C. D., Castles, J., Greve, A., & Downes, D. 1993, A&A, 272, 98

McKellar, A. 1940a, PASP, 52, 187

McKellar, A. 1940b, PASP, 52, 312

Megier, A., Strobel, A., Bondar, A., et al. 2005, ApJ, 634, 451

Mehlert, D., Saglia, R. P., Bender, R., & Wegner, G. 2000, A&AS, 141, 449

Merrill, P. W. 1934, PASP, 46, 206

Merrill, P. W. 1936, PASP, 48, 179

Merrill, P. W. & Wilson, O. C. 1938, ApJ, 87, 9

Mizuno, N., Rubio, M., Mizuno, A., et al. 2001a, PASJ, 53, L45

Mizuno, N., Yamaguchi, R., Mizuno, A., et al. 2001b, PASJ, 53, 971

Morton, D. C. 1974, ApJ, 193, L35

Morton, D. C., Drake, J. F., Jenkins, E. B., et al. 1973, ApJ, 181, L103+

Motte, F., Andre, P., & Neri, R. 1998, A&A, 336, 150

Motylewski, T., Linnartz, H., Vaizert, O., et al. 2000, ApJ, 531, 312

Musaev, F. A., Galazutdinov, G. A., Sergeev, A. V., Karpov, N. V., & Pod'Yachev, Y. V. 1999, Kinematics and Physics of Celestial Bodies, 15, 216

Nicholson, R. A., Bland-Hawthorn, J., & Taylor, K. 1992, ApJ, 387, 503

Nota, A., Pasquali, A., Marston, A. P., et al. 2002, AJ, 124, 2920

Nota, A., Smith, L., Pasquali, A., Clampin, M., & Stroud, M. 1997, ApJ, 486, 338

Nowak, N., Saglia, R. P., Thomas, J., et al. 2008, MNRAS, 391, 1629

Pan, K., Federman, S. R., Cunha, K., Smith, V. V., & Welty, D. E. 2004, ApJS, 151, 313

Peng, C. Y., Ho, L. C., Impey, C. D., & Rix, H.-W. 2002, AJ, 124, 266

Quillen, A. C., Brookes, M. H., Keene, J., et al. 2006, ApJ, 645, 1092

Quillen, A. C., de Zeeuw, P. T., Phinney, E. S., & Phillips, T. G. 1992, ApJ, 391, 121

Quillen, A. C., Graham, J. R., & Frogel, J. A. 1993, ApJ, 412, 550

Rachford, B. L., Snow, T. P., Tumlinson, J., et al. 2002, ApJ, 577, 221

Regan, M. W. & Mulchaey, J. S. 1999, AJ, 117, 2676

Reshetnikov, V. P. 2000, Astronomy Letters, 26, 485

Rest, A., van den Bosch, F. C., Jaffe, W., et al. 2001, AJ, 121, 2431

Rieke, G. H. & Lebofsky, M. J. 1985, ApJ, 288, 618

Rodgers, A. W., Conroy, P., & Bloxham, G. 1988, PASP, 100, 626

Rosolowsky, E. 2005, PASP, 117, 1403

Rosolowsky, E. 2007, ApJ, 654, 240

Rosolowsky, E. & Blitz, L. 2005, ApJ, 623, 826

Rosolowsky, E., Engargiola, G., Plambeck, R., & Blitz, L. 2003, ApJ, 599, 258

Rosolowsky, E. W., Goodman, A. A., Wilner, D. J., & Williams, J. P. 1999, ApJ, 524, 887

Saglia, R. P., Maraston, C., Thomas, D., Bender, R., & Colless, M. 2002, ApJ, 579, L13

Salama, F., Galazutdinov, G. A., Krełowski, J., Allamandola, L. J., & Musaev, F. A. 1999, ApJ, 526, 265

Salpeter, E. E. 1955, ApJ, 121, 161

Sarre, P. J., Miles, J. R., Kerr, T. H., et al. 1995, MNRAS, 277, L41

Savage, B. D., Bohlin, R. C., Drake, J. F., & Budich, W. 1977, ApJ, 216, 291

Savage, B. D., Cardelli, J. A., & Sofia, U. J. 1992, ApJ, 401, 706

Savage, B. D. & Sembach, K. R. 1996, ARA&A, 34, 279

Scalo, J. 1990, in Astrophysics and Space Science Library, Vol. 162, Physical Processes in Fragmentation and Star Formation, ed. R. Capuzzo-Dolcetta, C. Chiosi, & A. di Fazio, 151–176

Schadee, A. 1975, A&A, 41, 203

Schiminovich, D., van Gorkom, J. H., van der Hulst, J. M., & Kasow, S. 1994, ApJ, 423, L101+

Schmidt-Kaler, T., Tueg, H., Buchholz, M., & Schlosser, W. 1980, A&AS, 39, 305

Schreier, E. J., Capetti, A., Macchetto, F., Sparks, W. B., & Ford, H. J. 1996, ApJ, 459, 535

Schweizer, F. 1980, ApJ, 237, 303

Schweizer, F. 1981, ApJ, 246, 722

Scorza, C. & Bender, R. 1995, A&A, 293, 20

Sellwood, J. A. & Balbus, S. A. 1999, ApJ, 511, 660

Sembach, K. R., Danks, A. C., & Savage, B. D. 1993, A&AS, 100, 107

Sersic, J. L. 1968, Atlas de galaxias australes (Cordoba, Argentina: Observatorio Astronomico, 1968)

Sheffer, Y., Rogers, M., Federman, S. R., et al. 2008, ApJ, 687, 1075

Smith, L. F., Shara, M. M., & Moffat, A. F. J. 1990, ApJ, 358, 229

Smith, W. H., Schempp, W. V., & Federman, S. R. 1984, ApJ, 277, 196

Sneden, C., Gehrz, R. D., Hackwell, J. A., York, D. G., & Snow, T. P. 1978, ApJ, 223, 168

Solomon, P. M., Rivolo, A. R., Barrett, J., & Yahil, A. 1987, ApJ, 319, 730

Souza, S. P. & Lutz, B. L. 1977, ApJ, 216, L49

Spitzer, Jr., L. & Jenkins, E. B. 1975, ARA&A, 13, 133

Starck, J.-L., Murtagh, F., & Bijaoui, A. 1998, Image processing and data analysis. The multiscale approach (Image processing and data analysis. The multiscale approach, Publisher: Cambridge, UK: Cambridge University Press, 1998, ISBN: 0521590841)

Stokes, G. M. & Hobbs, L. M. 1976, ApJ, 208, L95

Stutzki, J., Bensch, F., Heithausen, A., Ossenkopf, V., & Zielinsky, M. 1998, A&A, 336, 697

Tatum, J. B. 1967, ApJS, 14, 21

Testi, L. & Sargent, A. I. 1998, ApJ, 508, L91

Thorburn, J. A., Hobbs, L. M., McCall, B. J., et al. 2003, ApJ, 584, 339

Tingay, S. J., Jauncey, D. L., Reynolds, J. E., et al. 1998, AJ, 115, 960

Tubbs, A. D. 1980, ApJ, 241, 969

van Breda, I. G. & Whittet, D. C. B. 1981, MNRAS, 195, 79

van den Bosch, F. C. 1998, ApJ, 507, 601

van Dishoeck, E. F. & Black, J. H. 1989, ApJ, 340, 273

van Gorkom, J. H., van der Hulst, J. M., Haschick, A. D., & Tubbs, A. D. 1990, AJ, 99, 1781

Vazquez-Semadeni, E., Ballesteros-Paredes, J., & Rodriguez, L. F. 1997, ApJ, 474, 292

Voors, R. H. M., Waters, L. B. F. M., de Koter, A., et al. 2000, A&A, 356, 501

Voors, R. H. M., Waters, L. B. F. M., Trams, N. R., & Kaeufl, H. U. 1997, A&A, 321, L21

Vuong, M. H., Montmerle, T., Grosso, N., et al. 2003, A&A, 408, 581

Wada, K., Spaans, M., & Kim, S. 2000, ApJ, 540, 797

Wade, C. M. 1961, The Observatory, 81, 202

Welty, D. E., Hobbs, L. M., Lauroesch, J. T., et al. 1999, ApJS, 124, 465

Welty, D. E., Hobbs, L. M., & Morton, D. C. 2003, ApJS, 147, 61

Weselak, T., Galazutdinov, G. A., Musaev, F. A., Beletsky, Y., & Krełowski, J. 2008a, A&A

Weselak, T., Galazutdinov, G. A., Musaev, F. A., & Krełowski, J. 2004, A&A, 414, 949

Weselak, T., Galazutdinov, G. A., Musaev, F. A., & Krełowski, J. 2008b, A&A, 484, 381

Weselak, T., Galazutdinov, G. A., Musaev, F. A., & Krełowski, J. 2008c, A&A, 484, 381

Weselak, T., Schmidt, M., & Krełowski, J. 2000, A&AS, 142, 239

Westerlund, B. E. & Krelowski, J. 1988a, A&A, 203, 134

Westerlund, B. E. & Krelowski, J. 1988b, A&A, 189, 221

White, S. M. 2000, ApJ, 539, 851

Whittet, D. C. B. 1992, Journal of the British Astronomical Association, 102, 175

Williams, J. P., de Geus, E. J., & Blitz, L. 1994, ApJ, 428, 693

Williams, J. P. & McKee, C. F. 1997, ApJ, 476, 166

Wilson, C. D. & Scoville, N. 1990, ApJ, 363, 435

York, D. G. 1971, ApJ, 166, 65